LOCAL MEASUREMENTS OF CYCLOTRON STATES IN GRAPHENE

A Thesis
Presented to
The Academic Faculty

by

Kevin Dean Kubista

In Partial Fulfillment
of the Requirements for the Degree
Doctor of Philosophy in the
School of Physics

Georgia Institute of Technology
May 2011

LOCAL MEASUREMENTS OF CYCLOTRON STATES IN GRAPHENE

Approved by:

Dr. Phillip First, Advisor
School of Physics
Georgia Institute of Technology

Dr. Markus Kindermann
School of Physics
Georgia Institute of Technology

Dr. Joseph Stroscio
Center for Nanoscale Science and Technology
National Institute of Standards and Technology

Dr. Andrew Zangwill
Physics
Georgia Institute of Technology

Dr. Zhigang Jiang
School of Physics
Georgia Institute of Technology

Date Approved: April 01, 2011

To my parents, Gayle and Rich Kubista.

ACKNOWLEDGEMENTS

I have relied on many people on my route towards earning my PhD and I would like to attempt to thank at least some of the people that have helped me. I will begin by thanking my advisor, Dr. Phillip First for giving me this opportunity and providing me with much needed guidance. In addition I want to thank Dr. Joseph Stroscio for giving me the opportunity to collect the data contained in this thesis, and for his assistance while at NIST, Gaithersberg. I would also like to thank the other committee members Dr. Zhigang Jiang, Dr. Markus Kindermann and Dr. Andrew Zangwill for their assistance towards my PhD. This entire work could not have been accomplished if it were not for the forethought of Dr. Walt de Heer, Dr. Claire Berger and the rest of Georgia Tech's Keck Lab: Mike Sprinkle, Xiaosong Wu, Ming Ruan, Yike Hu and Holly Tinkey. It is because of these people that I even had the opportunity to study epitaxial graphene. I would also like to thank Dr. Edward Conrad for his assistance in the lab. Finally, I want to thank my fellow lab mates: Lee Miller, Britt Torrance, Greg Rutter, Joanna Hass, Nikhil Sharma, Evan Green, Madeleine Phillips and Sameh Dardona.

I also want to thank those who have supported me throughout these years: Austin "Kaz" Bentley, Heather Bentley, Kirsten Eidsmoe, Chris Tidwell, and the members of the Atlanta Area Aquarium Association. My family: Gayle Kubista, Rich Kubista, Laura Kubista, Kristi Kubista-Hovis and Scott Kubista-Hovis have always been supportive and without them I would not have even imagined attempting this work. I would like to

conclude by thanking Lynn and Gary List, who without their assistance it is very doubtful that I would have completed my PhD.

TABLE OF CONTENTS

LIST OF TABLES

LIST OF FIGURES

LIST OF SYMBOLS AND ABBREVIATIONS

Å	Angstrom
a	Graphene lattice constant, 2.46 Å
AES	Auger electron spectroscopy
CMOS	Complementary Metal-Oxide-Semiconductors
CVD	Chemical Vapor Deposition
DoF	Degrees of Freedom
E_f	Fermi Energy
E_N	Energy Position of Landau Level N
FEM	Field Emission Microscope
FET	Field Effect Transistor
FIM	Field Ion Microscopy
FWHM	Full Width Half Max
HOPG	Highly Oriented Pyrolytic Graphite
IDL	Interactive Data Language
LEED	Low Energy Electron Diffraction
LDoS	Local Density of States
LL	Landau Level
LL_N	Landau Level with index N
piezos	Piezoelectric Transducers
QD	Quantum Dot
SdHOs	Shubnikov de Haas Oscillations
STM	Scanning Tunneling Microscopy

STS	Scanning Tunneling Spectroscopy
TIBB	Tip Induced Band Bending
TMCO	Tunneling Magneto Conductance Oscillation
TSP	Titanium Sublimation Pump
UCF	Universal Conductance Fluctuations
UHV	Ultra High Vacuum
QHE	Quantum Hall Effect
ℓ_B	Magnetic Length

SUMMARY

Graphene's unique massless electron behavior is observed in multilayer epitaxial graphene grown from SiC on the $(000\bar{1})$ face. These fermions collapse into cyclotron orbits (Landau levels) when graphene is placed into a high magnetic field, B. The Landau levels are shown to follow a $\sqrt{NB}$ energy dependence, where N is the quantum number of the Landau level. Cryogenic ultra-high vacuum scanning tunneling microscopy (STM) and spectroscopy (STS) are performed to study the local behavior of these cyclotron states near defects. A new STS technique was designed where conductance measurements were performed while the magnetic field was changed. This technique allows for a direct measurement of the energy versus momentum relationship for graphene.

These measurements produced results which indicate a local doping effect due to the STM tip. Techniques relying on degenerate perturbation theory for graphene states solved in the symmetric gauge are shown to reliably model these effects. This perturbation method allows for the study of local nanometer scale screening effects in graphene, and indicates that the local tip effect can be modeled as a defect potential. Measurements of Landau levels (LLs) will be shown to depend on the combined potential of the tip induced band bending (TIBB) potential and local defect potentials. In addition magnetically localized defect states are presented. These are not explained by TIBB. The defect states are argued to be Stark shifted in energy by TIBB, eventually crossing the Fermi energy, E_f. Once states cross E_f further doping effects from the tip are measured. This switch from hole to electron state is also shown to change the local

potential of the system which indicates a direct charge state of the defect, which modifies the local density of states.

CHAPTER 1

GRAPHENE

1.1 What's So Great About Graphene?

Graphene has quickly garnered the scientific community's attention producing over 5,500 papers from 2005 to 2010 containing the word "graphene" in their title.[1] Entire conferences[2, 3] dedicated only to graphene were created within four years of the demonstration of graphene's massless Dirac fermion behavior.[4, 5] Over the last five years results such as Klein tunneling,[6] and technologies like the 100 GHz field-effect transistor (FET),[7] and 97.7% transparent, flexible, conductive layers[8] (figure 1.1) emphasize why graphene remains a phenomenon in physics.

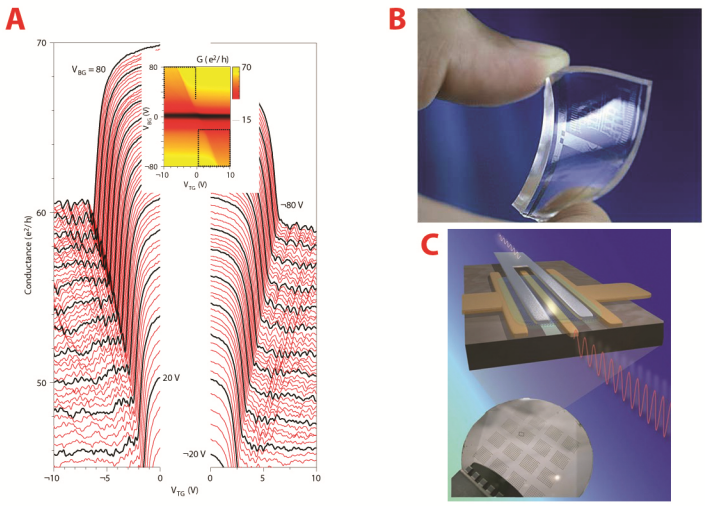

Figure 1.1: Graphene has been shown to have promising characteristics such as (A) Klein tunneling (figure from ref. 6), and graphene has been implemented in (B) nearly transparent large scale bendable conductive membranes (figure from ref. 8) and (C) 100 Ghz FET (figure from 7).

Some current investigations seek to exploit graphene's room temperature half-integer quantum Hall effect (QHE) to replace the resistivity standard.[9] For this and other applications, high carrier mobility is essential. Room temperate transport mobilities as

high as 120,000 cm^2/Vs have been reported,[10] and far infrared transmission experiments imply values as high as 250,000 cm^2/Vs.[11] Graphene is a leading material for next-generation touch screen displays,[12] and is now used for electrodes in the development of fast-charging batteries.[13] Finally, institutions such as Georgia Tech,[14] IBM,[7] and research collaborations like NRI[15] strive to control graphene's band structure in the hope of creating transistors suitable to replace and/or complement the work-horse complementary metal-oxide-semiconductor (CMOS) transistor used in modern Si-based computer chips. While graphene is still years away from attaining some of these goals, new breakthroughs occur constantly.[14]

1.2 Physical Characteristics of Graphene

Graphene is often described as carbon in a honeycomb or chicken-wire structure. Graphene was coined to describe a single layer of graphite[16] that consists of sp^2 ($2s$, $2p_x$, $2p_y$) bonded carbon atoms, with a unit cell containing two carbon atoms spaced 1.42 Å apart. The resulting structure can be seen in figure 1.2. In free-standing graphene, the remaining ½-filled $2p_z$ orbitals gives rise to graphene's unique electronic properties

Graphene's primitive unit cell is defined by two vectors that can be taken as:

$$\mathbf{a}_1 = \frac{a}{2}\left(\sqrt{3}\hat{\boldsymbol{x}} + \hat{\boldsymbol{y}}\right), \qquad \mathbf{a}_2 = \frac{a}{2}\left(\sqrt{3}\hat{\boldsymbol{x}} - \hat{\boldsymbol{y}}\right), \tag{1}$$

where a is the lattice constant, 2.46Å.

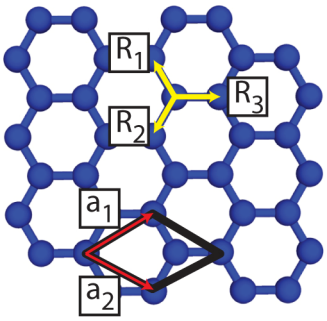

Figure 1.2: Graphene's lattice structure. Graphene's unit cell is defined by primitive unit vectors $\mathbf{a}_1$ and $\mathbf{a}_2$ (red arrows), which create the unit cell (black diamond). Each cell contains two atoms 1.42 Å apart. The second atom's location is described by the translation vectors $\mathbf{R}_1$, $\mathbf{R}_2$ and $\mathbf{R}_3$.

When viewed in reciprocal space, the basis vectors are:

$$\mathbf{b}_1 = \frac{2\pi}{a}\left(\frac{1}{\sqrt{3}}\hat{\boldsymbol{x}} + \hat{\boldsymbol{y}}\right)$$
$$\mathbf{b}_2 = \frac{2\pi}{a}\left(\frac{1}{\sqrt{3}}\hat{\boldsymbol{x}} - \hat{\boldsymbol{y}}\right). \qquad 2$$

In addition the second atom in the unit cell can be described using the translation vectors:

$$\mathbf{R}_1 = -\frac{a}{2}\left(\frac{\sqrt{3}}{3}\hat{\boldsymbol{x}} - \hat{\boldsymbol{y}}\right)$$
$$\mathbf{R}_2 = -\frac{a}{2}\left(\frac{\sqrt{3}}{3}\hat{\boldsymbol{x}} + \hat{\boldsymbol{y}}\right) \qquad 3$$
$$\mathbf{R}_3 = \frac{a}{2}\left(\frac{\sqrt{3}}{3}\hat{\boldsymbol{x}}\right).$$

By using these atomic lattice vectors in a tight binding model[17] one can obtain the following energy momentum relationship:

$$E\left(k_x, k_y\right) = \frac{\beta \pm \gamma\, \mathrm{w}\left(k_x, k_y\right)}{1 \pm s\, \mathrm{w}\left(k_x, k_y\right)} \qquad 4$$

where

$$w\left(k_x,k_y\right)=\sqrt{1+4\cos\frac{\sqrt{3}k_x a}{2}\cos\frac{k_y a}{2}+4\cos^2\frac{k_y a}{2}} \qquad 5$$

with "+" corresponding the valence band, and "–" the conduction band. This formula allows one to modify the π-bonding (transfer) integral (γ), on-site energy (β) and overlap integral (s) and is a result of nearest-neighbor carbon-carbon interactions obtained by diagonalizing the 2 x 2 Hamiltonian.[18] This energy momentum relation is shown in figure 1.3, with symmetry points K -Γ- M - K' identified in the first Brillouin zone.[19]

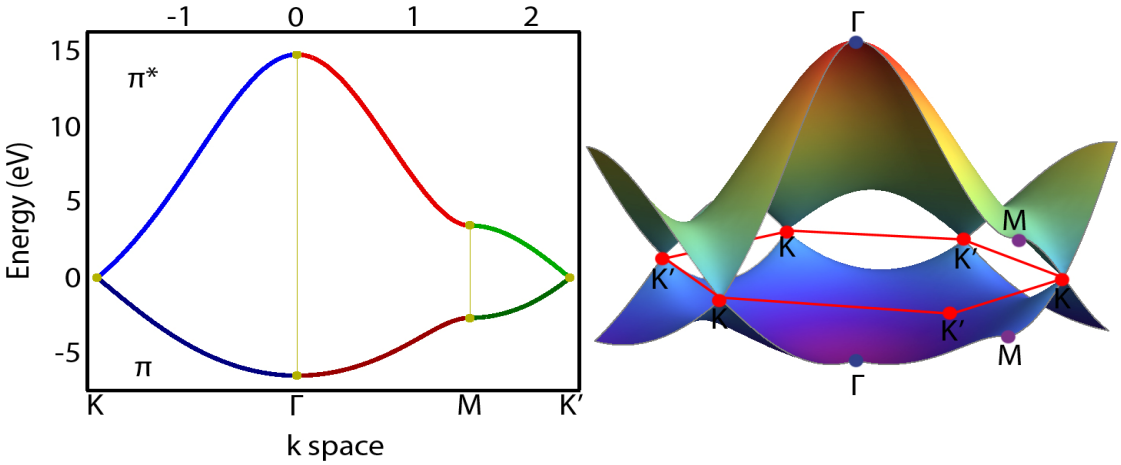

Figure 1.3: Tight binding results where π-bonding (transfer) integral $\gamma_0=-3$ eV , on-site energy $\beta=0$ eV and overlap integral $s=0.13$ eV .[19] The π and π* bands are seen to meet energy at the K and K' points. The resulting conical shape is referred to as the Dirac cone.

1.3 State Functions of Graphene

1.3.1 Zero Field

Near graphene's K and K' points the Hamiltonian can be simplified to a Dirac Hamiltonian that is often used to model defects and the effect of magnetic fields on graphene.[20-22] Without a defect potential the Hamiltonian can be written as:

$$\boldsymbol{H} = \frac{\gamma}{\hbar}\begin{pmatrix} 0 & \hat{\pi}_x - i\hat{\pi}_y \\ \hat{\pi}_x + i\hat{\pi}_y & 0 \end{pmatrix}, \tag{6}$$

where $\hbar$ is the Planck constant divided by 2π, $\gamma = \sqrt{3}a\gamma_0/2$ is a band parameter, and $\hat{\boldsymbol{\pi}} = \hat{\mathbf{p}} + \frac{e\mathbf{A}}{c}$, with $\hat{\mathbf{p}}$ being the momentum operator and $\mathbf{A}$ the magnetic vector potential.[23] With no magnetic field, $\mathbf{A} = 0$, and the Schrödinger equation, $\boldsymbol{H}\Psi = \mathrm{E}\Psi$, can be solved exactly. Solutions in the K and K' valleys are of the form of spinors, where the upper and lower components are the wave functions on the A and B carbon sublattices, respectively:[21]

$$\begin{aligned} \Psi^{K}_{\zeta\boldsymbol{k}}(\boldsymbol{r}) &= \frac{1}{\sqrt{2}L}\exp(i\boldsymbol{k}\cdot\boldsymbol{r})\begin{pmatrix} \zeta \\ \mathrm{e}^{i\varphi(\boldsymbol{k})} \end{pmatrix}, \\ \Psi^{K'}_{\zeta\boldsymbol{k}}(\boldsymbol{r}) &= \frac{1}{\sqrt{2}L}\exp(i\boldsymbol{k}\cdot\boldsymbol{r})\begin{pmatrix} \mathrm{e}^{i\varphi(\boldsymbol{k})} \\ \zeta \end{pmatrix}, \end{aligned} \tag{7}$$

where L^2 is area of the system $\varphi(\boldsymbol{k})$ is the angle of the wave vector $\boldsymbol{k}$, and ζ denotes the bands (+1 for conduction, –1 for valence). The resulting energy is

$$\mathrm{E}_{\zeta\boldsymbol{k}} = \zeta\gamma k, \tag{8}$$

with $k = |\boldsymbol{k}|$. This is the same linear result one would obtain from a Taylor expansion of equation 4 about the K and K' points and is often referred to as the Dirac cone. One can now equate the linear momentum dependence to that of massless neutrinos resulting in $\mathrm{E} = pc^*$, where $c^* = \sqrt{3}\gamma_0 a/2\hbar \sim 10^6$ m/s is the charge carrier velocity.

1.3.2 Landau Gauge

New discrete energy states arise when a magnetic field, $\mathbf{B} = B\hat{\mathbf{z}}$, is applied to graphene. By far the most common approach to solving the Schrödinger equation is to use the Landau gauge.[24] In this gauge there is only one component of the vector potential:

$$\mathbf{A} = \left(Bx\hat{\boldsymbol{y}} \right) \tag{9}$$

An exact solution can be obtained, resulting in state functions of the form:[21]

$$\begin{aligned} \Psi_{Nk}^{K}\left(\boldsymbol{r}\right) &= \frac{C_N}{\sqrt{L}}\exp(-iky)\begin{pmatrix} \operatorname{sgn}(N) i^{|N|-1}\phi_{|N|-1} \\ i^{|N|}\phi_{|N|} \end{pmatrix}, \\ \Psi_{Nk}^{K'}\left(\boldsymbol{r}\right) &= \frac{C_N}{\sqrt{L}}\exp(-iky)\begin{pmatrix} i^{|N|}\phi_{|N|} \\ \operatorname{sgn}(N) i^{|N|-1}\phi_{|N|-1} \end{pmatrix}, \end{aligned} \tag{10}$$

where

$$C_N = \begin{cases} 1 & (N=0) \\ \dfrac{1}{\sqrt{2}} & (N\neq 0) \end{cases}, \quad \operatorname{sgn}(N) = \begin{cases} 1 & (N>1) \\ 0 & (N=0), \\ -1 & (N<0) \end{cases} \tag{11}$$

and

$$\phi_{|N|} = \frac{1}{\sqrt{2^{|N|}\,|N|!\sqrt{\pi}\,\ell_B}}\exp\left[-\frac{1}{2}\left(\frac{x-\ell_B^2 k}{\ell_B}\right)^2\right] H_{|N|}\left(\frac{x-\ell_B^2 k}{\ell_B}\right). \tag{12}$$

The magnetic length is $\ell_B = \sqrt{\hbar/eB}$ and $H_N\left(x\right)$ are Hermite Polynomials. This solution uses three quantum numbers (N, j, k) where $N = 0, \pm 1, \pm 2, \ldots$ is the Landau level (LL) index, $j = K$ and K', and k is the electron wave vector in the Y direction.[21] The resulting eigenvalues are:

$$E_N = \operatorname{sgn}(N) c^* \sqrt{2e\hbar B|N|}. \tag{13}$$

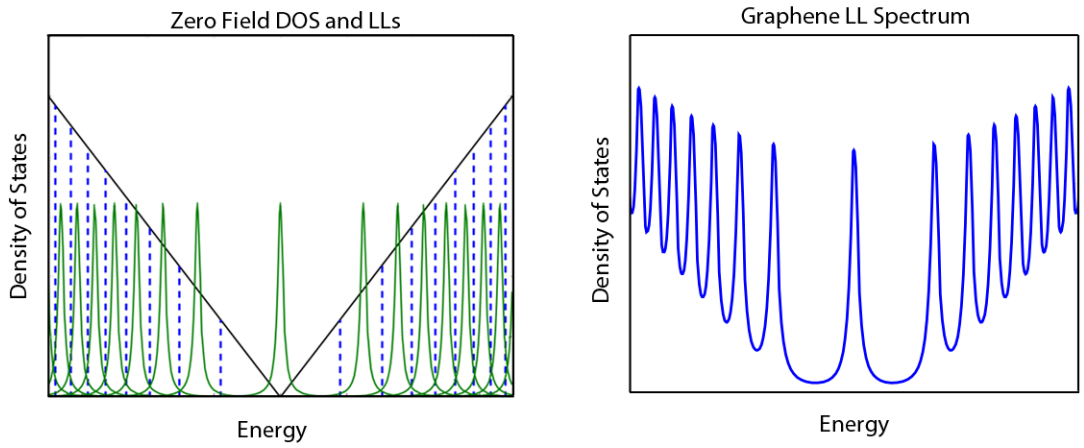

Figure 1.4: (A) The ideal linear density of states implied by equation 8 is shown in black. When a magnetic field is applied states collapse into discrete LLs (green) which follow the energy dependence in equation 13. Due to finite hot-carrier lifetime these states will have a finite width and at higher energy they overlap. (B) This overlap causes local density of state (LDoS) measurements to appear to contain a background slope.

In 2005, Novoselov *et al.*[4] and Zhang *et al*[5] found that the density of states collapses into a series of LLs when a magnetic field is applied[24] (figure 1.4). These LLs were observed as steps in resistance measurements using the Hall bar geometry, and were shown to follow the massless fermion behavior of equation 13. This special series of quantized resistance values is known as the half-integer quantum Hall effect. It should be noted that while mathematically each state should collapse into a δ-function, due to electron-impurity interactions, inter-LL electron-electron scattering, and other lifetime-limiting mechanisms, the peaks will be Lorentzian in real samples. Convolutions with a Gaussian instrument function would result in Voigt-function peaks.[25] A feature of both the integer and half-integer quantum Hall effects is that the energy only relies on the quantum number N and not on k. A result of this is that the wave functions form parallel strips in the Y direction spaced equally along the X direction.[24] This result is entirely due to the choice of $\mathbf{A}$ and one could have chosen a gauge where strips were parallel in the X direction. Though somewhat concerning, this result is acceptable since

all states within a LL are degenerate allowing any mixture of them with the same energy to form a solution to the Schrödinger equation. Another result from equation 13 is that graphene, unlike two-dimensional massive fermion systems, has a Landau level zero (LL_0) which is composed of both valence- and conduction-band states. This result led to the eventual observation of the fractional quantum Hall effect where the electrons and magnetic flux quanta bind to form complex composite quasiparticles.[26]

1.3.3 Symmetric Gauge

Another common gauge used to solve the Schrödinger equation is the symmetric gauge where the magnetic potential is defined as:

$$\mathbf{A} \to A_\theta = \frac{1}{2} Br, A_r = A_z = 0. \tag{14}$$

In this gauge **A** forms circles about the origin, making solutions ideal for cylindrical polar coordinates. The symmetric gauge is generally used to describe Fock-Darwin states created by quantum dots (QD)[23] where rotational symmetry is important, but if dealing with an infinite system become more difficult. When the Schrödinger equation is solved using this gauge one obtains:[23, 24, 27]

$$\begin{aligned} \Psi^{K}_{n,m} &= C_N \begin{pmatrix} \mathrm{sgn}(N)\phi_{n,m-1}(x) \\ i\phi_{n,m}(x) \end{pmatrix} \\ \Psi^{K'}_{n,m} &= C_N \begin{pmatrix} i\phi_{n,m}(x) \\ \mathrm{sgn}(N)\phi_{n,m-1}(x) \end{pmatrix} \end{aligned} \tag{15}$$

where again

$$C_N = \begin{cases} 1 & (N = 0) \\ \dfrac{1}{\sqrt{2}} & (N \neq 0) \end{cases}, \quad \mathrm{sgn}(N) = \begin{cases} 1 & (N > 1) \\ 0 & (N = 0) \\ -1 & (N < 0) \end{cases}, \tag{16}$$

while without normalization

$$\phi_{n,m}(r) \propto r^{|m|} e^{im\theta} L_n^{|m|}(r^2/2\ell_B^2) e^{(-r^2/4\ell_B^2)}, \tag{17}$$

with $L_n^{|m|}(x)$ the Laguerre polynomials. This result can be verified by using the Laguerre properties[28]

$$\frac{d^k L_n^a(x)}{dx^k} = (-1)^k L_{n-k}^{a+k}(x) \tag{18}$$

and

$$L_n^a(x) = L_n^{a+1}(x) - L_{n-1}^{a+1}(x) \tag{19}$$

when plugging the state functions (equation 15) back into the Schrödinger wave equation. For nomenclature purposes the author will later refer to these states as $|n,m\rangle$ states, where $\langle n,m|n,m\rangle = \left|\Psi_{n,m}^{K}\right|^2 = \left|\Psi_{n,m}^{K'}\right|^2$. The eigenvalues are the same as in equation 13, but now

$$|N| = n + \frac{|m|+m}{2}. \tag{20}$$

While the total LL index N contains the same values, the possible values n and m must be given careful consideration. For example LL_2 will contain states with $n = 0,1,2$ and states with $m = 0,\pm1,\pm2,-3,-4,-5\ldots$ Interestingly the energy is independent of the second quantum number for $m \le 0$. These n and m quantum numbers are inherently difficult to envision, but semi-classically the m index is used to describe the electron's angular momentum. m's positive and negative states occur due to the alignment or anti-alignment of the magnetic field with the magnetic moment.[24] For a positive m the magnetic field increases the effective transverse momentum, while a negative m will decrease the effective transverse momentum.[23] This can physically be interpreted as the rotation induced by the magnetic field plus the rotation due to m. The second quantum number, n, give the number of radial nodes.

1.3.3.1 Symmetric Gauge Ladder Operators

To better understand these quantum numbers a pseudo-momentum operator can be constructed.

$$\widehat{\boldsymbol{\pi}}' = \hat{\mathbf{p}} - \frac{e\mathbf{A}}{c} \tag{21}$$

The momentum operator and vector potential are now of the form:

$$\begin{aligned} \hat{\mathbf{p}} &= \frac{1}{2}\left(\hat{\boldsymbol{\pi}} + \widehat{\boldsymbol{\pi}}'\right), \\ \mathbf{A} &= \frac{c}{2e}\left(\hat{\boldsymbol{\pi}} - \widehat{\boldsymbol{\pi}}'\right). \end{aligned} \tag{22}$$

The pseudo-momentum depends on the gauge and does not represent a physical quantity, but the commutator is gauge-invariant,[29]

$$\left[\widehat{\pi}'_{\mathrm{x}}, \widehat{\pi}'_{\mathrm{y}}\right] = i\frac{\hbar^2}{\ell_B^2} \tag{23}$$

Additionally mixed commutators are found to have extra quantities:

$$\begin{aligned} \left[\widehat{\pi}_{\mathrm{x}}, \widehat{\pi}'_{\mathrm{x}}\right] &= \frac{2ie\hbar}{c}\frac{\partial A_x}{\partial x}, \\ \left[\widehat{\pi}_{\mathrm{y}}, \widehat{\pi}'_{\mathrm{y}}\right] &= \frac{2ie\hbar}{c}\frac{\partial A_y}{\partial y}, \\ \left[\widehat{\pi}_{\mathrm{x}}, \widehat{\pi}'_{\mathrm{y}}\right] &= \frac{ie\hbar}{c}\left(\frac{\partial A_x}{\partial y} + \frac{\partial A_y}{\partial x}\right) = -\left[\widehat{\pi}'_{\mathrm{x}}, \widehat{\pi}_{\mathrm{y}}\right] \end{aligned} \tag{24}$$

These would create unphysical quantities due to the components of the pseudo-momentum that do not commute with the Hamiltonian. But, in the symmetric gauge these extra mixed commutators are null. This is not true for the Landau gauge where $\left[\widehat{\pi}_{\mathrm{x}}, \widehat{\pi}'_{\mathrm{y}}\right]$ would not vanish, but by remaining in the symmetric gauge ladder operators can now be constructed:

$$b=\frac{\ell_B}{\sqrt{2}\hbar}\left(\widehat{\pi'_x}+i\widehat{\pi'_y}\right),\qquad b^\dagger=\frac{\ell_B}{\sqrt{2}\hbar}\left(\widehat{\pi'_x}-i\widehat{\pi'_y}\right),$$
$$a=\frac{\ell_B}{\sqrt{2}\hbar}\left(\widehat{\pi_x}-i\widehat{\pi_y}\right),\qquad a^\dagger=\frac{\ell_B}{\sqrt{2}\hbar}\left(\widehat{\pi_x}+i\widehat{\pi_y}\right). \tag{25}$$

These operators have different quantum numbers:

$$b^\dagger\left|N,m'\right\rangle=\sqrt{m'+1}\left|N,m'+1\right\rangle,\qquad b\left|N,m'\right\rangle=\sqrt{m'}\left|N,m'-1\right\rangle,$$
$$a^\dagger\left|N,m'\right\rangle=\sqrt{N+1}\left|N+1,m'\right\rangle,\qquad a\left|N,m'\right\rangle=\sqrt{N}\left|N-1,m'\right\rangle. \tag{26}$$

In LL_0, $N=0=n+\frac{|m|+m}{2}$ which means that these states will have identical physical characteristics to the states identified in equation 15 since $|m|=m'$ and $n=0$. These ladder operators can be expressed in position representation by defining a new coordinate system $z=x-iy$, $z^*=x+iy$, $\partial=\left(\partial_x+i\partial_y\right)/2$, and $\bar{\partial}=\left(\partial_x-i\partial_y\right)/2$. Resulting in:[29]

$$b=-i\sqrt{2}\left(\frac{z^*}{4\ell_B}+\ell_B\partial\right),\qquad b^\dagger=i\sqrt{2}\left(\frac{z}{4\ell_B}-\ell_B\bar{\partial}\right),$$
$$a=-i\sqrt{2}\left(\frac{z}{4\ell_B}+\ell_B\bar{\partial}\right),\qquad a^\dagger=i\sqrt{2}\left(\frac{z}{4\ell_B}-\ell_B\partial\right). \tag{27}$$

The states are then constructed by:

$$\left|N,m'\right\rangle=\frac{\left(a^\dagger\right)^N}{\sqrt{N!}}\frac{\left(b^\dagger\right)^{m'}}{\sqrt{m'!}}\left|N=0,m'=0\right\rangle. \tag{28}$$

Careful consideration must be given for arbitrary LL states due to the differential operators.

1.3.3.2 Semiclassical Interpretation

These operators can now be a compared to the classical equations of motions for a massive electron in a magnetic field.[29]

$$m\ddot{\mathbf{r}} = -e\left(\dot{\mathbf{r}} \times \mathbf{B}\right) \Leftrightarrow \begin{matrix} \ddot{x} = -\omega_C \dot{y} \\ \ddot{y} = \omega_C \dot{x} \end{matrix}, \tag{29}$$

which when integrated gives:

$$\begin{matrix} \dot{x} = \dfrac{\widehat{\pi_x}}{m} = -\omega_c \left(y - Y\right) \\ \dot{y} = \dfrac{\widehat{\pi_y}}{m} = \omega_c \left(x - X\right) \end{matrix} \Leftrightarrow \begin{matrix} y = Y - \dfrac{\widehat{\pi_x}}{eB} \\ x = X + \dfrac{\widehat{\pi_y}}{eB} \end{matrix}. \tag{30}$$

From this an integration constant, $\boldsymbol{R} = \left(X, Y\right)$, can be interpreted as the "guiding center" of the electronic cyclotron motion.[29] This constant of the motion can now be related to the pseudo-potential by using in the symmetric gauge with equation 22 resulting in:

$$\begin{aligned} y &= \frac{c}{eB}\left(\widehat{\pi'_x} - \widehat{\pi_x}\right), \\ x &= \frac{c}{eB}\left(\widehat{\pi_y} - \widehat{\pi'_y}\right). \end{aligned} \tag{31}$$

When comparing equation 31 with equation 30 one arrives at:

$$\begin{aligned} X &= -\frac{c\widehat{\pi'_y}}{eB}, \\ Y &= -\frac{c\widehat{\pi'_x}}{eB} \end{aligned} \tag{32}$$

This result shows that the pseudo-momentum can be considered as components of the guiding center in the symmetric gauge.

A second parameter identified as the "cyclotron variable", $\hat{\boldsymbol{\eta}} = (\widehat{\eta_x}, \widehat{\eta_y})$, will now be introduced. This variable describes the dynamics of the electron in a magnetic field and can be considered as the time-dependent component of the position.[30] The cyclotron variable is perpendicular to the electron's velocity and can be described using the gauge-invariant momentum:

$$\widehat{\eta_x} = \frac{c\widehat{\pi_x}}{eB}$$
$$\widehat{\eta_y} = -\frac{c\widehat{\pi_y}}{eB}. \qquad 33$$

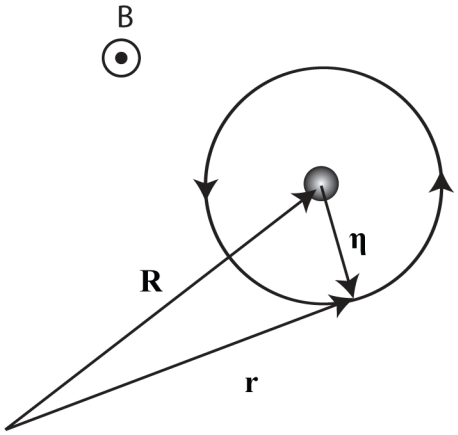

Figure 1.5: The classical picture of an electron in a magnetic field undergoing cyclotron motion around a guiding center $\boldsymbol{R}$. The grey region indicates the quantum mechanical uncertainty of the center's location due to the non-commutativity of its components.[29]

The position operator of the electron is defined by the sum of the guiding center and the cyclotron variable,

$$\mathbf{r} = \mathbf{R} + \boldsymbol{\eta}. \qquad 34$$

A physical interpretation is shown in figure 1.5. The state functions in the symmetric gauge (figures 1.6 to 1.9) show the average guiding center value is always zero:[29]

$$\langle \boldsymbol{R} \rangle \equiv \langle N, m' | \boldsymbol{R} | N, m' \rangle = 0, \qquad 35$$

but the magnitude of the guiding center is:

$$\langle |\boldsymbol{R}| \rangle \equiv \left\langle \sqrt{X^2 + Y^2} \right\rangle = \ell_B \langle N, m' | \sqrt{2b^\dagger b + 1} | N, m' \rangle = \ell_B \sqrt{2m' + 1}. \qquad 36$$

This indicates that average electron position for any $|N, m'\rangle$ state is situated on a circle of radius $\ell_B \sqrt{2m'+1}$, while the phase is undetermined. When considering only LL_0 this relationship can be applied to equation 15's quantum numbers, indicating that the

electron guiding center radius is $\ell_B\sqrt{2|m|+1}$. This length dependency is best seen in LL_0's probability density, figure 1.6.

A second length, called the cyclotron radius, is defined by:

$$\left\langle|\boldsymbol{\eta}|\right\rangle \equiv \left\langle\sqrt{\eta_x^2+\eta_y^2}\right\rangle = \ell_B\left\langle N,m'\left|\sqrt{2a^\dagger a+1}\right|N,m'\right\rangle = \ell_B\sqrt{2|N|+1}. \qquad 37$$

By using equation 20 the cyclotron radius in the symmetric gauge is then,

$$R_c = \ell_B\sqrt{2\left(n+\frac{|m|+m}{2}\right)+1}. \qquad 38$$

This radial dependence shows that the larger the value of n and m, the further a fermion will be orbiting from the guiding center. Figures 1.7 and 1.8 demonstrate the cyclotron radial dependence when the LL index is increased, while figure 1.9 demonstrates the dependence on the magnetic length.

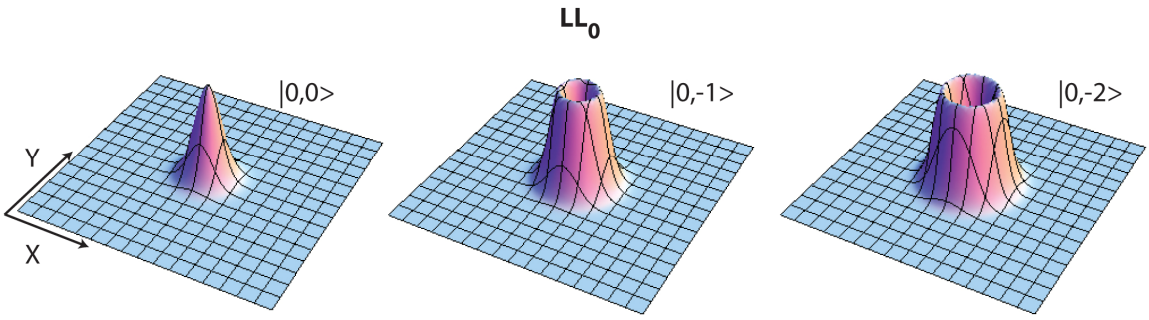

Figure 1.6: Probability density, $|\Psi|^2$, of the $|n,m>$ states which reside closest to $r=0$ in LL_0. As $|m|$ grows larger the magnitude of the guiding center of each state moves farther from zero, while the average guiding center remains zero.

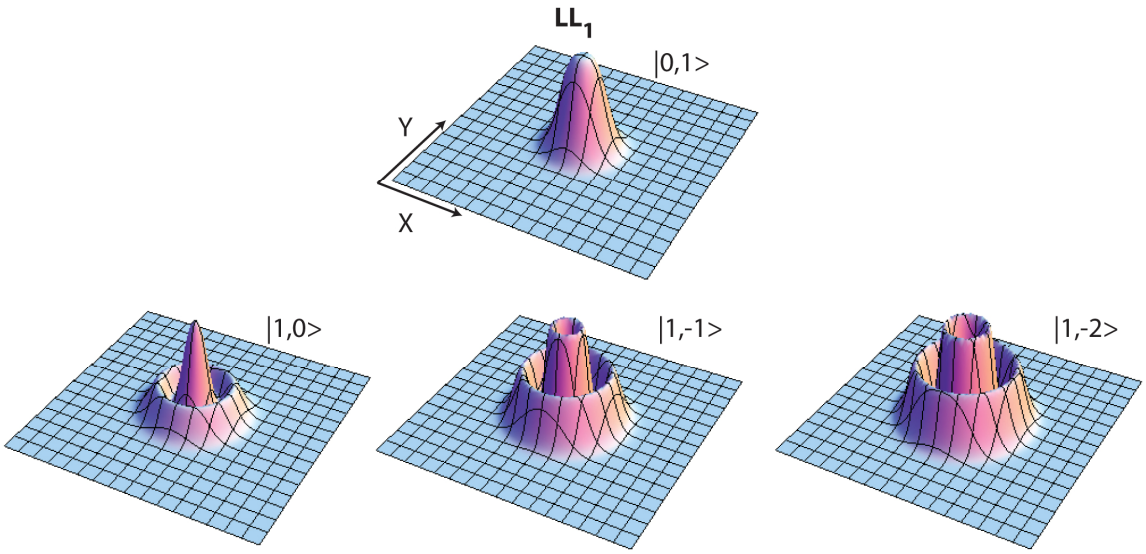

Figure 1.7: Probability density, $|\Psi|^2$, of the $|n,m>$ states which reside closest to $r=0$ in LL_1. Since $N \neq 0$ additional positive m states are possible. $|\Psi(0)|^2 \neq 0$ for state $|0,1>$ and $|1,0>$ in LL_1 due to the mixed nature of Ψ.

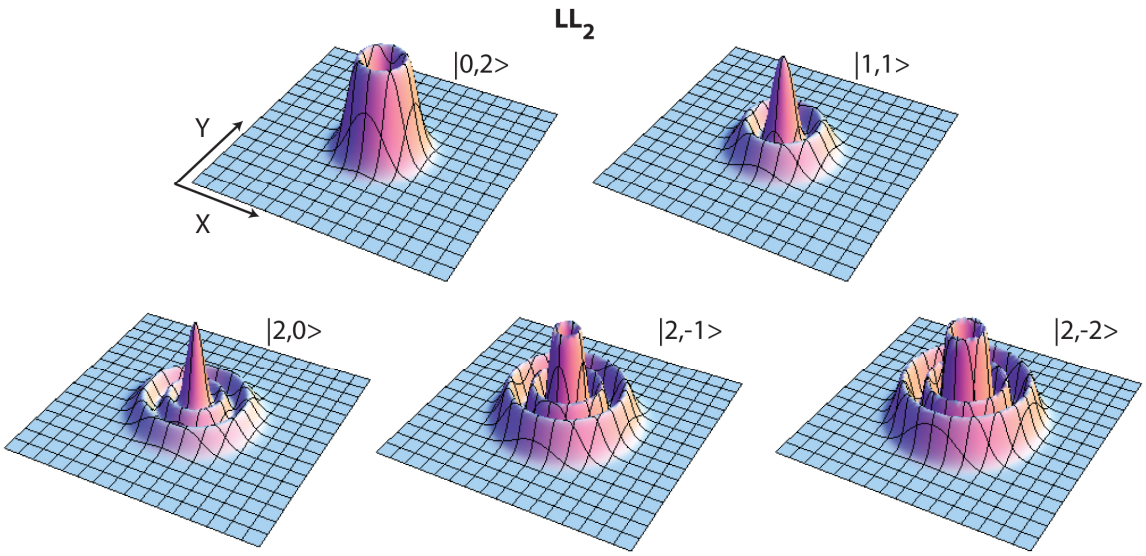

Figure 1.8: Probability density, $|\Psi|^2$, of the $|n,m>$ states which reside closest to $r=0$ in LL_2. The co-dependence of the quantum states (n, m) on the cyclotron radius can be seen as the average electron position moves further from the origin when $|m|$ increases, and additional rings become present as n increases in index.

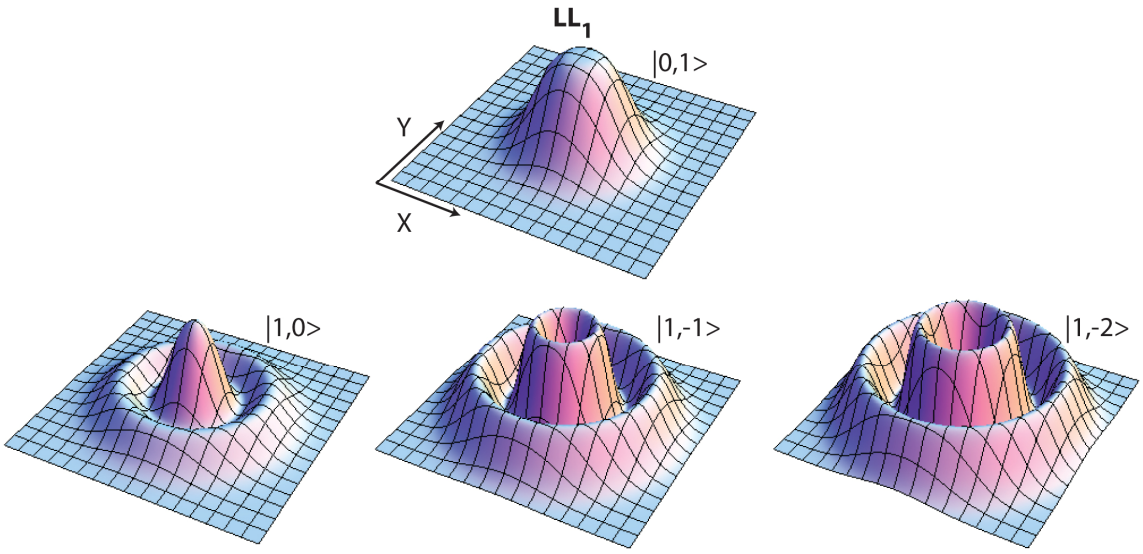

Figure 1.9: Probability density, $|\Psi|^2$, of the $|n,m>$ states which reside closest to $r=0$ in LL_1. Here the magnetic length has been doubled (magnetic field reduced by a factor of 4) from figure 1.7. One can quickly see how $|\Psi|^2$ is located closer to the origin as the magnetic field increases.

1.3.4 Degeneracy

Each LL has a maximum number of degenerate states defined by the magnetic flux.[30]

$$N_B = A \times \frac{B}{h/e} = A \times n_B , \tag{39}$$

with A the area. This maximum degeneracy can be thought of as the total number of cyclotron orbits that can fit in a disk of graphene of radius $R_{\max}$. If the electronic density, n_{el}, is known, the filling factor or maximum number of states in each LL can be extracted:[30]

$$\nu = \frac{n_{el}}{n_B} = \frac{h n_{el}}{eB}. \tag{40}$$

The total number of states in LL_0 can then be determined by equating equation 36 with the maximum radius of the graphene disk, $R_{\max} = \ell_B \sqrt{2M+1}$. This indicates that the

maximum number of states in a disc of area A is set by $A = \pi \ell_B^2 (2M + 1)$. If $M \gg 1$ one then arrives at $M = \frac{A}{2\pi \ell_B^2} = n_B \times A = N_B$.[29]

1.4 Defects in Graphene

Defects are an essential aspect of understanding experimental results obtained from graphene. Trapped dopants between SiO_2 and exfoliated graphene have been shown to create local electron and hole puddles.[31] Once graphene was suspended the effect of these puddles on transport characteristics became clear.[32] Even with suspension, new defects in the form of ripples[33] and flexural phonons became a concern.[34]

Intrinsic defects such as vacancies and adatoms have been investigated,[35-38] yet many theoretically predicted phenomenon, such as atomic collapse[39] and Hofstadter butterfly effects,[40] have not been observed. It is the hope of many to fully understand the effect of defects and then to use them to devise methods towards creating the future graphene based transistor.[41-43]

1.5 Methods of Creating Graphene

Over the last 10 years there have been remarkable advances in the process of creating graphene. Three techniques will be briefly outlined with an emphasis on epitaxial growth from SiC, since it is the technique by which samples were created for this thesis.

1.5.1 Exfoliation

Mechanical exfoliation of graphite was shown in 2004 to be a simple approach to obtaining microscopic flakes of graphene for two-dimensional transport studies.[44] This technique originally entailed repeatedly peeling flakes of graphite off of prepared mesas of highly oriented pyrolytic graphite (HOPG) attached to photoresist using adhesive tape. The remaining thin flakes on the photoresist were then removed using acetone and placed onto a Si wafer with a 300 nm of SiO_2. This thickness happened to be ideal, allowing a

single layer of graphene to be identified optically, due to optical interference in SiO_2.[44] Once a graphene flake was found, techniques developed for carbon nanotubes were then utilized to the create Hall bars and other transport devices.

Due to its relative simplicity, this method was quickly adopted by those in the transport community. Using this technique sample sizes of 10 μm x 10 μm are reliably produced, and occasionally samples as large as $(100\ \mu m)^2$ can be found.[44] While first touted as ideal graphene, interface interaction with the SiO_2 was recognized as a mobility-limiting factor[45, 46] due to acoustic phonon coupling and trapped charges.[26] Suspended graphene removed these limitations by removing SiO_2 from under the graphene.[10, 47] These samples show dramatically higher mobilities but are difficult to prepare and study. Nevertheless two-terminal measurements were found to exhibit the fractional QHE.[26, 32]

A simpler approach was found to circumvent the mobility-reducing phonon modes in SiO_2. Graphene was placed on alternate substrates, such as boron nitride[48] and the fractional QHE was shown using a hall Bar probe.[49] In addition, it has been shown that graphene's mobility and carrier density can be modified by materials like ligand-bound nanoparticles, which act as charge reservoirs, removing or supplying charge to create a more uniformly charged layer of graphene.[50]

While exfoliation has been an extremely useful tool for understanding graphene, it unfortunately has the same downside as carbon nanotubes. Samples are small in size and placement is nearly random. Due to these facts research has broadened into other techniques which show promise for large scale production of graphene.

1.5.2 Chemical Vapor Deposition

While successful in making carbon fiber, filament, and nanotube materials for more than 30 years,[51] chemical vapor deposition (CVD) has only recently been implemented in the graphene community. A recent publication demonstrated the ability to create

predominantly monolayer 30-inch graphene films on copper substrates by introducing a carbonaceous gas at temperatures < 1000 C.[12] The substrate can then be removed via etching. This process led to the first commercially viable graphene-based touch-screen. Unfortunately the process of removing graphene from copper damages the samples, resulting in poor mobilities, but recent work has been performed using nano-copper crystals to seed deposits of single layer graphene directly on dielectric substrates.[52] The benefit of this method is that the copper films de-wet and evaporate during or immediately after graphene growth, leaving undamaged graphene tens of micrometers wide. This technique could be used to control locations of grain boundaries which are believed to have a large impact on mobility.[53] Further studies have been performed on multiple metals including poly-nickel,[54] iridium,[55] ruthenium,[56] and palladium.[57] Copper remains the most promising substrate in growing single layer graphene, likely due to its low solubility of carbon.

1.5.3 Epitaxial Growth on SiC

The final technique involves the thermal decomposition of SiC to produce graphene. This technique has been known since 1975[58] to produce "monolayer graphite", but it wasn't until 2004[59] that researchers at Georgia Tech used this method to create a route towards scalable production of graphene devices.[60] By using this technique wafer scale samples can be created on SiC, with mobilities as high as suspended graphene. The quantum Hall effect and an ideal Dirac-cone dispersion (figure 1.10 A) have also been observed.[11, 61-63]

Samples used in these studies were grown from 4H (figure 1.10 B) and 6H (figure 1.10 C) SiC wafers in temperatures > 1300º C using a low-vacuum induction furnace in Dr. Walt de Heer's lab. This technique controls the silicon sublimation rate by creating a silicon-rich environment in the furnace. Previous studies have shown that graphization in ultra high vacuum (UHV) results in poor quality materials which exhibit small domains

and include pitting and graphene-free regions.[64] It is believed that higher temperatures allow carbon to migrate across the surface, but in order to prevent lower temperature graphitization the Si sublimation rate must be reduced by either confinement or by introducing gases.[64] Extensive research is continuing to further control the growth process and to reduce the density of "pleats", which are folds of the graphene film that relieve compressive stress from the SiC substrate.[65] Currently, pleat free domains as large as 10 μm can be grown (figure 1.10 D) with graphene growing continuously over both pleats and SiC steps. Pleats can be manipulated by atomic force manipulation, but they may or may not return to their original state after deformation.[66]

Another challenge for epitaxial graphene on SiC is that graphene film cannot be easily back-gated to control the carrier density. While top-gates and side-gates have been shown to work for graphene,[67] this does affect the ease with which experimental research can be performed.

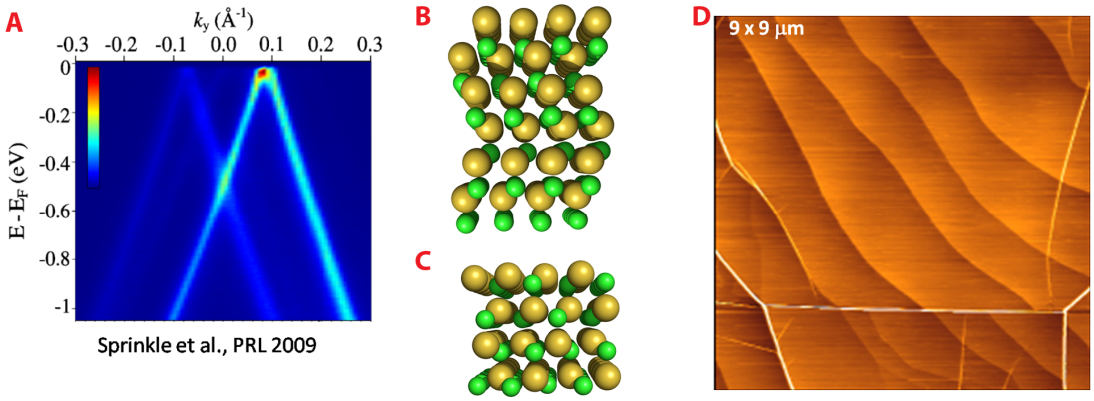

Figure 1.10: (A) Multi layer epitaxial graphene has been shown to contain primarily Dirac fermions,[62] where each layer has its own Dirac cone (figure from ref. 62). Multi layer epitaxial graphene has been grown from (B) 6H and (C) 4H SiC. The carbon (green) terminated face graphitizes at lower temperatures and is used to create this unique structure. Graphene growth on the silicon face (yellow) is self limiting and exhibits mostly Bernal stacking shown in figure 1.11. Wafer scale samples can be grown. (D) While pleats (figure from ref. 64) occur regularly due to thermal expansion mismatch between graphene and SiC the graphene layer remains continuous across the surface, growing over steps.[64]

Extensive research exists[35, 61, 64] detailing the differences between samples grown on the Si-face (0001) and the C-face ($000\bar{1}$), and a short summary will be given here to emphasize the difference.

1.5.3.1 SiC (0001)

Carbon grown on the silicon face has had considerably more research performed on it. This is likely due to the self limiting effect[61] where under UHV conditions the first carbon rich layer, referred to as the buffer layer or layer 0, forms at temperatures above 1100 C.[64] Upon investigation with low energy electron diffraction (LEED) a commensurate $\left(6\sqrt{3}\times 6\sqrt{3}\right)$R30º reconstruction is observed. This layer is believed to be graphene with its π orbitals tightly bound to the SiC causing this layer to be non-conductive.[68] Extensive STM and STS measurements have been performed revealing a gap around E_f and subsurface orbitals clearly seen through the interface indicate a tight coupling between the buffer layer and the SiC.[68] This layer has recently been decoupled by hydrogen passivation, resulting in the recovery of graphene's Dirac like spectrum.[69]

The next graphene layer (layer 1) grows relatively controlled[63] exhibiting all of graphene's signatures including the quantum Hall effect.[60, 70] While not bound to the SiC, this layer is still highly doped, placing E_f near -400 meV.[71] The carbon film grows in a mostly Bernal stacking order (figure 1.11 A) identical to graphite and exhibits bi-layer properties when the buffer layer is decoupled.[71] Mobilities tend to be around 1000-2000 cm^2/Vs.[61] Various means of decoupling may improve these values in the future.

1.5.3.2 SiC($000\bar{1}$)

The carbon face grows quite differently. UHV studies all but ignored this face for thin carbon growth due to the amorphous carbon and carbon nanotubes that would quickly form.[65] But graphitizing under low-vacuum conditions presents completely different growth characteristics. While sample thickness is extremely hard to control, a well

calibrated furnace has been used to grow monolayer graphene.[72] Carbon growth is nearly unlimited with 100-layer samples easily achieved.[58] Like the Si-face, graphene layers closest to the SiC are highly doped. The lowest layer, or interface layer, has E_f ~400 meV and dominates electronic transport.[63] Interestingly, samples obtained via low pressure induction furnaces do not stack like graphite (Bernal stacking), but instead, layers tend to have slight rotations between them. These stacking rotations create moiré patterns (figure 1.11 B) that affect the apparent height in STM measurements. Due to literature existing on the effects of moiré patterns on graphene, this thesis will be limited to only reporting on the angle of rotations observed. These angles were derived using the moiré unit cell distance and the relation:[73]

$$D = \frac{a}{2\sin(\theta/2)}, \qquad 41$$

where D is the lattice parameter of the hexagonal moiré superlattice, $a = 2.46$ Å is the graphene lattice constant, and θ is the rotation angle between the two graphene lattices. Rotations cause the creation of regions where atoms appear AA stacked and regions where they appear AB stacked. Studies performed on these multi-layer epitaxial graphene suggest that this periodic rearrangement of stacking is enough to electronically decouple each layer. In particular evidence of increased layer separation[64] direct observation of the Dirac energy dispersion,[62] Landau levels which follow equation 13,[74, 75] and mobilities up to 250,000 cm^2/Vs[11] have all been shown. Subtle effects of the symmetry-breaking AB/BA stacking regions also have been discovered.[76, 77] It should be mentioned that other methods of growing carbon-face samples do not necessarily reproduce these rotated-layer samples. Instead results using CVD systems with SiC show rotated domains only near pleats[78] and have much lower mobilities.[79]

The physics of "twisted" graphene layers is in its infancy, with both experimental and theoretical challenges.[80-82] Predictions such as velocity renormalization and small

band gaps have yet to be understood, and are not observed (so far) on samples created in a low-vacuum induction furnace.[62, 74]

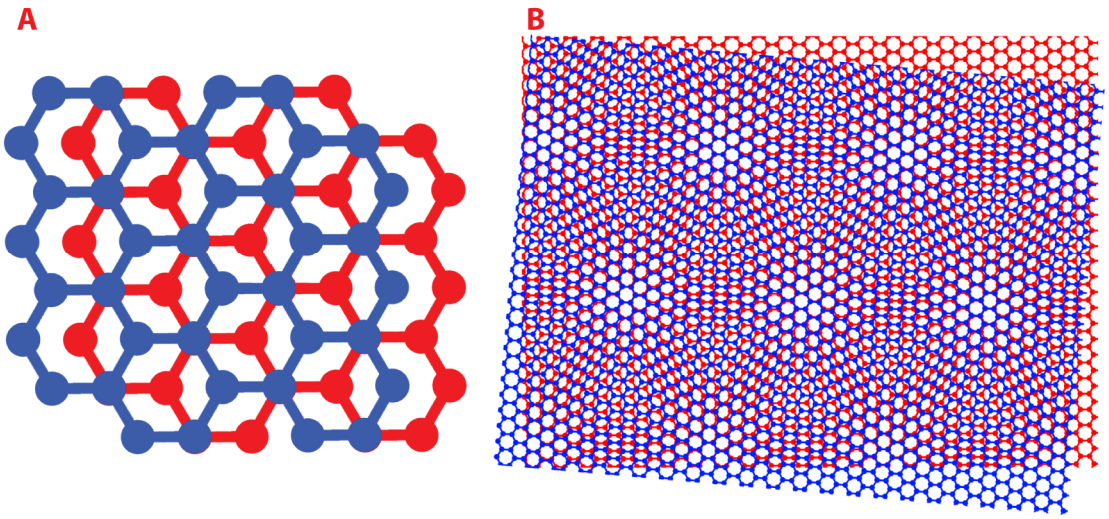

Figure 1.11: (A) Si-face graphene grows by Bernal stacking, where each layer is rotated 60º from the next. (B) Multi layer epitaxial graphene grown on C-face of SiC undergoes quasi-random rotations. This creates domains in each layer where atoms will be either commensurate or incommensurate with atoms in the layer below. This pattern is referred to as a moiré pattern, and is believed to be the reason why multiple layers of graphene behave like independent monolayers.[80]

CHAPTER 2

EXPERIMENTAL INSTRUMENTATIONS AND TECHNIQUES

2.1 Scanning Tunneling Microscopy and Spectroscopy

Multiple techniques have been used to characterize epitaxial graphene, but only scanning tunneling microscopy (STM) and spectroscopy (STS) are precise enough to investigate the effects of defects on the atomic scale. While beneficial for preparing samples, other measurement techniques such as low energy electron diffraction (LEED) and Auger electron spectroscopy (AES) will not be presented.

2.1.1 History

Since the 1980's STM has provided direct atomic scale measurements of material properties. The process of developing the first technique to truly verify nanoscience predictions arguably began by the demonstration of electron tunneling in the 1960s by Giaever.[83] In the 1970's R. Young, J. Ward and F. Scire modified this technique to achieve vacuum tunneling. They then went on to include the use of piezoelectric transducers (piezos) creating a three dimensional scanning device called the "topografiner" which used field emission current to sense the local topography.[84] The development of the scanning tunneling microscope did not occur until the 1980's, when Binnig and Rohrer demonstrated the atomic scale imaging of monosteps on a $CaIrSn_4$ single crystal.[85, 86] STM development has continued over the years to the point where high magnetic field studies at ultra low temperatures can now be performed.[87]

2.1.2 Theory

2.1.2.1 Microscopy

In principle STM is a relatively straightforward procedure which is shown in figure 2.1. To obtain an atomic image, a small bias is applied between an atomically sharp tip and a

conducting sample. The tip is lowered to within a few angstroms of the surface where the electron wave functions of the tip and sample overlap, inciting tunneling events. As electrons tunnel from tip to sample or vice versa the corresponding current can be measured. This current is changed by moving the tip closer to or farther from the sample. A feedback (servo) loop is used to maintain a constant current as the tip is rastered in the *X* direction. The amount by which the tip's height was changed by the servo is recorded (figure 2.1 B), and the process is repeated at successive *Y* positions to obtain in an atomic scale topograph (figure 2.1 C). As discussed below, the atomic-scale lateral resolution is a consequence of the strong dependence of the tunnel current on the tip-sample separation, which localizes the current source to the few most prominent atoms on the tip.

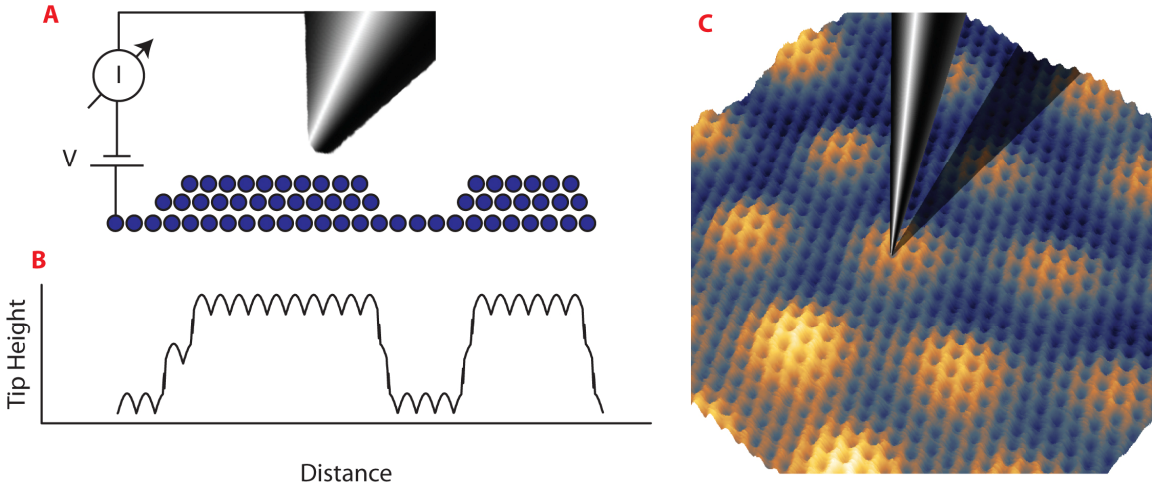

Figure 2.1: STM. (A) A voltage is applied between a conducting surface and a tip. The tip is then lowered a few angstroms from the surface, creating a measured tunnel current which depends exponentially on tip-sample separation. The tip can then be placed in a servo loop to maintain constant current by varying the height of the tip. (B) The height variation of the tip while moving in the *X* direction can be recorded as a constant current profile. (C) Topographs result from scanning in the *X* and *Y* directions, imparting atomic scale information. These images must be carefully interpreted due to the dependence on LDoS variations. In this case large moiré regions (orange) appear as height variations which are instead due to an increased probability of tunneling into an AA stacked region.

The mathematical basis of this process will now be given, modeling both tip and sample as planar electrodes with normals along the x axis ($x = 0$ is taken to lie at the end of the tip). STM relies on the fact that electrons tunnel through a vacuum barrier of

length d (the distance from tip to sample). The electron state function, $\psi_n(x)$, can be found by solving the Schrödinger wave equation[88] and the resulting probability for any tunneling event will be:

$$\mathrm{P} \propto \left|\psi_n(0)\right|^2 \mathrm{e}^{-2\kappa d}, \tag{42}$$

where $\kappa = \sqrt{2m\left(V_B - E\right)}/\hbar$ while V_B denotes the barrier potential, m is the mass of the electron, and E is the energy of the state. V_B may not be constant across the gap, but for this work it will be assumed to be the vacuum level. Hence, for states at the Fermi level ($\mathrm{E_f}$), $V_B - E$ is the work function.[89] Using these results one obtains for a small range, eV, of electron energies:

$$I \propto \sum_{E_\mathrm{f}-eV}^{E_\mathrm{f}} \left|\psi_n(0)\right|^2 \mathrm{e}^{-2\kappa d} \propto \rho\left(E_\mathrm{f}\right) eV \left|\psi_n(0)\right|^2 \mathrm{e}^{-2\kappa d} \tag{43}$$

where $\rho(E_\mathrm{f})$ is the local density of states at the Fermi energy. This indicates that the current has an exponential dependence on the distance of the tip sample gap. The decay constant 2κ is typically $\sim 0.2\ \mathrm{nm}^{-1}$ since most work functions are 4.5-5.5 eV.[89] This means that the tunneling current will drop by almost an order of magnitude for every 0.1 nm change in the tip-sample separation. It is this fact that allows for STM to achieve atomic scale imaging, but it was only made possible by the development of piezo-electric scan control[84] and effective vibration isolation.[85, 86]

2.1.2.2 *I* vs. *Z*

I vs. Z spectra are obtained by varying the Z height (tip-sample separation) for the purpose of measuring the decay constant between the tip and sample. Each spectrum is obtained after setting the initial Z by servoing at a set sample bias and reference current. Subsequently, the servo is held and the current is measured as the tip is retracted from the surface. Data can be fit to equation 43 allowing for the direct measurement of the sample decay constant for different sample biases. This measurement gives an indication of the

state of the tunneling junction and typically indicates a dependence on the tip apex for low tip-sample distances. By using these measurements current and voltage set points can be chosen where decay constants appear nearly constant, indicating little dependence on the tip shape.[90]

2.1.2.3 Spectroscopy

Scanning Tunneling Spectroscopy (STS) was developed within a few years of STM, in order to measure the energy-resolved local density of states (LDoS). At any position the tip can be taken out of the servo loop and held at a constant height. A slowly changing DC bias (figure 2.2) can then be applied while the corresponding change in current is measured. More advanced systems utilize a lock in amplifier, which allows one to add an additional AC modulation to the DC bias. The dI/dV can then be directly measured, which under certain assumptions is found to be directly proportional to the LDoS. A single spectrum can take from several ms up to 5 minutes to acquire, making vibration control vital for precision measurements.

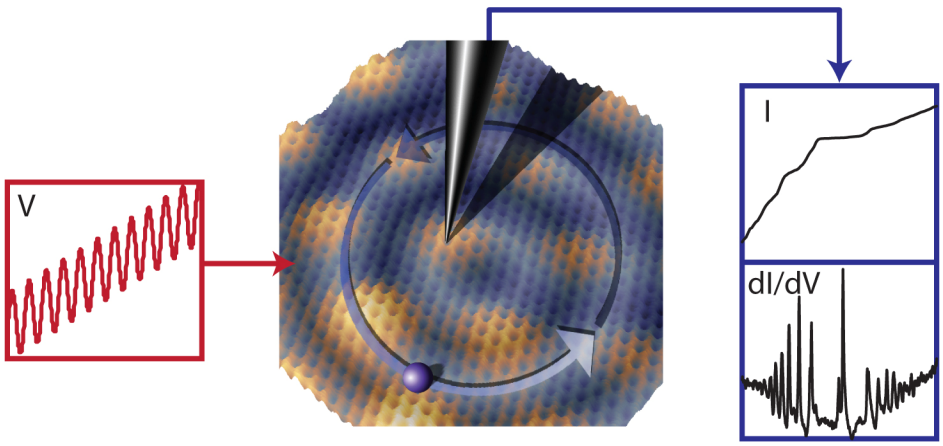

Figure 2.2: Scanning tunneling spectroscopy. While holding the tip at constant height the sample bias (red) can be slowly varied with an added (exaggerated) AC signal applied. The corresponding I and dI/dV can be measured giving the LDoS to sub-angstrom accuracy.

To understand how this measurement relates to LDoS, one must return to the current. By assuming a constant density of states for the tip and zero temperature, the current can be approximated to the form,

$$I(V) \propto \int_{E_F}^{E_F+eV} \rho(E) T(E,V)\, dE \qquad 44$$

where $\rho(E)$ is the local density of states at the surface and $T(E,V)$ is a barrier transmission coefficient.[89] $T(E,V)$ has only a small V dependence when V is much less then the work function. Often in this regime it is assumed to be constant, allowing one to measure the density of states by measuring the $dI/dV \propto \rho(E)$. This approximation is not applicable at higher bias where the effects of $dT(E,V)/dV$ must be considered.[91]

Spectroscopy measurements can be performed in multiple locations to characterize atomic scale features such as defects. The tip is held at a constant height at predefined positions and STS measurements are performed in conjunction with the topograph. With this added spatial dependence conductance measurement now are a function of the energy, *X* direction, and *Y* direction: $\frac{dI}{dV}(E,x,y)$. Conveying the response to these dependencies is inherently difficult. Data is often collected along straight lines as seen in figure 2.3 and displayed in what the author refers to as a conductance "line scan" (figure 2.3 C). This allows data to be represented in energy and distance with the color scale indicating the differential conductance. Often multiple conductance line scans are performed (STS grids) and are best represented in a video format, as slices in a 3D space (figure 2.3 D) similar to methods used for magnetic resonance imaging. Constant slices of energy are also useful to understand spatial structure in the LDoS (figure 2.3 E). Measurements at low temperatures are inherently slow due to the need to allow for piezo relaxation and hysteresis. Data acquisition times

are limited by the boil-off rate for liquid helium, requiring scanning to stop once in the dewar requires refilling.

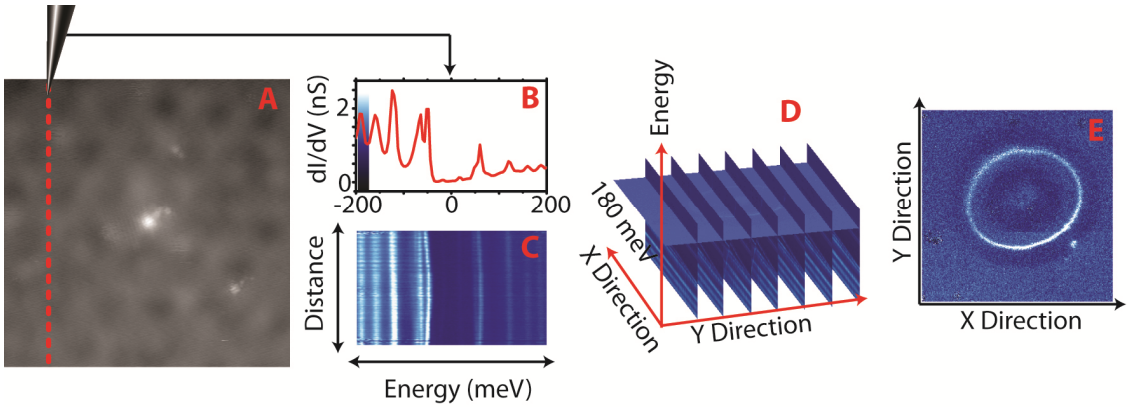

Figure 2.3: Methods of viewing STM and STS data. (A) A topograph near a defect. (B) Spectrum acquired at a single location. (C) Multiple spectra along the red dotted line displayed as a conductance line scan. (D) Multiple line scans stacked with a 3D space. (E) A conductance map extracted from the 3D data set at 180 meV.

Experimentalists will further probe systems by changing the magnetic field. This causes data to now depend on four variables, $\frac{dI}{dV}(E,x,y,B)$. Data can be acquired at fixed magnetic fields, where the tip is retracted when the magnetic field is changed. A new technique was developed in chapter 4 where conductance measurements are performed while the magnetic field is swept. This data was performed at constant energies and gives complementary results to constant magnetic field measurements.

2.2 Low Temperature Surface Characterization Chamber 1

The two systems utilized in this thesis have cryogenic chambers capable of running at 4.3 K. This low temperature greatly reduces thermal drift, allowing the study of a single location over several days with atomic precision. Most importantly low temperature allows for higher energy resolution in STS. Typically the energy resolution of dI/dV measurements is limited by the modulation amplitude, V_{mod}, and thermal broadening with the approximate relationship:[92]

$$\Delta E = \sqrt{(3.3kT)^2 + (2.5eV_{\text{mod}})^2}. \quad 45$$

This means that energy measurements become nearly 70 times more precise as $V_{\text{mod}} \to 0$ by reducing the temperature from 300 K to 4.3 K. In practice V_{mod} was set to ≤ 2 mV.

2.2.1 Georgia Tech Low-Temperature STM

Initial tunneling experiments were performed in a custom designed and constructed ultra high vacuum (UHV) cryogenic STM.[93, 94] Figure 2.4 shows a representative schematic. Tungsten tips were electrochemically etched using a zone electropolishing system under a microscope[95] which was found to give reliable results. Clipped Pt/Ir tips were attempted, but the technique was unreliable for the author. Two samples and a tip can be loaded into the load-lock and transferred into pressures of 10^{-10} torr within 12 hours. Using a modified wobble-stick, samples and tips are placed on a parking lot capable of holding up to 4 tips and 11 samples. Once placed in the UHV system the tip is locked onto a horizontal manipulator where a filament can be lined up (by eye) in front of the tip. In order to remove volatiles and oxides from the tip, an AC current of 4.0 A is then sent through the filament at a DC voltage of -1200 V. Tip heating for ~ 1 minute causes the pressure to rise to approximately 5×10^{-9} torr. Upon cooling, tips can be locked into a tip carrier stage and lowered onto the elevator in the STM.

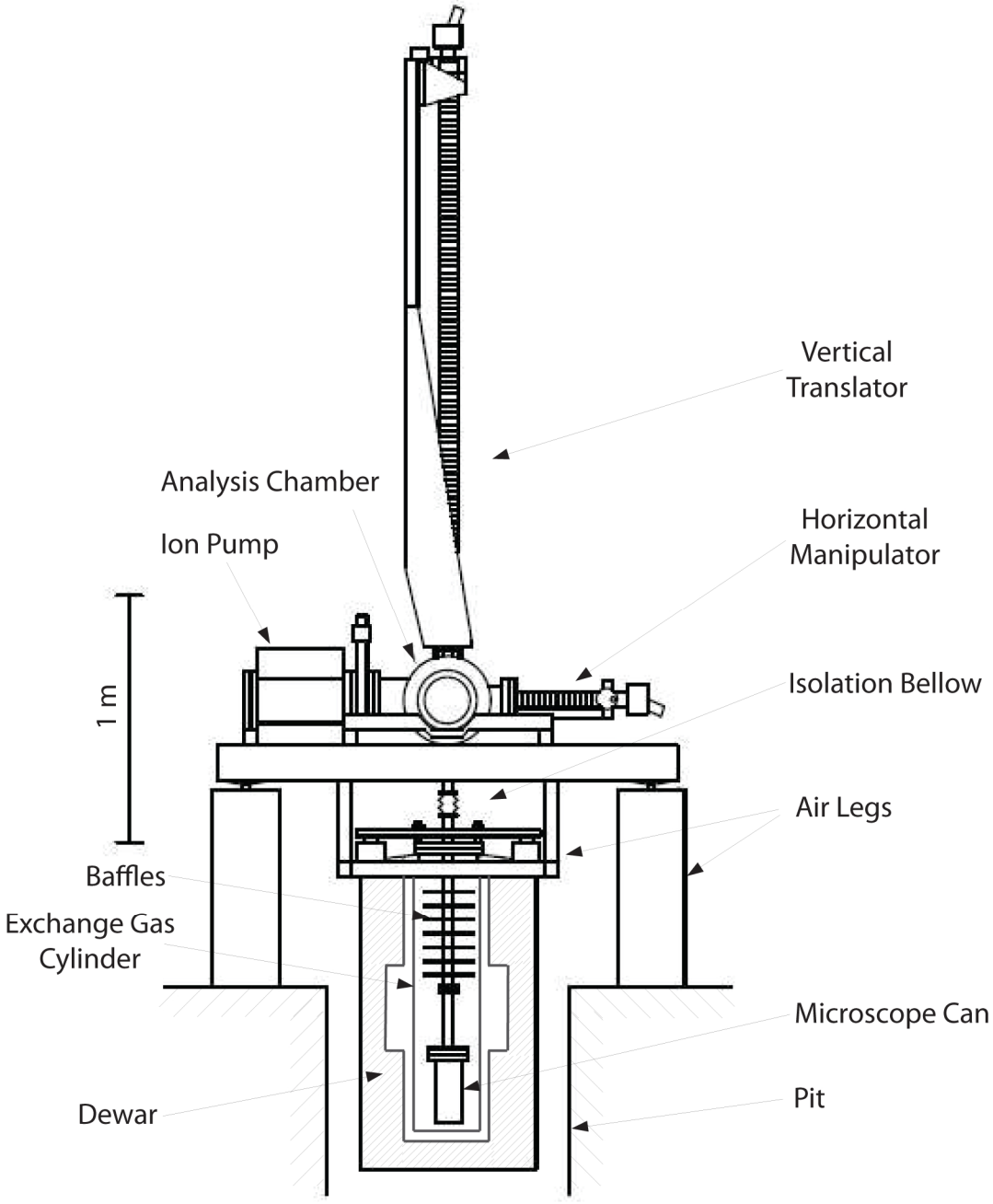

Figure 2.4: (Figure from ref. 93) A schematic of the low temperature UHV surface analysis chamber. This system is equipped with an electron-bombardment heater capable of graphitizing SiC at to 1450 C. Sample quality can be verified using LEED before transfer to the STM stage. Air legs, isolation bellows and 3 stage graphite-wool "springs" dampen the STM platform, removing most noise due to vibrations. Including sample prep time, STM investigations can begin with 36 hours of samples being placed into the load-lock system.

After transfer from the load-lock, sample preparation begins upon recovery of 10^{-10} torr by use of a titanium sublimation pump (TSP) and a cryopump. Infrared and optical pyrometers are used to monitor sample temperatures. A current of 4.0 A is administered to the sample heater filament, bringing temperatures to ~600º C. Continuous cryopumping is used to assist in pressure control throughout sample heating, but to prevent contamination the TSP filaments remain off once sample preparation begins. Approximately 200 *V* is applied to the filament resulting in an emission current of 120 mA which heats the sample to > 1200º C. Vacuum pressure is monitored via the ion pump, and sets the maximum rate for sample heating. Upon completion of heating, sample quality can be quickly studied using LEED,[64] which shows the sample's crystalline structure and domain rotations.

After cooling to near room temperature, samples are lowered onto the STM stage (figure 2.5). To prevent damage to piezos, special care must be used to ensure that contact occurs between the sample and its centering jig when placing the sample onto the STM stage. The system is then prepared for tunneling: isolation legs are filled with nitrogen gas to 40 psi and all loose parts are secured. The elevator can be lowered once the system is floating and electronics are on. Overload lights on the tunnel-current preamplifier should turn on and off briefly when the tip carrier touches the spherical contacts on the STM (this occurs when the elevator stage is 5 turns from the fully lowered position). If lights remain on, contact between the tip and sample has occurred and the tip will need to be replaced. Once the elevator is completely lowered, the shutter can be closed, preventing warm molecules from hitting the tip or sample. At this point the sample and tip must be allowed to cool. Typically, 4-6 hours pass before an approach with a walk-back of 200 steps is done. This type of approach is best started before leaving for the night and will allow the sample and tip to fully cool while getting the tip within 50 m of the sample. Upon approaching, extensive studies can be performed

using custom built electronics and software. For dI/dV measurements a Stanford Research model SR830 lockin amplifier is used in conjunction with a DL Instruments current preamplifier and a Stanford Research voltage amplifier. Tunnel current is initially converted to a voltage with a gain of 10^8 V/A and then sent to the lockin. In parallel, the signal is fed to the voltage amplifier where a low pass filter of 1 KHz to filter out the 5 KHz modulation is applied, in conjunction with an additional gain of 100 before entering the servo.

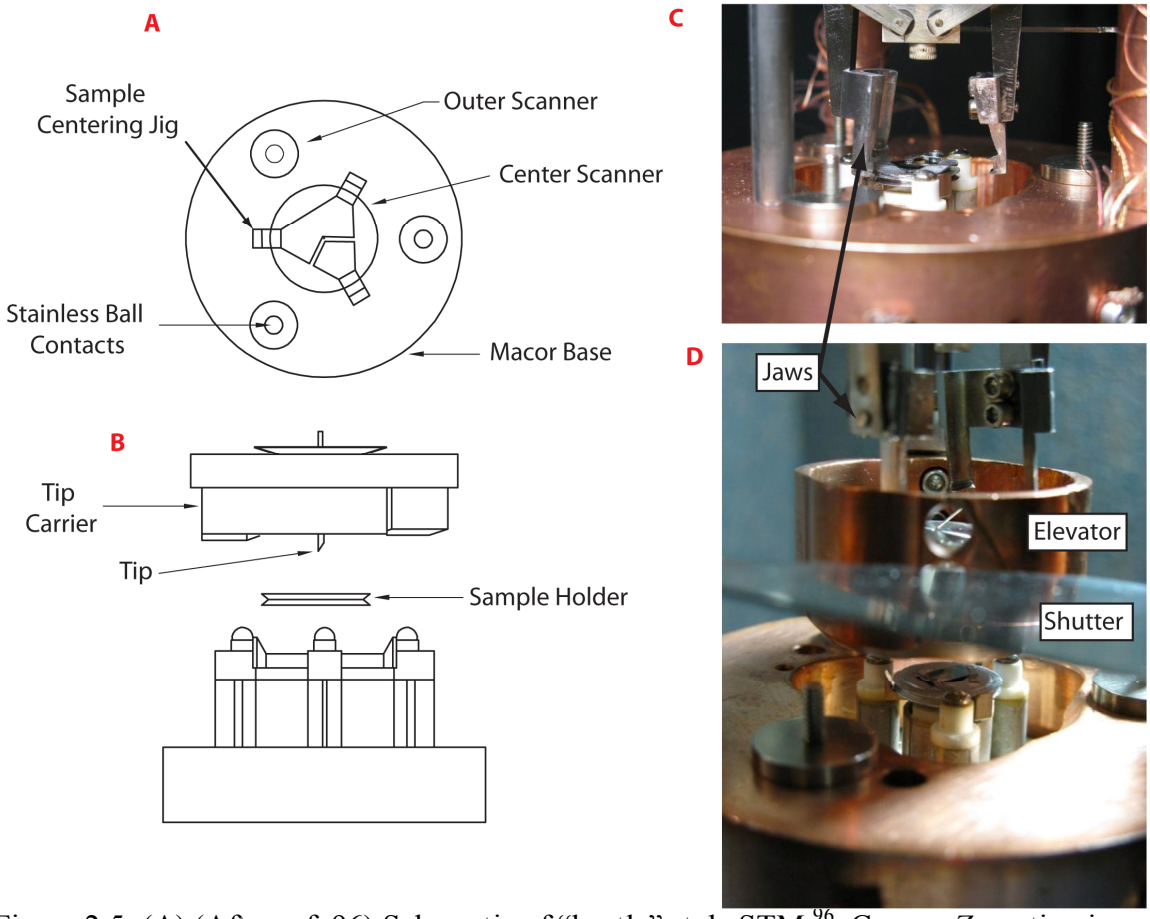

Figure 2.5: (A) (After ref. 96) Schematic of "beetle" style STM.[96] Course Z motion is controlled by three outer piezos, while fine scale motion is controlled by the center piezo. (B) (After ref. 96) Modifications to sample holder, tip carrier, and jaws were made to improve transfer efficiency and to accommodate thicker SiC samples. (C) Upon depositing a sample and (D) tip the elevator can be lowered, placing the tip carrier on the STM. To maintain thermal isolation and to prevent contamination from warm molecules, a metal shutter is placed over the STM.

2.2.2 Vibration Control

Vibration is a leading contributor to tunneling noise. This system's Newport high performance laminar flow isolators serve to decrease vibrations above 10 Hz by a transmissibility of 0.01. When these legs were not properly balanced, a 13-15 Hz resonance was occasionally found, which would ruin any atomic STM signal. Added weight, a filled dewar, and judicious use of cable ties all were employed to stabilize the system. In addition a graphite-wool pad was placed between stages on the STM to dampen high frequency vibrations (this material is conductive, so care was taken in its placement to avoid short-circuits to wire leads on the STM).

2.2.3 Improvements

Extensive noise reduction was performed on this system by the author. Multiple connections were rewired due to contacts breaking from repeated cooling and heating. (As a quick note to future users of the system, if capacitances between the piezos and ground are not correct [~2 nF] first check coaxial cables, and then suspect soldering on wires connected to multi-pin feedthroughs on the can.) Twisted pair wiring and a current preamplifier on the STM UHV housing were investigated for reducing noise, but the required redesign was deemed unpractical. A slimmer sample holder with a hole was designed to accommodate thicker SiC wafers and to facilitate heating. In addition the tip holder and jaws were redesigned for improved manipulation, resulting in a 100% success rate for all transfers. Caution must be used when picking up samples from the STM when a misalignment of the vertical translator exists from unlevel inner isolation bellows. Due to the non-symmetric nature of the jaws early contact can result, ruining any chance of grabbing the sample at predefined reference heights.

Several ground loops were eliminated, reducing the noise-in-signal substantially. Currently the servo, voltage preamp and IO-Tech analog output have nearly a 1 Ω

resistance placed between their grounds (this resistance was created by soldering multiple resistors in parallel). A more advanced redesign should be performed to ensure that resistance will decrease if a resistor fails, rather than increase. Ground fault interrupters increased ground loop noise and hence this extra safety measure is currently not used. Two suggested improvements not yet implemented on this system would be an active isolation system and an improved isolation bellows.

2.2.4 Overall System Effectiveness

This system is capable of obtaining atomic scale image at liquid helium temperatures. In addition this system was designed to perform ballistic electron emission microscopy[96] and consequently has electrical connections that could be repurposed to operate a gate electrode. Samples can be exchanged easily allowing for relatively fast and stable STM characterization and makes this system ideal for proof of concepts on samples before high magnetic field studies are performed at NIST. This system soon will employ a new RHK Technology servo controller. Coupled with the author's improvements this should put the system in its best condition ever, poised to perform interesting studies involving gated graphene and lithographically defined graphene structures.

2.3 Low Temperature Surface Characterization Chamber 2

This system is located at the National Institute of Standards and Technology, NIST, in Gaithersburg, MD. The author and his colleague David L. Miller were fortunate to be able to perform 6 months of data collection using this system. Most of the data contained in this thesis was collected during that time period and there still remains data to be analyzed. Unlike the beetle design of chamber 1, this system uses a Pan style[97] STM within a molybdenum module (figure 2.6) that holds both the tip and the sample. Tips are made of Ir wire, electrochemically etched to an end radius of ~10 nm. They are out gassed at higher temperatures once placed in UHV, and then cleaned using field

evaporation under a field ion microscope (FIM).[98] The studied 10 ± 1 layer epitaxial graphene sample grown on SiC $(000\bar{1})$, was resistively heated to 1180º C after having been heated to 1250º C at Georgia Tech. The sample and tip are then placed into the module and lowered liquid-helium cooled UHV cryostat. Sample and tip exchange requires four days due to the large mass of the module and the need to reach room temperature before any sample and tip exchanges can be performed. This is because the entire STM mechanics are located within the module and damage will occur to piezos or leads if all items are not at room temperature. The single module design along with active and passive vibration isolation systems eliminate most vibrational noise. Image registry to within a single atom can be maintained over a period of 4 days, and magnetic field studies can be performed up to 10 T in the *Z* direction and 1.5 T in the XY plane.

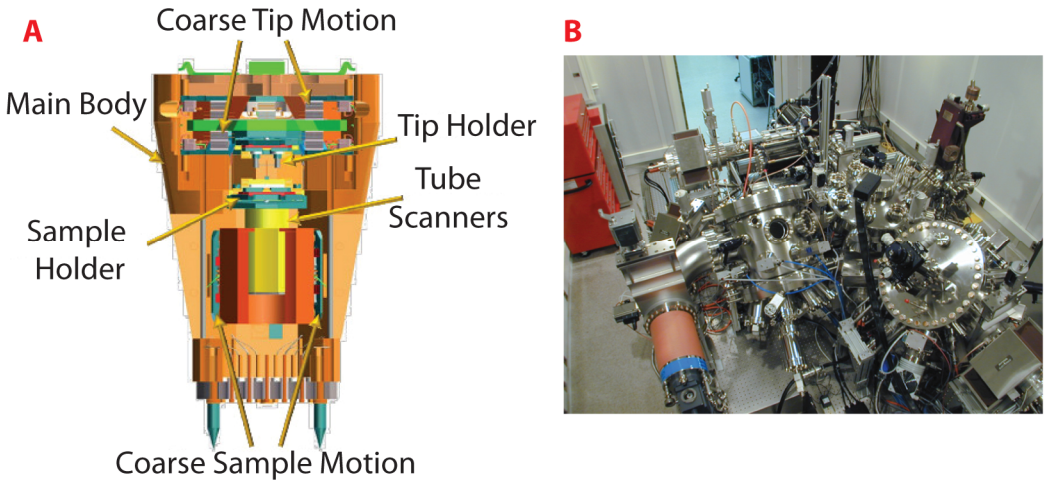

Figure 2.6: (Figure from ref. 98) Low temperature surface characterization chamber at NIST. (A) This system uses a module based STM. It is capable of magnetic field studies to 10 T and maintains atomic corrugation over 4 days while performing conductance studies. Due to its incredible stability this system is capable of tunneling while magnetic fields change, a new measurement investigated in chapter 4. The entire system (B) is enclosed in an acoustic faraday cage enclosure, removing as much external noise as possible.

The incredible stability of this system allows for precise conductance maps to be performed. For accurate STS data NIST uses a 465.7 Hz modulation of the bias voltage,

applied only during dI/dV acquisition. Time constraints such as waiting for the tip to settle after moving to a new position limits the number of points obtainable in any given time interval. For some of the studies in this thesis, conductance maps were performed at 251 positions x 251 positions x 101 energies, acquired at a fixed magnetic field over a period of ~ 65 hours. Settings would vary depending on the desired accuracy in energy and the tunneling conditions, but typical data acquisition variables for conductance measurements are presented in table 2.1.

Table 2.1: Typical spectroscopy settings used at NIST.

Voltage Set Point, V_{set}	0.35 V to 0.175 V
Tunneling Current Set Point, I_{set}	0.4 nA to 0.1 nA
Modulation Voltage, V_{mod} (amplitude of AC signal)	2 mV to 0.5 mV
Sensitivity (Sets gain on dI/dV measurements)	0.05 mV to 0.01 mV
Lock-in Time Constant	30 ms to 10 ms
Number of STS points	101 pts to 501 pts

2.4 Epitaxial Graphene Sample Preparation

To date the best method of growing multilayer epitaxial graphene is in a well calibrated low-vacuum induction furnace. Once grown, samples are mounted in atmosphere on molybdenum sample holders and then placed under UHV conditions. A particularly "dirty" sample is shown in figure 2.7 B. This sample was placed into the UHV chamber and was reheated to 800º C (figure 2.7 A) to remove any volatile adsorbates such as O_2. The remaining grey and white regions are believed to be amorphous carbon (no Si peak was found in Auger scans). Heating to $\approx 1250^{o}$ C is the only reproducible method to remove this layer. Nearly half of this particular amorphous carbon layer was removed by heating up to 1170 C (figure 2.7 C). Other samples (figure 2.7 D and E), when heated

to 1200º C, show little to no amorphous carbon. AFM studies do not show the presence of this layer. Its source it is still unknown, but it seems to be a graphitic residue from the furnace growth process. To prepare samples for STM/STS experiments, they are heated multiple times in UHV, each time increasing the temperature by 25º C to 50º C. While not ideal, to date this is the only reproducible technique that will remove the amorphous carbon layer, allowing graphene to be studied. The reheating process appears to have little to no effect on large scale structures such as pleats and pits seen in figure 2.7 D and E, but the top graphene layer may be left with more point defects than the underlying layers.

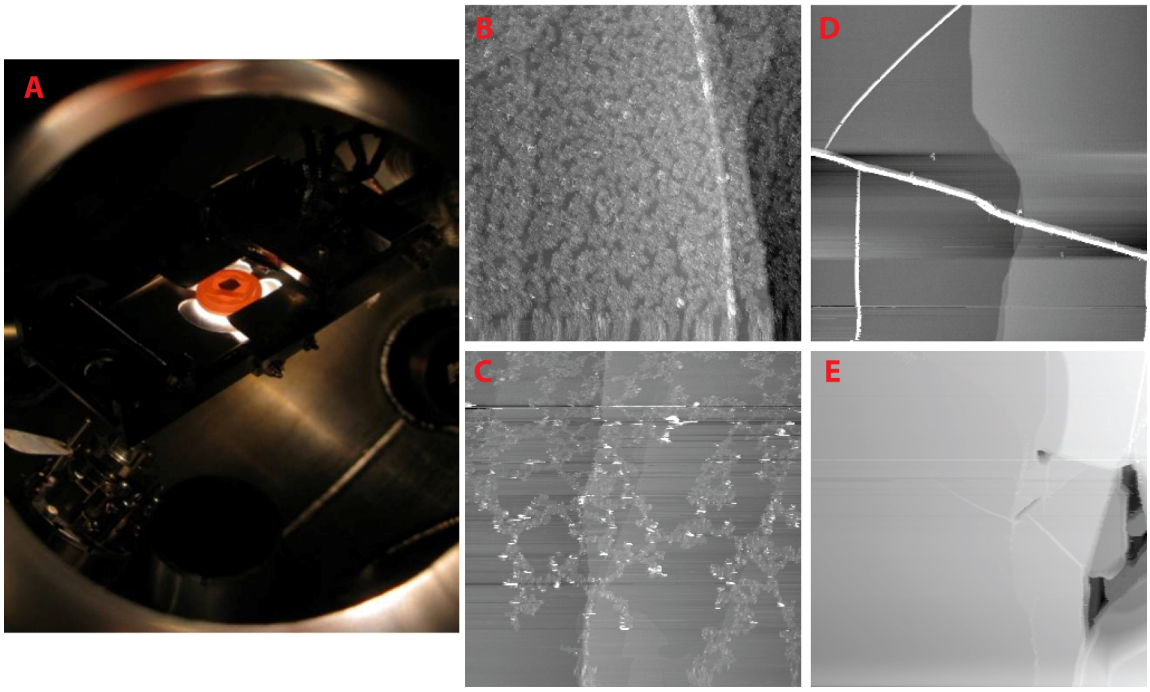

Figure 2.7: (A) Samples obtained from induction furnaces require reheating under UHV conditions. (B) This heating is performed to remove amorphous residue. (C) Samples are incrementally heated until the amorphous carbon is seen to migrate. (D) This technique allows for the study of nearly pristine graphene surfaces. (E) Pleats due to thermal expansion mismatch between SiC and graphene[65] are still present along with the occasional pit. [B: (800º C, ci6692, line subtracted topograph, sample bias $\left(V_{Bias}\right) = -1$ V, 9.8 nm black/white scale); C: (1170º C, ci6704, line subtracted topograph, $V_{Bias} = -1$ V, 9.0 nm black/white scale); D: (1200º C, ci6749 , line subtracted topograph, $V_{Bias} = -1$ V, 4.3 nm black/white scale); E: (1200º C, ci6752, line subtracted topograph, $V_{Bias} = -1$ V, 57.8 nm black/white scale)]

CHAPTER 3

CHARACTERIZATION OF LOCAL TIP EFFECTS

Distinguishing tip effects from defect effects in graphene was of vital concern throughout this thesis. It is only recently that tip effects were recognized to exist in published results concerning graphene, but when these tip effects were modeled they were treated as a constant capacitive term. [38, 74, 99, 100] Under ideal conditions, this approach results in LLs fitting equation 13 very well, but in some cases confusing asymmetries between electron and hole carrier velocities are also found.[74, 100] In addition, splitting of LL_0 at energies away from the Fermi energy was identified.[100, 101] The explanation of graphitic coupling contradicts results which indicate that LL_0 should remain a single state while higher index LLs should split.[101, 102] Since the infancy of STM it has been well understood that doping due to the tip would impact semiconductors.[103, 104] Theoretical models have been performed in multiple materials including Si, GaAs and InAs, with one such result being shown figure 3.1. [105] To date no such calculation has been performed for graphene and while confirmation of these types of theories is difficult due to the direct dependence of the tip's shape it would be a benefit to the graphene community. That said, multilayer epitaxial graphene has been shown to be a complicated system to model, requiring multiple screening layers and Hartree approximations.[99]

The majority of conductance spectra obtained by the author were more complicated than those previously reported.[74] In this chapter multiple simplified tip models will be fit to acquired data in an attempt to measure the local influence of the tip on graphene. Hopefully the results will spark interest for advanced theoretical work. With these models it will be shown that nearly all deviations from equation 13 are due to the local potential of the STM tip. Once the tip effect is accounted for other effects, such as the apparent velocity renormalization, are no longer present.

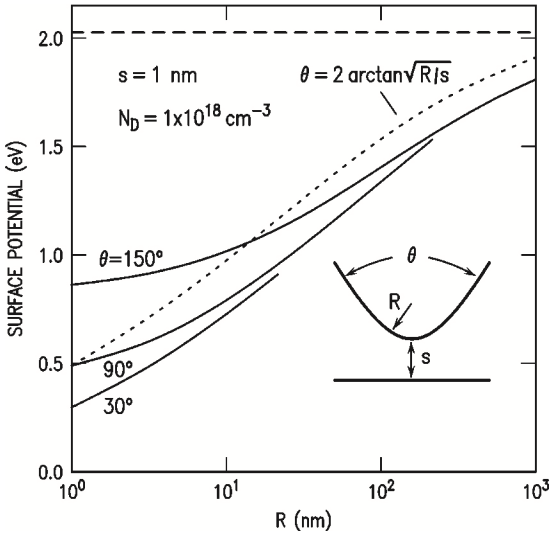

Figure 3.1: (Figure from ref. 105) Local potential doping effects on semiconductor are shown to depend on the width of STM tips.[105]

3.1 Microtip Classification

The spectra studied in this chapter were produced with the same (macroscopic) tip, in similar regions of the sample; however the microscopic tip configurations are apparently different. Applied voltage pulses or tip crash were used to induce "tip switches" which change the tip configuration. Each induced microtip displayed dramatically different tunneling responses. Therefore, while all originate from the same bulk tip, they will be referred to as tip 1, tip 2 and tip 3. Data from tip 1 was obtained when the tip was in its initial state, shortly after the tip approached. Before the approach, field emission microscopy (FEM) of the tip displayed a single point, indicating a sharp and well-ordered crystalline structure,[106] although it is unknown whether the final tip state upon approaching is exactly the same. Two tip changes occurred between tip 1 and tip 2. The first change occurred during the process of performing a field series (dI/dV at different magnetic fields) and was possibly due to a small tip crash. The second change occurred while the tip was scanned at a bias of 1 V. These combined tip changes resulted in tip 2. The transition from tip 2 to tip 3 was caused by pulsing the tip and scanning at 1 V.

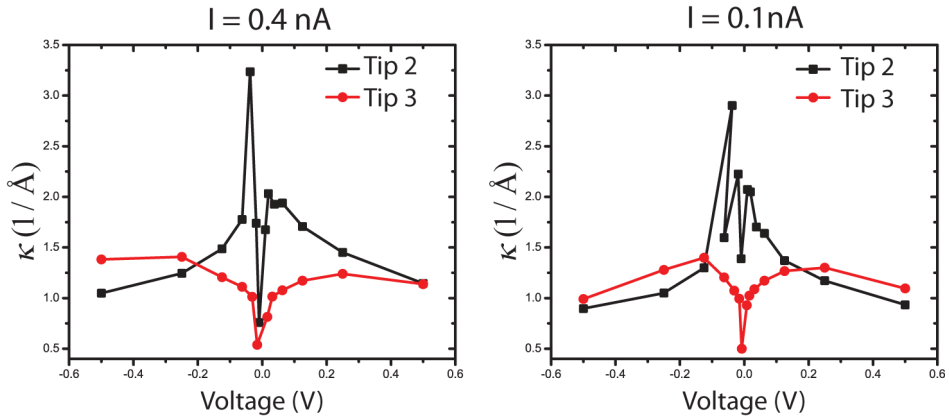

Figure 3.2: Extracted κ values from I vs. Z measurements performed with tip 2 and tip 3. The clear differences indicate that even though the macroscopic tip has not been changed, they behave as distinct tips. [tip 2: (L_25178 to L_25206); tip 3: (L_25386 to L_25411)]

From $I(Z)$ spectra the decay parameter κ was measured for tip 2 and tip 3, as shown in figure 3.2. While it is not exactly understood why κ increases for tip 2 as sample bias is decreased, it is seen that tip 3 behaves different where κ only decays as bias is decreased. It is known that contamination of the tip with carbonaceous flakes may occur while performing STM on graphite in ambient conditions,[107] but all measurements in the present work were performed in UHV conditions at 4.3 K. One can only speculate on the physical differences underlying the different $\kappa(V)$ functions measured from the tips, but whatever the cause, it is evident that tip 2 and tip 3 are different and as a result the measured dI/dV spectra are different. It is worth noting that tip 3 may have been less stable than tip 2; it suffered a tip-switch near the end of a magnetic field series. Tip 2 was stable over many days. It also should be noted that all conductance measurements in this chapter were obtained at a set point of 0.35 V where tip decay constants were of similar magnitude for all three tips.

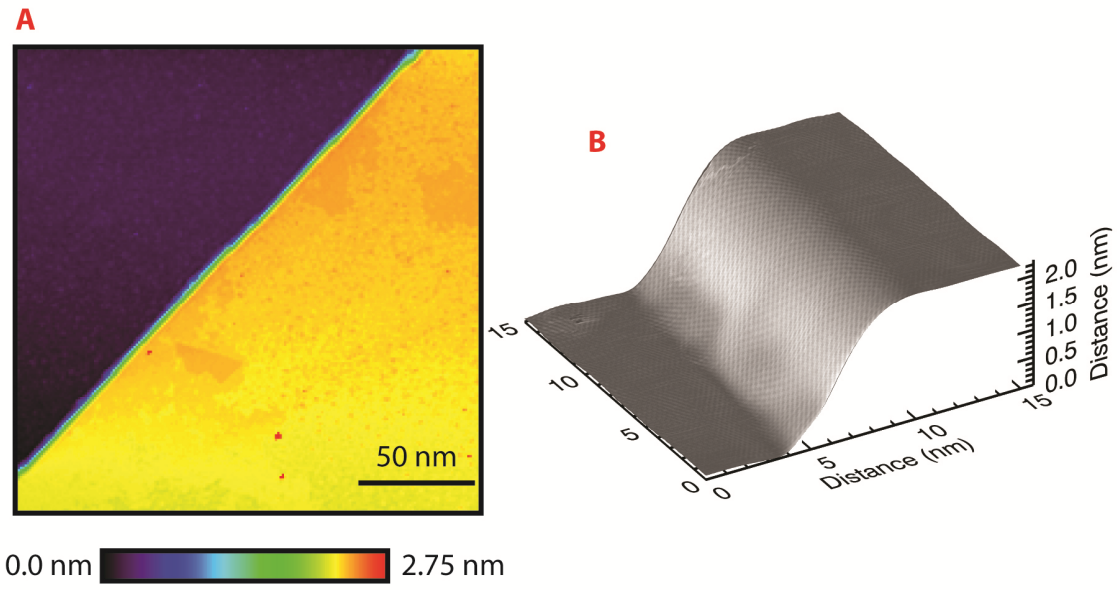

Figure 3.3: (A) A 2.2 nm step occurs between measurement locations performed for tip 1 and tips 2 and 3. It is possible this step is caused by 6 4H-SiC bilayers and the loss of 2 layers of graphene, which may explain the shift in the Dirac point seen from tip 1 to tip 2. (B) Atomic imaging shows the upper graphene layer to be continuous across the step. [A: (L_24389, 200 nm x 200 nm, 201 pts x 201 pts, $V_{Bias} = 1.0$ eV, $I_{set} = 0.1$ nA); B: (L_24403 15 nm x 15 nm, 301 pts x 301 pts, $V_{Bias} = 350$ meV, $I_{set} = 0.1$ nA)]

It is suspected that these tip changes should be considered macroscopic, but external tip characterizations methods such as SEM were not practical. If these are macro changes in the tip, the long range tip effects could differ dramatically.[105] While all spectra were performed on similar 4 nm moiré regions, tip 1 spectra were acquired on a terrace that was 2.2 nm lower than the region probed by tips 2 and 3 (figure 3.3). This height difference is most likely due to a step bunching of 6 4H-SiC bilayers (1.5 nm) and the loss of 2 graphene layers (0.68 nm). This possible difference in the number of graphene layers may explain the observed difference in LL_0 energies for these tips (-35 meV for tip 1, ≈ -5 meV for tips 2 and 3), since the large electron density at the SiC interface is better screened by thicker film.

3.2 Example Field Series Spectra

Several Landau level spectra can be seen in figure 3.4. A large electron-hole asymmetry in the tunnel conductance was typically observed in spectra obtained from tip 1 and tip 2. The conductance asymmetry was found to be dependent on the particular microtip. Small tip switches, believed to be caused by migrating atoms on the tip, would sometimes produce a much different dI/dV intensity ratio between electron and hole states. These atomic tip changes may change the local potential directly below the tip, but direct measurement of the tip-induced potential is generally not possible. Evidence presented in chapter 5 will show this asymmetry to be due to the tip potential. In the present chapter, the conductance asymmetry will be ignored, but an effective method for measuring the tip-induced potential will be developed. Investigations will focus on the explanation of extra peaks seen within low index LLs and the energy position of each LL (E_N) in relation to that expected for pristine graphene. (These effects only changed when tip changes were induced by crashing the tip into the surface or by pulsing a voltage $\geq 1\ V$ between the tip and sample.)

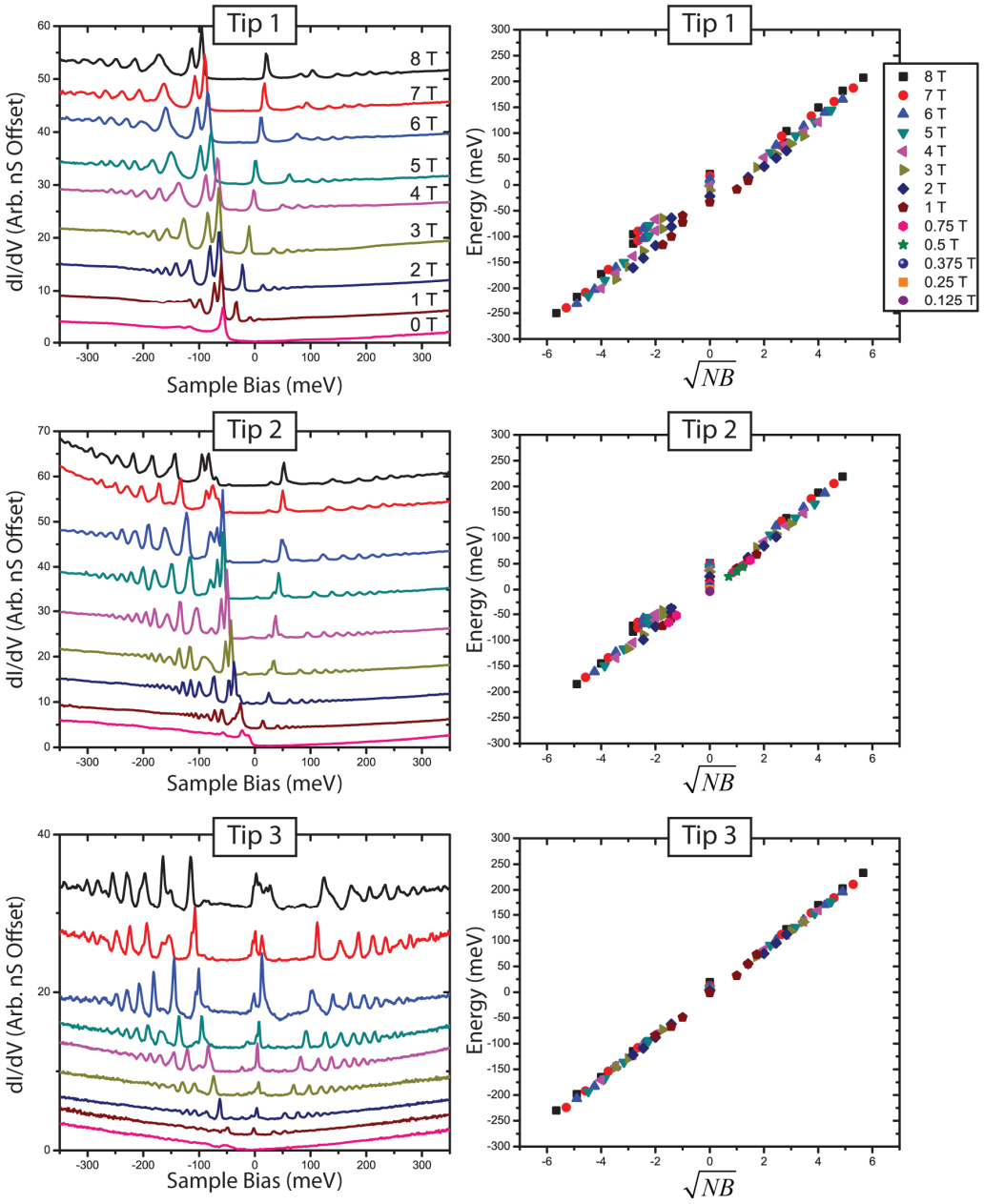

Figure 3.4: Three "magnetic field series" spectra and their extracted LL positions plotted as energy vs. $\sqrt{NB}$. All spectra were obtained from the same macrotip within 400 nm of one another. Large changes of the microtip occurred between each field series and the resulting effect on the spectra is apparent. Tip 3 resulted in spectra that fit equation 13 very well for nearly all LLs; while for tip 1 and tip 2 low index LLs are seen to deviate from a linear fit. In addition, new peaks are seen in LL_{-1} and LL_0. [Tip 1: (selected spectra from L_24459 to L_24945, 281 pts, $V_{set} = 350$ meV, $I_{set} = 0.4$ nA, $V_{\text{mod}} = 2.0$ mV.); Tip 2: (selected spectra from L_24885 to L_25042, 281 pts, $V_{set} = 350$ meV, $I_{set} = 0.4$ nA, $V_{\text{mod}} = 2.0$ mV.); Tip 3: (selected spectra from L_25286 to 25455, 601 pts, $V_{set} = 350$ meV, $I_{set} = 0.4$ nA, $V_{\text{mod}} = 1.0$ mV.)]

For all tips LL_0, shifts in energy as the magnetic field increases and crosses E_f. This shift has not yet been explained satisfactorily. It was originally attributed to a field-dependent screening of the interface by the graphene multi layer, although the role of the tip potential was also postulated.[74] The LL energies from tip 3 follow equation 13 quite well, when measured with respect to E_0, the energy position of LL_0. This suggests that the effect of the tip may be predominantly a (field-dependent) shift of the surface potential. But, using this technique on spectra from tip 1 and tip 2 does not result in a uniform $\sqrt{NB}$ dependence of the LL energies. Instead, subtraction of E_0 enhances an apparent electron hole asymmetry. (A similar asymmetry has been found by others,[101] and was interpreted as velocity renormalization for electrons and holes.) Extra peaks seen in high magnetic fields (figure 3.4) also are not explained by simple field-dependent shifts of the surface potential.

A more perplexing question is why changing the tip from 2 to 3 caused LL_0 to shift 40 meV, while LL_{-6} and LL_6 shifted only 10 meV at 6 T. If these results are attributed to a tip-induced potential, they show that lower index LLs are affected more than higher index LLs, i.e., inconsistent with a spatially uniform tip potential (similar energy dependence on LL index was shown in n-InAs (110) where LLs of higher index shifted less near defects[108]). This is not surprising if one considers the tip to be a cylindrically symmetric gate electrode, which creates a radius-dependent voltage across the surface. If the potential were known, then LL solutions in the symmetric gauge (chapter 1.3.3) could be used to calculate the perturbed LL energies. Since the exact tip-induced potential is unknown, the author will instead show that the observed LL energies can be used to effectively measure the tip-induced surface potential. This approach is similar in concept to the reconstruction of TIBB effects modeled using Hartree calculations in conjunction with semiconductor QD states caused by the tip.[109]

For the purpose of this thesis the effect of the tip-induced surface potential will be split into two parts. The first is a bias-dependent shift of the LDoS, similar to the

operation of a gate electrode. The second element is the two-dimensional form of the potential, which exists even at zero-bias because of the work function difference between graphene and the Ir tip.

The first effect is simple to extract from the data and will be discussed in section 3.3. The second effect is more complex to measure. At low magnetic fields the magnetic length is large, so LLs should only be slightly influenced by the local tip-induced potential. At high fields the magnetic length becomes comparable to the tip's potential well width, causing LLs to be modified in energy.

3.3 Direct Evidence of Bias Dependent Tip Effects

Tip interactions with samples have been well documented in other materials including graphite.[110, 111] In particular a term called the "lever arm", ξ, has been used to describe the ratio of the applied potential to the induced energy shift of the local density of states.[112, 113] In other contexts, the same effect is discussed in terms of a "quantum capacitance"[114] which describes the relation between the screening charge induced by a gate electrode and the shift of the energy states necessary to acquire this charge. The lever arm results from the voltage divider formed by the gate-sample (tip-sample) capacitance in series with the quantum capacitance. In order to observe this effect a state must be close to the Fermi energy such that the doping effect can pull the state across E_f, creating a new state for tunneling at higher bias referred to as a "mirroring" event.[113] In this thesis LLs and defect states were used to extract lever arm values independent of fitting procedures.

Figure 3.5 represents a typical LL state and its mirroring effect. In this conductance line scan, spectra are seen to be similar to tip 1 where LL_{-1} is split. Four mirroring states are seen when tip interactions pull the upper LL_{-1} state across E_f, creating additional peaks in the conductance measurement. Each mirror state can be reproduced

by reflecting the upper LL_{-1} peak across E_f and multiplying by the lever arm, 3.75. Observed lever arms on graphene varied from 3.75 to 20 depending on the tip.

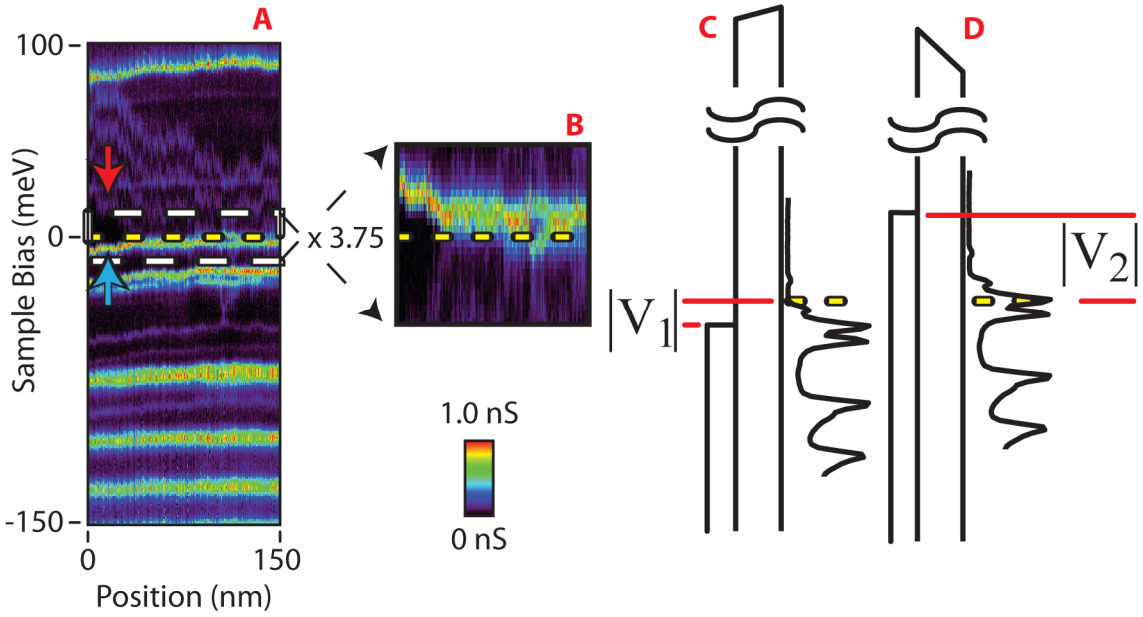

Figure 3.5: Measuring the lever arm effect. (A) (L_26021) A conductance line scan is shown. Here the doping potential pulls LL_{-1} (blue arrow) above the Fermi energy, creating mirror images (red arrow) at higher bias. (B) By mirroring across E_f and multiplying by 3.75, LL_{-1} is seen to match these mirror states. Mirror events are explained by the following: (C) When states are near E_f, there measured energy position is V_1. (D) Once the sample bias reaches $V_2 = \xi V_1$ LL_{-1} is pulled across E_f creating the mirrored state at V_2, which is due to tunneling into the newly unoccupied LL_{-1} state.

3.4 Extracting the Tip-Induced Surface Potential

The lever arm effect does not explain the observed splitting in low-index LLs or their peculiar energy dependence. Four mirrored states are present in figure 3.5 for the already split LL_{-1}, a 4-fold degeneracy believed to be due to spin and valley. This degeneracy splitting in the mirror states could be due to a charging energy, since the state is expected to be confined within a tip potential well.[115] A second possibility is that the spacing between mirror states indicated an enhanced splitting for spin and valley degeneracy once states cross E_f.[116] Whatever the cause, the degeneracy in each split peak indicates that

every peak must be treated as a LL. Each LL peak retains its 4-fold spin and valley degeneracy, so peak-splitting must be due to a loss of translation symmetry, hence the Landau gauge is not appropriate. In order to devise a simplified model of tip interactions two crucial assumptions will be made:

1) The tip-induced potential is cylindrically symmetric.
2) The tip-induced potential is constant for all magnetic fields.

Under these assumptions perturbation theory can be used with a model tip-induced potential, $V_{trial}(r)$, to calculate LL energies of the $|n,m\rangle$ states appropriate to the symmetric gauge.

3.4.1 Introduction to Model Potentials

In order to better understand the influence of the tip four tip potential models were used in this thesis:

1) Unscreened Point Charge Model
2) Gaussian Model of the Tip Potential
3) Screened Point Charge Model
4) Spherical Tip Model with Interface Screening

At high fields, energy spacing between LLs were assumed to be large and hence no states should have been present to screen tip effects. The first trial potential function treats the tip as an unscreened point charge located a height d_{tip} above the graphene surface along with a constant doping term E_d, due to interface and macro tip interactions.

Often literature models the tip effect as the second model, a Gaussian,[38, 109] and while this type of potential has no physical basis for graphene, it may provide a touchstone to other work. Furthermore, the short range of this potential may give an indication of how screening would modify the results.

The third model was used to attempt to incorporate results concerning screening in zero magnetic field in graphene.[117] The point defect will no longer be modeled using Coulomb's law, but instead there will be an additional logarithmic term in the denominator.

The fourth and most advanced tip geometry model undertaken treats the tip as a metal sphere while the n-doped interface layer is modeled as a grounded conducting plane. This model takes into account the following physics: 1) the STM tip has a finite size, 2) the top graphene layer screens poorly due to the discrete spectrum of LLs, and 3) the highly-doped layer(s) near the SiC interface will screen well even in high magnetic fields, since the LLs will be close in energy for large $\mathrm{E_f} - \mathrm{E_d}$ (for the conducting layer $\mathrm{E_f} - \mathrm{E_d} \approx 0.4\,\mathrm{eV}$).[99]

3.4.2 Isolated LL Approximation

Initially single 8 T spectra were fit. In this case results using degenerate perturbation theory can be viewed in figure 3.6. Using the unscreened point charge model the trial potential is:

$$V_{trial}(r) = E_d + \frac{Q}{4\pi\varepsilon_0\sqrt{r^2 + d_{tip}^2}}. \qquad 46$$

With this the matrix:

$$\sum_{n_1,m_1}\sum_{n_2,m_2}|n_1,m_1\rangle\langle n_1,m_1|V_{trial}|n_2,m_2\rangle\langle n_2,m_2| = \sum_{n_1,m_1}\sum_{n_2,m_2}|n_1,m_1\rangle\lambda_{n_1m_1;n_2m_2}\langle n_2,m_2|, \qquad 47$$

can be generated with equation 20 holding true. It should be noted that all potentials are displayed as an electron potential energy in this thesis ($V_{trial} > 0$ reduces the local electron density or increases the local hole density).

If the energy perturbation of $|\Delta E_N| >> |E_N - E_{N\pm1}|$ then, in the manifold of states with $|N| = n + \frac{|m|+m}{2}$, any state $|n,m\rangle$ will have little to no mixing with any "nearest

neighbor" state $|n',m'\rangle$ in the manifold of $LL_{N\pm1}$. This allows for first order degenerate perturbation theory with states only from LL_N. Thus for any given LL_N only $\lambda_{n,m} = \langle n,m|V_{trial}|n,m\rangle$ has to be calculated, since states of different m remain orthogonal (equation 17). As an added benefit the states from equation 15 will remain eigenstates of the new perturbed Hamiltonian. One can now combine the tip lever arm with the tip-potential, giving the new eigenenergies

$$E_{n,m} = \left(\frac{1}{1-1/\xi}\right)\left[\text{sgn}(N)c^*\sqrt{2e\hbar B|N|} + \lambda_{n,m}\right]. \quad 48$$

By using this relationship the measured $E_{n,m}$ states can have a least square fit performed to derive the best fit values for E_d, Q, d_{tip}, ξ and c^* in equation 46. A program was written using Interactive Data Language (IDL)[118] to construct V_{trial} and perform equation 48 for LLs $N=-4$ to $N=4$ for all states $|m|\le 5$. The results show (figure 3.6) that only states with $|m|\le 1$ were observable as separate peaks. In addition only LL_0, and $LL_{\pm1}$ in the model are split by an amount larger than the experimental peak widths, so that individual $|n,m\rangle$ peaks can be distinguished. For LLs where degeneracy splitting was undetermined, an average of the eigenenergies for states $|n_1,1\rangle$, $|n_2,0\rangle$, and $|n_2,-1\rangle$ (where $n_1+1=n_2=|N|$) was used. An IDL fit procedure written by Craig B. Markwardt[119] which performed the Levenberg-Marquardt minimization algorithm[120] was used to fit equation 48 to the measured LL energies. Each energy peak position was extracted from LL spectra using a Lorentzian model in Origin Pro,[121] and the minimum energy resolution of 1.75 meV (equation 45) was assigned to uncertainty values for least-chi-square fits.

Fourteen peaks were identified in the 8 T spectra shown in figure 3.6 and the resulting fit gave $E_d = -21\,\text{meV}$, $Q = 0.58\,e$, $d_{tip} = 7.1\,\text{nm}$, $\xi = 8.6$, and $c^* = 0.996 \times 10^6\,\text{m/s}$ with a normalized chi-square value, $\langle \chi \rangle^2 / \text{DoF} = 8.8$, with the degrees of freedom (DoF) defined as the number of fit values minus the number of fit parameters. While this model (red rings figure 3.6) seems to explain the peaks for a single magnetic field, it does not fit as well at lower fields in the field series. In order to improve the fits a mixing of states from different LLs must be included.

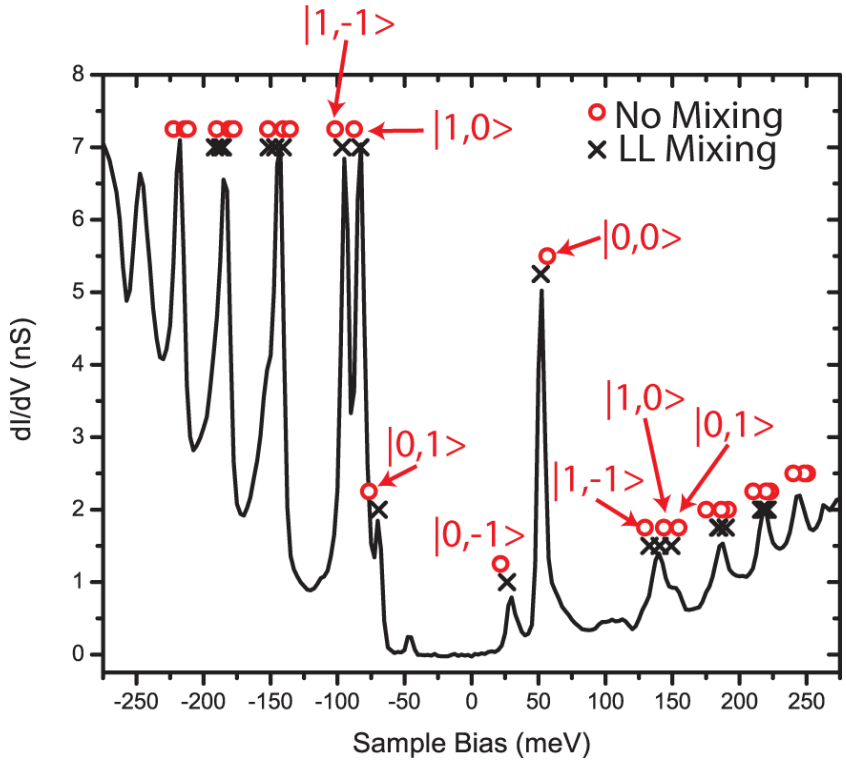

Figure 3.6: 8 T Spectra obtained with tip 2. The tip is treated as a point source (equation 46). Using degenerate perturbation theory (red), $|n,m\rangle$ states in the symmetric gauge are observed. An improved approximation accounts for interaction between nearest neighbor LLs (black X). [(L_24889, 281 pts, $V_{set} = 350$ meV, $I_{set} = 0.4$ nA, $V_{\text{mod}} = 2.0$ mV)]

3.4.3 LL Mixing Approximation

At lower magnetic fields the assumption, $|\Delta E_N| >> |E_N - E_{N-1}|$, is no longer valid. Ideally one would construct the entire $|n,m\rangle$ Hamiltonian and find its eigenvalues and eigen vectors. Unfortunately since eigenvectors depend directly on the potential and a nearly infinite number of $|n,m\rangle$ states, this procedure is unrealistic. In order to deal with this problem the assumption $|\Delta E_N| >> |E_N - E_{N-2}|$ was made, allowing for only energetically nearest neighbor LL interactions.

As a result the following Hamiltonian can be constructed to predict the new eigenenergies:

$$\mathbf{H}_0 + \mathbf{H}_1 = \sum_{n_1,m_1} |n_1,m_1\rangle \mathrm{sgn}(N) c^* \sqrt{2e\hbar B|N|} \langle n_1,m_1| + \sum_{n_1,m_1} \sum_{n_2,m_2} |n_1,m_1\rangle \lambda_{n_1 m_1; n_2 m_2} \langle n_2,m_2|, \qquad 49$$

where the states $|n_1,m_1\rangle$ and $|n_2,m_2\rangle$ reside in N, $N-1$ or $N+1$. The energy dependence of each unknown state is extracted by diagonalizing the matrix and selecting the energies corresponding to the LLs in N. An example for LL_0 when only concerned for states with $|m| \le 1$ is:

$$\mathbf{H}_0 + \mathbf{H}_1 = \begin{bmatrix} -E_1 + \lambda_{0,1;0,1} & 0 & 0 & 0 & 0 & 0 & 0 & 0 \\ 0 & -E_1 + \lambda_{1,0;1,0} & 0 & \lambda_{1,0;0,0} & 0 & 0 & 0 & 0 \\ 0 & 0 & -E_1 + \lambda_{1,-1;1,-1} & 0 & \lambda_{1,-1;0,-1} & 0 & 0 & 0 \\ 0 & \lambda_{1,0;0,0} & 0 & \lambda_{0,0;0,0} & 0 & 0 & \lambda_{1,0;0,0} & 0 \\ 0 & 0 & \lambda_{1,-1;0,-1} & 0 & \lambda_{0,-1;0,-1} & 0 & 0 & \lambda_{1,-1;0,-1} \\ 0 & 0 & 0 & 0 & 0 & E_1 + \lambda_{0,1;0,1} & 0 & 0 \\ 0 & 0 & 0 & \lambda_{1,0;0,0} & 0 & 0 & E_1 + \lambda_{1,0;1,0} & 0 \\ 0 & 0 & 0 & 0 & \lambda_{1,-1;0,-1} & 0 & 0 & E_1 + \lambda_{1,-1;1,-1} \end{bmatrix} \qquad 50$$

where $E_1 = c^* \sqrt{2e\hbar B}$. The resulting eigenvalues could be sorted and the 4th and 5th highest energies would correspond to the new LL_0 states. This energy selection method is appropriate as long as LL_N energy states do not cross nearest neighbor $LL_{N\pm1}$, an event that did not occur for all potential fits. In addition this method does not contain any reiterative measures, meaning that while LL_{-1} is changed by LL_0 and LL_{-2}, the unperturbed forms of LL_0 and LL_{-2} were used instead of the new states due to their own interactions with nearest neighbors.

The resulting energy values from a fit using this approach performed at 8 T are labeled in figure 3.6 as the black Xs. The extracted parameter values are $E_d = -7.6$ meV, $Q = 0.22\ e$, $d_{tip} = 2.9$ nm, $\xi = 12.9$, and $c^* = 1.06 \times 10^6$ m/s resulting in $\langle \chi \rangle^2 / \text{DoF} = 2.2$. For such a simplified tip potential this normalized chi-square value is astounding. The LL mixing model is appropriate for the entire range of magnetic fields investigated.

3.4.3.1 Unscreened Point Charge Model

Results from fits of complete field series using the unscreened point charge model tip potential (equation 46) and allowing nearest neighbor LL mixing are shown in figure 3.7. Each data point has been included as a black dot, with dot size being bigger than uncertainty bars. The resulting fit is seen in yellow. Table 3.1 has been included to present the best-fit parameter values. These results show how well this method fits for all field spectra. In particular these results explain magnetic field dependence of LL_0. Slight discrepancies can be seen in tip 1 in LL_{-1} for fields less than 4 T, and in tip 3 for 8 T. The two most likely reasons are either effects due to charge rearrangement between layers, or that tip changes occurred in the process of retracting, changing the field and reapproaching. It is believed that these deviations are more likely tip micro state dependent, since tip 2 (the most stable tip) is seen to have the best fit.

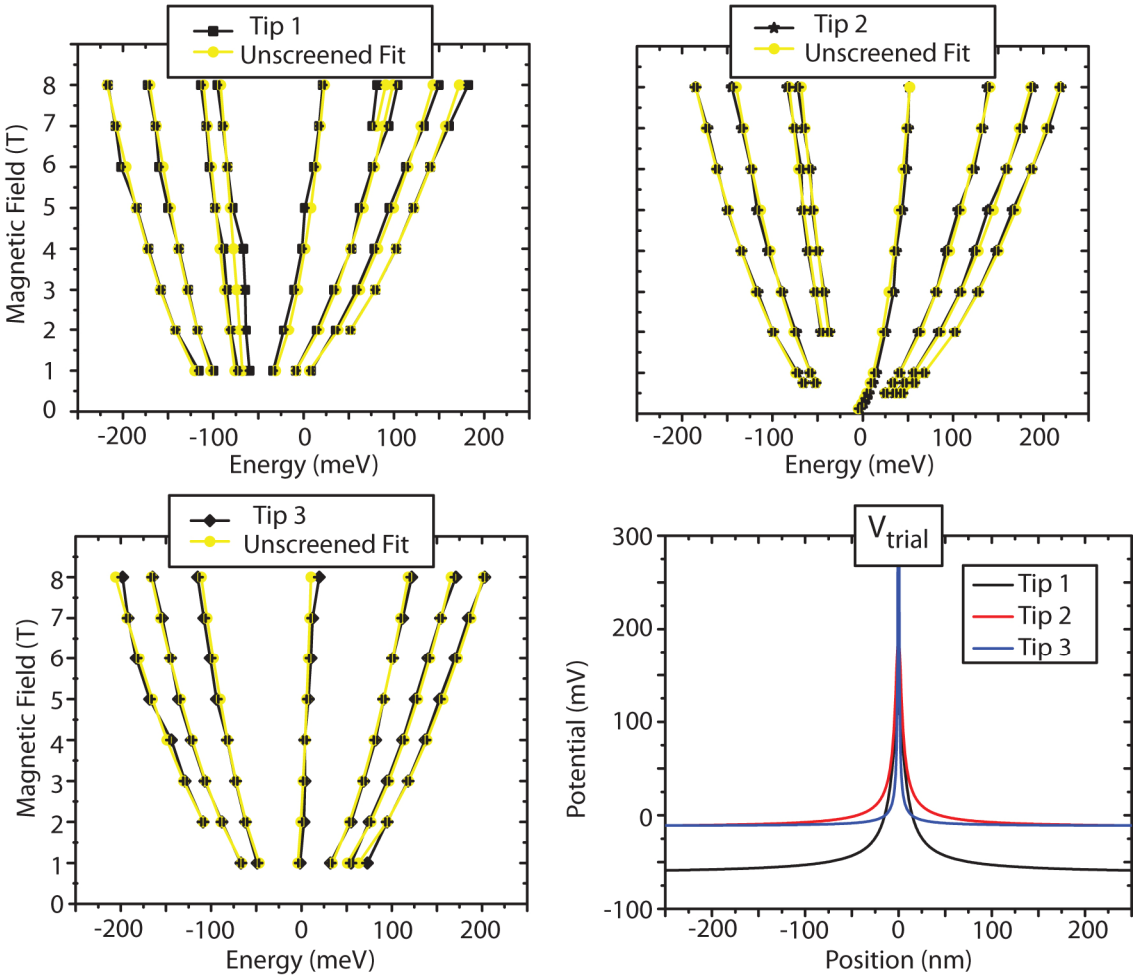

Figure 3.7: Measured (black) and fit (yellow) LL positions using the unscreened point charge model of the tip potential (equation 46). An excellent fit is found for nearly all fields, supporting the conclusion that LLs are perturbed by the local potential of the STM tip. Extracted potential for tips 1 and 2 are nearly identical, except for a 50 meV offset, which could be due to the difference in the number of graphene layers between the two locations. Tip 2 and tip 3 probed the same graphene terrace, consistent with their similar values for E_d. However, the potential from tip 3 appears to be more localized near the origin.

Table 3.1: Results from unscreened point charge model.

Tip	E_d (meV)	$Q\,(e)$	d_{tip} (nm)	ξ	$c^*\left(10^6\ \mathrm{m/s}\right)$	$\langle\chi^2\rangle$	$\frac{\langle\chi^2\rangle}{\mathrm{DoF}}$
1	-63	0.68	5.6	9.8	1.00	333	5.5
2	-13	0.41	2.9	11.8	1.04	114	1.7
3	-11	0.11	0.246*	9.9	1.03	170	3.3

The resulting tip potentials are shown in figure 3.7. The similarity in E_d for tip 2 and tip 3 is reassuring since to both were acquired within 100 nm of each other, while the lower value of E_d for tip 1 is consistent with fewer graphene layers between the tip and SiC interface. In addition, the potential from tip 3 has a more confined form. It should be emphasized that the spatial precision for potentials is limited by ℓ_B, i.e., the form of the potential cannot be determined accurately for $r \leq \ell_B$, since the wave function size is $\sim \ell_B$ ($\ell_B = 9.2$ nm at $B = 8$ T).

3.4.3.2 Gaussian Model of the Tip Potential

For the Gaussian model the trial function is now of the form:

$$V_{trial}(r) = E_d + A\,\mathrm{e}^{-r^2/2\sigma^2}. \qquad 51$$

Results are shown in figure 3.8 with extracted parameter values in table 3.2.

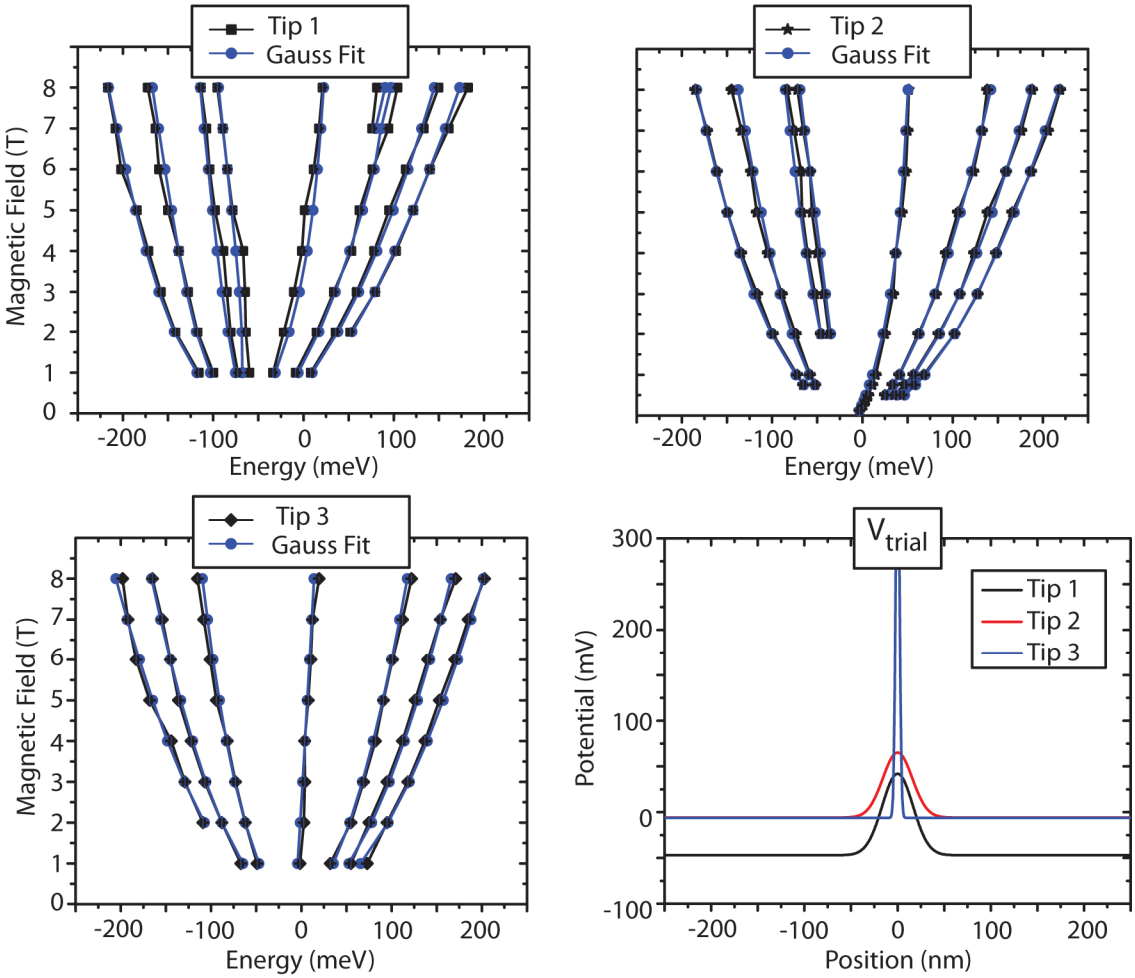

Figure 3.8: LL peak positions (black) for tips 1, 2, and 3 and the corresponding best fits (blue) using the Gaussian tip model. Tip 1 and tip 2 are seen to have a poorer fit than the point charge model, while tip 3's has improved. Resulting parameters indicate that the tip 3 potential is large and short-ranged.

Table 3.2: Results from Gaussian model. †minimum bound value set from observed line scans.

Tip	E_d (meV)	A (meV)	σ (nm)	ξ	$c*\left(10^6 \text{ m}/\text{s}\right)$	$\langle\chi^2\rangle$	$\frac{\langle\chi^2\rangle}{\text{DoF}}$
1	-47	89	16.4	8†	0.97	358	5.9
2	-6	71	15.7	12.3	1.05	154	2.3
3	-6	421	2.05	8†	1.00	159	3.1

Fits for tips 1 and 2 have chi-square values noticeably larger than those for the point charge model. In addition, the minimum lever arm, 8, (set by observed line scans)

was quickly reached in the fitting. This alone indicates that the Gaussian model is not accurate. LL positions still underwent similar energy shifts and the Dirac point for each tip, while slightly closer to E_f, was similar to the results from the point charge model.

Table 3.3: Investigating tip 3's results from the Gaussian model for fixed σ values. Here the chi-square value is seen to increase by nearly 20% when the FWHM of the potential is forced to be similar to the width of tips 1 and 2.

σ (nm)	E_d (meV)	A (meV)	ξ	$c*\left(10^6 \text{ m}/\text{s}\right)$	$\langle\chi^2\rangle$	$\frac{\langle\chi^2\rangle}{\text{DoF}}$
5	-6.9	87	13.8	1.06	163	3.1
10	-7.6	33	12.6	1.05	176	3.4
15	-8.5	23	7.8	1.00	185	3.6

Tip 3 was seen to fit better using this Gaussian form. Additional fits were performed (table 3.3) with bound widths, indicating that for the Gaussian to fit best a full width half max (FWHM) ~5 nm was numerically preferred with a large potential present directly below the tip. Unfortunately with the magnetic length dependence it is impossible to show if this localized high potential effect is present.

3.4.3.3 Screened Point Charge Model

For the screened point charge model the trial function is now of the form:

$$V_{trial}(r) = E_d + \frac{Q}{4\pi\varepsilon_0\sqrt{r^2+d_{tip}^2}\,\ln\left(\sqrt{r^2+d_{tip}^2}\,/a\right)} \qquad 52$$

The resulting fit data can be seen in figure 3.9 with the fit parameters in table 3.4.

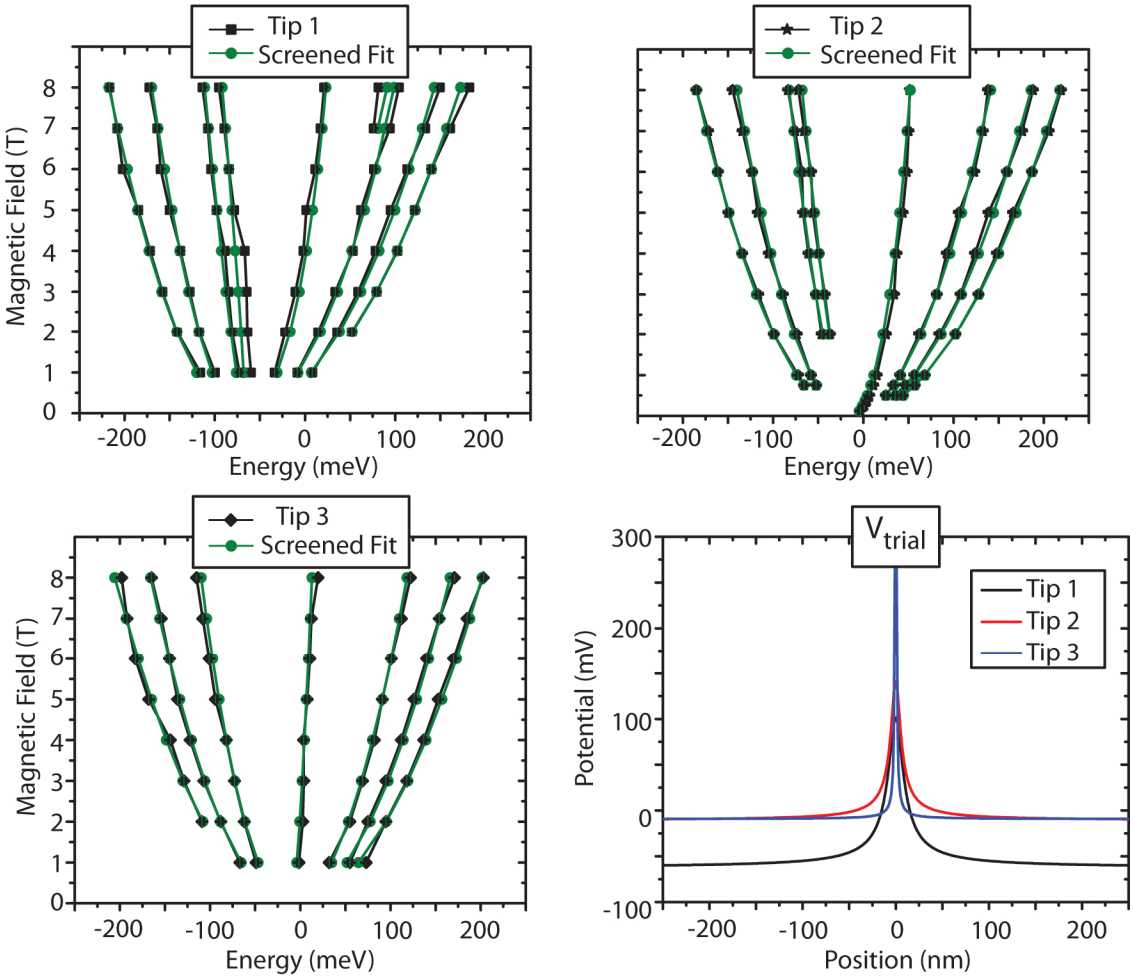

Figure 3.9: LL peak positions (black) for tips 1, 2, and 3 and the corresponding best fits (green) using a screened point charge. Results are slightly better than the unscreened point charge model, but fit potentials are nearly identical, indicating a confined potential within 25 nm of the tip which slowly decays to the Dirac point.

Table 3.4: Results from screened tip model. †lower bound

Tip	E_d (meV)	$Q\,(e)$	d_{tip} (nm)	ξ	$c^*\left(10^6\ \mathrm{m/s}\right)$	$\langle\chi^2\rangle$	$\frac{\langle\chi^2\rangle}{\mathrm{DoF}}$
1	-63	3.12	8.0	18.6	1.05	330	5.4
2	-11	1.7	5.5	8.2	1.00	112	1.6
3	-8	0.24	0.246†	9.6	1.03	158	3.1

Results similar to the unscreened model were obtained, but tip 3 reached a minimum boundary condition for d_{tip}. Extensive result analysis will be reserved for section 3.4, but tip 1's and tip 2's local potential were found to be localized within a 25 nm radius with a slightly lower maximum value at the origin than the unscreened point charge model. In addition chi-square values have slightly improved from the unscreened point charge model for these tips, indicating that some screening is likely occurring in the system.

3.4.3.4 Spherical Tip Model with Interface Screening

A schematic in figure 3.10 identifies this model's additional parameters. Because the parameters are interdependent convergence of these calculations was slow, and it is not certain whether the true minimum was found for this model. Reproducible minimized fit results were compared by performing multiple fits with different realistic initial conditions. If conflicting results with similar chi-square values were found the relative trial step size was increased in an attempt to sample a larger parameter space. Over 7000 iterations were performed for each fit using the sphere-tip model. In each iteration over 250 $\lambda_{n_1,m_1;n_2,m_2}$ calculations were performed for each magnetic field. This means that for each iteration an integration was performed for over 6500 perturbations on partial state functions (equation 17) of 20,001 elements. Due to the large amount of calculations up to 5 days of computation was needed to reach convergence. This limited the number of repeat fits to be performed for this model, but results were found to reproduce for multiple initial conditions. The calculation time could be reduced by decreasing the number of states included in the Hamiltonian. For all calculations shown, states with $|m| \leq 5$ were included.

The solution of the spherical geometry can be extracted using the method of images. It involves an infinite number of image charges to be placed inside the sphere,

and across the conductive plan (figure 3.10). To solve this solution analytically, a cutoff charge is needed, where the remaining sum of image charges to infinity can be obtained from a single effective charge.[122]

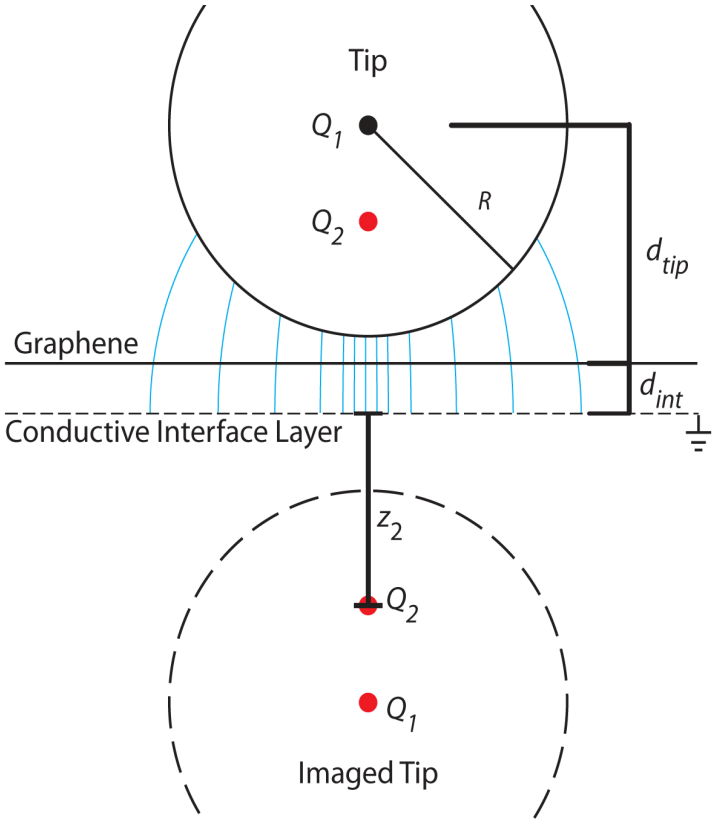

Figure 3.10: A schematic of the spherical-tip model. Here the work function difference was modeled as a point charge Q in the center of a sphere a distance d_{tip} from the surface. The method of images is used with the grounded conductive interface plane. The top graphene layer has little effect on the electric field lines (blue), while the conductive interface layer terminates all field lines.

To construct this potential the following routine was used:

First initial conditions were set.

$z_k = d_{tip} + d_{\text{int}}$; the total length from the center of the sphere to the conducing interface layer.

$\alpha_k = 2\dfrac{d_{tip} + d_{\text{int}}}{R}$; a variable used to set future image charges and distance.

$Q_k = Q$; the initial charge.

$V_{trial}(r)=\frac{Q_k}{4\pi\varepsilon_0}\left[\frac{1}{\sqrt{r^2+\left(z_k-d_{int}\right)^2}}-\frac{1}{\sqrt{r^2+\left(z_k+d_{int}\right)^2}}\right]+E_d$; the first two potentials (original charge, and image charge) are constructed.

For the next 99 image pairs the following loop was performed:

$Q_k=\frac{Q_k}{\alpha_k}$; the new charge resulting from the previous image charge.

$z_k=R\left(\frac{d_{tip}+d_{\text{int}}}{R}-\frac{1}{\alpha_k}\right)$; the new location of the charge.

$\alpha_k=2\frac{d_{tip}+d_{\text{int}}}{R}-\frac{1}{\alpha_k}$; the new fractional constant is prepared for the next iteration.

$V_{trial}(r)=\frac{Q_k}{4\pi\varepsilon_0}\left[\frac{1}{\sqrt{r^2+\left(z_k-d_{int}\right)^2}}-\frac{1}{\sqrt{r^2+\left(z_k+d_{int}\right)^2}}\right]+V_{trail}(r)$; the two new induced charges are added to the old potential.

The loop is then repeated and once the maximum number of image pairs is reached, the rest of the sum is treated as a single point where:

$z_\infty=R\sqrt{\left(\frac{d_{tip}+d_{\text{int}}}{R}\right)^2-1}$; the location of the effective summed image charge.

$\alpha_\infty=\frac{d_{tip}+d_{\text{int}}}{R}+\sqrt{\left(\frac{d_{tip}+d_{\text{int}}}{R}\right)^2-1}$; the final ratio needed to calculate the induced charge.

$Q_\infty=\frac{Q\alpha_\infty}{\alpha_\infty-1}$; the last image charge.

$V_{trial}(r)=\frac{Q_\infty}{4\pi\varepsilon_0}\left[\frac{1}{\sqrt{r^2+\left(z_\infty-d_{int}\right)^2}}-\frac{1}{\sqrt{r^2+\left(z_\infty+d_{int}\right)^2}}\right]+V_{trial}(r)$; the last two point charges are added to the potential.

The resulting fits are shown in figure 3.11, with the numerical results in table 3.5. The fits appear to be slightly better for tips 1 and 2 when compared to fits performed with the screened and unscreened point charge models. Although, with the two added parameters the normalized chi-square values are slightly larger. The resulting potential for tip 3 has a diminished effect near the origin which is known from the Gaussian fit to cause higher chi-square values. Again it is unknown what the potential truly is for a radius below 9.2 nm, but it is the author's belief that the potentials resulting from this model are the closest to the actual potential.

While this model is much more complex, results extracted appear to agree with the other models and observations. The lever arm matches observed values obtained near defects in other line scans and the tip sample distance of 1 Å to 2 Å was similar to results obtained from I vs. Z measurements. In addition, these results indicate that the tip is ~60 nm wide, well within the range of expected values for the macro tip. The interface distance was smaller than the expected ~3.4 nm, but this result was anticipated given the intervening doped graphene layers between the top layer and the interface layer; these will also contribute to screening. Additionally, the interface distance d_{int} is smallest for tip 1, agreeing with the hypothesis of fewer graphene layers. The extracted Dirac point also agrees with this picture, showing a difference in doping of ~45 meV. The potential on the sphere due to the charge would be 0.90 V for tip 1 and 0.12 V for tip 3. This may be due to a change in the work function difference between graphene and the Ir tip. Note that work function difference between graphite (HOPG graphite 4.48 eV)[123] and Ir (5.27 eV)[124] is 0.79 eV, close to the potential found for tip 1. It is possible that the work function decrease was due to graphene being picked up by the tip, but unfortunately tip conditions are not known.

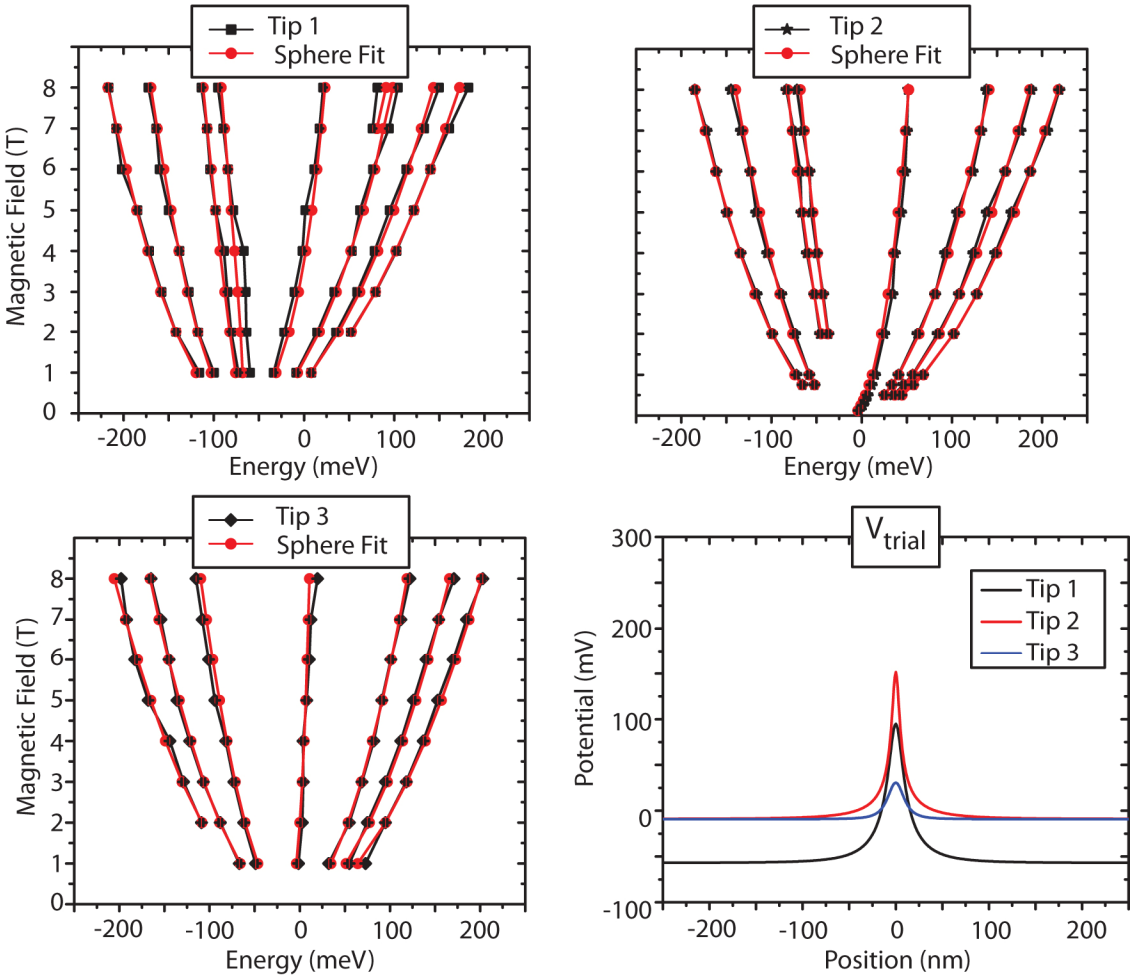

Figure 3.11: LL peak positions (black) for tip tips 1, 2, and 3 and the corresponding best fits (red) using the spherical tip with a conductive interface layer model. Results are similar to screened and unscreened point charge models, but the local potential at the origin is smaller.

Table 3.5:Results from the spherical tip model.

Tip	E_d (meV)	$Q\,(e)$	d_{tip} (nm)	ξ	$c^*\left(10^6\ \mathrm{m/s}\right)$	d_{int} (nm)	R (nm)	$\langle\chi^2\rangle$	$\frac{\langle\chi^2\rangle}{\mathrm{DoF}}$
1	-54	18.8	29.9	15.3	1.04	1.04	28.8	327	5.5
2	-7.6	7.5	29.1	10.3	1.03	1.34	29.0	112	1.7
3	-9.8	2.5	28.9	10.0	1.03	1.37	28.7	180	3.7

3.5 The Total Effect of the Tip

It is nearly impossible to state which model is best in modeling the tip. But, by looking at figure 3.12 it is obvious that the best-fit potentials obtained from the spherical-tip and both point-charge models are nearly identical. Tip 2 clearly shows a localized potential within ≈ 25 nm of the tip. With magnetic lengths at 1 T equal to 26 nm these results indicate that the local tip potential has a large effect on the measured LDoS and that the tip-potential effect cannot be ignored. Instead it must be quantified as done here, and incorporated into our understanding of the measured spectra.

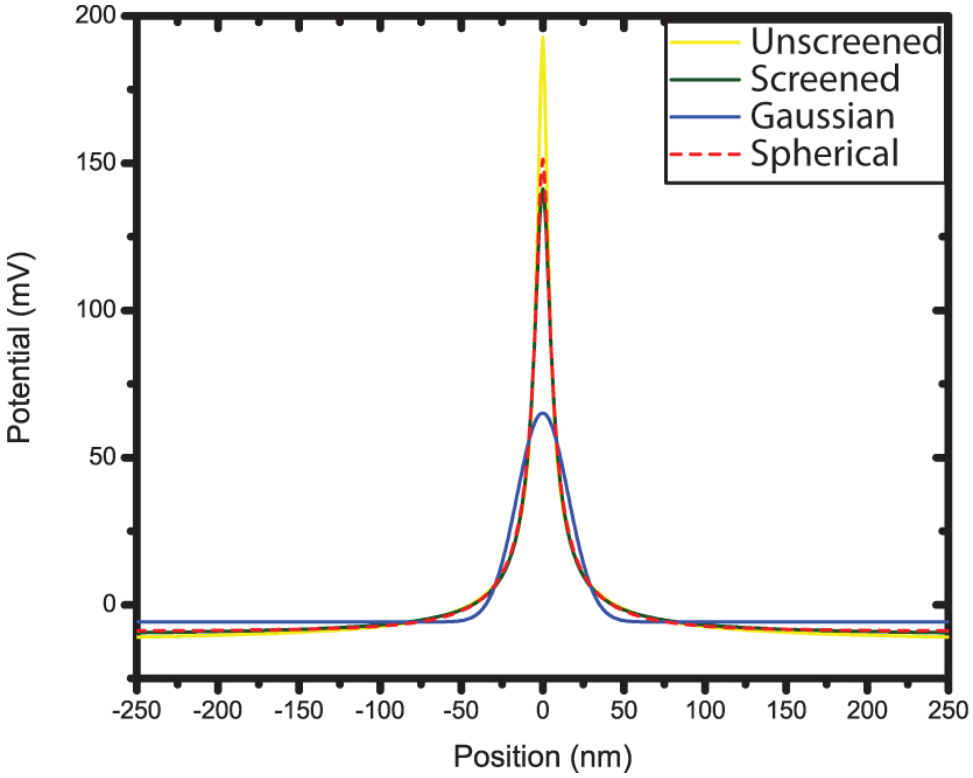

Figure 3.12: A compilation of fit potentials of tip 2 using all four fit methods.

Table 3.6 shows the averaged lever arm, Dirac point and Fermi velocity obtained by fitting each tip with the 4 models. These three values indicate the capacitive coupling of the tip changed slightly as the tip changed shape.

Table 3.6: Averaged results from all 4 tip models.

Tip	E_d (meV)	ξ	$c^*\left(10^6\ \mathrm{m/s}\right)$
1	-56.8	12.9	1.02
2	-9.4	10.6	1.03
3	-8.7	9.4	1.02

Without a thorough understanding of the tip effects Fermi velocities cannot be accurately determined. Indeed the c^* values in table 3.6 are smaller than those previously reported.[74] Other results attributed to fundamental properties of graphene or its coupling to the substrate, such as asymmetries between hole and electron carrier velocities,[101] may also be caused by the tip potential. The influence of the lever arm and the tip-induced surface potential on the interpretation of LL spectra is shown in figure 3.13. A black line in figure 3.13 A has been fit to the peak positions of tip 2 plotted on a $\sqrt{NB}$ scale and results in a velocity of 1.14 x 10^6 m/s when no tip effects are incorporated. By excluding LL_0 and fitting only holes or electron states, velocities were found to be (1.34 ± 0.03) x 10^6 m/s for electron states and (1.12 ± 0.03) x 10^6 m/s for hole states. These results are similar to previously reported observations[101] that link Fermi velocity asymmetries with a weak coupling between graphene and a graphite substrate. In chapter 5 the author will show that the tip effect plus defect effects can directly affect observed velocity asymmetries.

It can be seen in figure 3.13 B, that the slope will reduce (red dashed line) when the lever arm effect is removed. The resulting slope gives a Fermi velocity of 1.02 x 10^6 m/s. Once the localized potential effect is removed all LL peaks are then seen to collapse onto the light blue line in figure 3.13 C. The velocity changed to 1.03 x 10^6 m/s, but in addition there no longer remains any asymmetry in the system. These results are extremely encouraging, explaining all peaks measured in the spectra. Perhaps most

importantly the large non-linear energy shift of LL_0 with the magnet field is explained and accurately modeled.

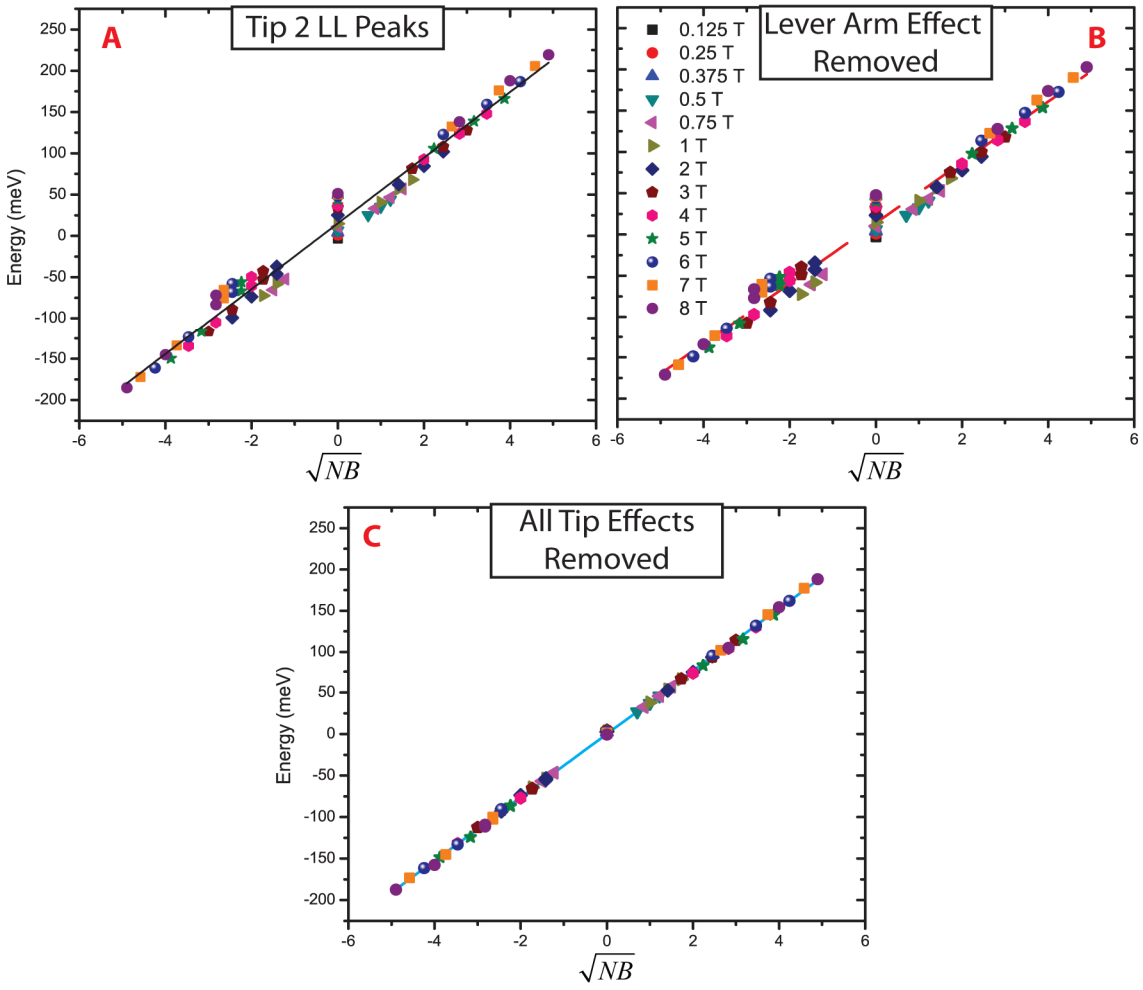

Figure 3.13: Removing the tip effects. The LL positions of tip 2 (A) are shown to contain large deviations from ideal graphene's $\sqrt{NB}$ dependence. By removing the lever arm effect (B) the slope is seen to reduce from the original (black) fit line to red dashed line. Once the perturbation of the tip potential is removed (C) all LLs collapse onto the ideal graphene equation (blue line), with a Fermi velocity of 1.03 x 10^6 m/s.

Energy vs. magnetic field plots are shown in figure 3.14 to emphasize the total effect of the tip. Here ideal graphene with a Dirac point at -35 meV has been overlaid by the tip-perturbed spectrum corresponding to tip 2. The three lowest-indexed $|n,m\rangle$ states are shown for LL_{-3} to LL_3. While the potential was treated as a perturbation, it can be seen that its presence has a large effect on the low-index LLs. Here LL_{-2} is seen to

correspond to energies where the ideal LL_{-1} is expected while LL_1 overlaps the ideal graphene LL_2 location.

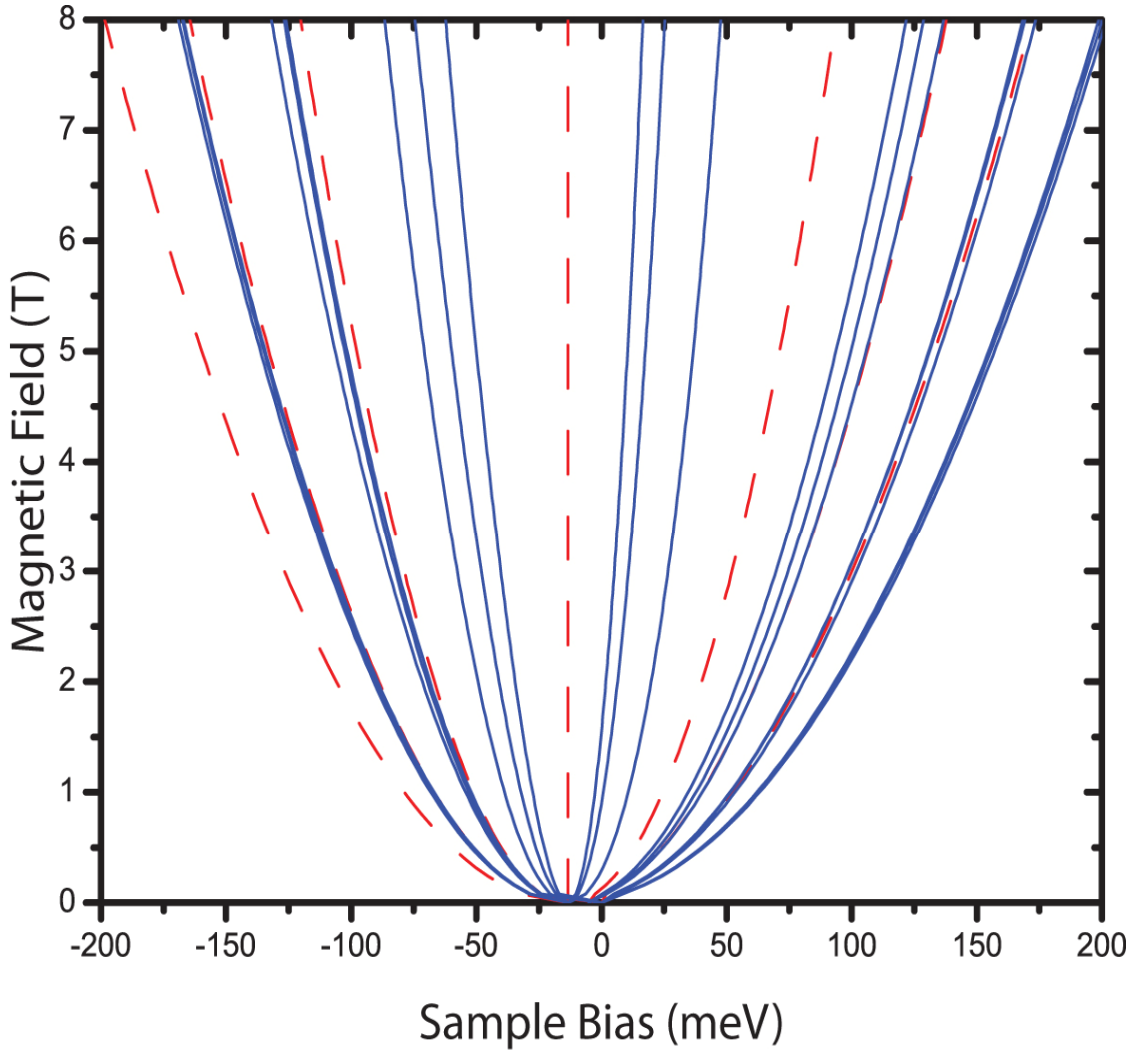

Figure 3.14: A comparison to ideal graphene (red) with a Dirac point at -35 meV and the tip influenced graphene fit for tip 2 (blue).

In the model, the total potential can be changed instead of the magnetic field. This allows for the influence of the tip effects to be seen on the individual $|n,m\rangle$ states out to $|m| \leq 5$ (figure 3.15). Here Q_0 is the measured potential for tip 1. In chapter 5, defects will be shown to change the total potential, with results related to those shown in figure 3.15. Only by understanding the effect of the tip on graphene can the further effect

of defects be understood. Clearly, all STM measurements on low-density materials must convincingly model the tip effects before invoking other explanations to explain observed anomalies.

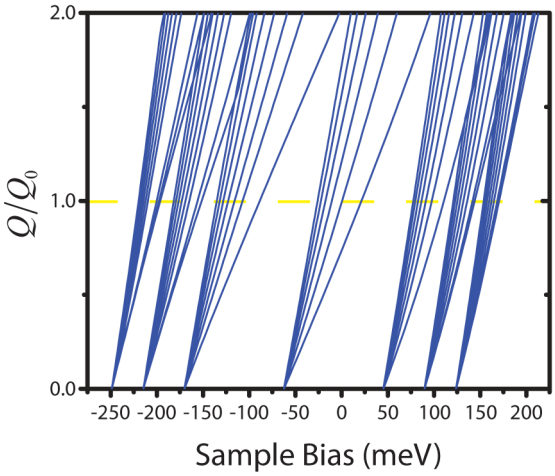

Figure 3.15: Potential effect due to the work function difference on LLs at 8 T. The direct effect of the potential on LL energies is shown. In particular the charge, Q, is varied using the unscreened point model to show the large effect on low-index $|n,m\rangle$ states. Small glitches due to the energy selection process can be seen when LL_N states cross nearest neighbor $LL_{N\pm1}$ states.

CHAPTER 4

TUNNELING MAGNETO CONDUCTANCE OSCILLATIONS

A new technique was developed to characterize graphene's energy-momentum relation using STM. It permits for the measurement of the differential tunnel conductance as a function of magnetic field by ramping the field while tunneling at a constant bias. Compared to photoemission measurements,[62] this technique results in nearly an order of magnitude more precise measurement in momentum space. In addition, this technique is an atomic measurement and is limited in sampling the momentum space by the magnetic length. Other observations not well understood were noticed using this technique and while very interesting these will be summarized in sections 4.6 and in appendix A.

4.1 Measurement Technique

STS magnetic field studies are done invariably at constant magnetic fields where $\frac{dI}{dV}(E,x,y,B)$ measurements can be performed by sweeping the sample bias. Changing B would require retracting the tip, changing the magnetic field and reapproaching. For this thesis a new technique was developed in which spectra were obtained by slowly ramping the magnetic field while tunneling at a constant bias and recording the differential tunnel conductance, $\frac{dI}{dV}$. The data acquired is similar to that from Shubnikov-de Haas measurements, yet it retains atomic scale spatial resolution. During the development of this technique multiple data acquisition settings were used. In particular, depending on the filling factor (set by the magnetic field) sensitivity settings on the lock-in amplifier were adjusted.

Few STM systems are stable enough to perform multi-hour conductance measurements, let alone while the magnetic field changes. Fortunately the extraordinary stability of the NIST LTSTM (chapter 2.3) made possible such an undertaking.

Implementation of this new technique was hampered somewhat by hardware limitations and by proprietary software (challenges that could have been addressed if instrument time wasn't so precious). Instead of measuring $\frac{dI}{dV}(B)$ directly, it was necessary to ramp B at a constant rate and measure $\frac{dI}{dV}(t)$. The hardware and software available could record a time-trace only on the analog-to-digital converter normally dedicated to Z height. Consequently, Z was not recorder during acquisition of $\frac{dI}{dV}(t)$. The acquisition sequence began by setting the magnetic field to its maximum value of 1.2 T or 2 T, after which a $\frac{dI}{dV}(E)$ spectrum was obtained. A small AC voltage was then applied to the tip while being placed into a constant current servo loop at the chosen sample bias. The magnetic field was changed at rates from 0.01 T/min to 0.06 T/min while dI/dV vs. time measurements were performed. Ideally data acquisition software would have recorded both dI/dV and magnetic field values, but due to the limitations described, conversion from time to field was performed. Field ramps took up to 4 hours for each set bias. Manual input was needed to start and stop these scans.

Since Z and $\frac{dI}{dV}$ could not be recorded simultaneously, $Z(B)$ was measured separately as shown in figure 4.1. While magnetic sweeps were eventually increased to 2 T, Z vs. B measurements were performed earlier in the data run from -1.2 T to 1.2 T only. Three features were seen when monitoring the Z height. One is that it follows a parabolic form $Z = 17.7 + 2.3B - 10.6B^2$. This is believed to be primarily due to magnetostriction of STM parts as the magnetic field changes. Typical fractional changes are on the order of 10^{-7} for materials such as stainless steel,[125] which would cause height changes of approximately 0.5 nm for a sample holder that is 5 mm thick. The second feature is the presence of small oscillation faintly visible within the background parabola. The period

of these oscillations is nearly linear in B after 0.4 T, and will be explored more in section 4.6. The final feature is a dip in Z position between -0.15 T and 0.15 T. This interesting feature will require further investigations to confirm its source, but one can speculate that it is due to weak localization or weak anti-localization.[126] The dip is found to have a slight hysteresis of 0.01 T when the sweep direction is changed (figure 4.1 B), which is probably just hysteresis of materials within the field volume. Due to time constraints and the infancy of this procedure an alternate sample such as gold could not be used to assist towards distinguishing these observed effects from either STM system responses or graphene effects.

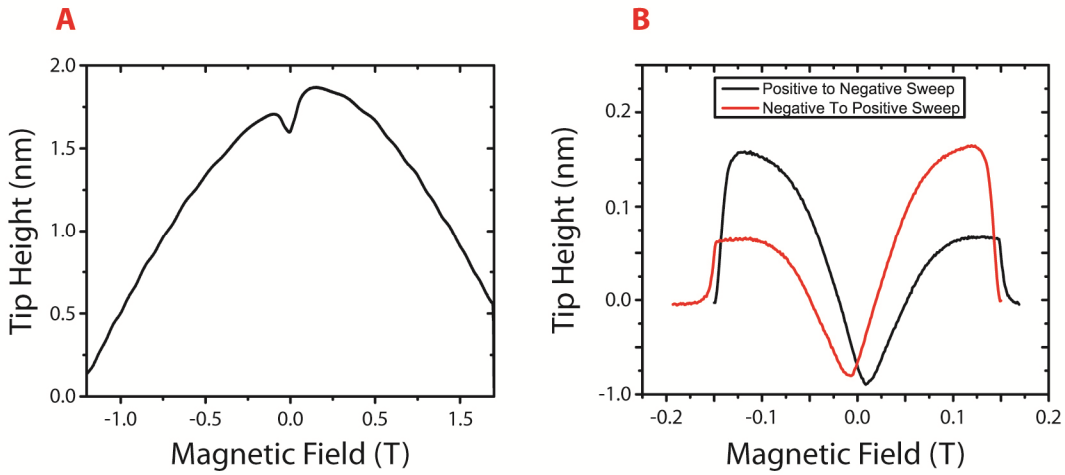

Figure 4.1: Z vs. B calibration measurements. (A) The tip height is seen to follow a parabolic dependence on the magnetic field. (B) Along with a 0.01 T hysteresis a local minimum is seen in the tip height. This is likely due to a sudden decrease in LDoS, possibly indicating weak anti-localization.[126] [A: (L_25754, $V_{set} = -80$ meV, $\Delta B = 0.02$ T/min, $I_{set} = 0.8$ nA); B: (L_25985 Red, $\Delta B = 0.06$ T/min, $V_{set} = -55$ meV, $I_{set} = 0.22$ nA) (Black 25984, $\Delta B = 0.06$ T/min, -55 mV, $I = 0.22$ nA)]

Quantification of the XY drift during field sweeps was performed by obtaining atomic resolution topographs near defects before and after, and by performing multiple magnetic field sweeps. Total displacement in the X direction was 2.3 Å after sweeping from -1.2 T to 1.2 T four times (2 forward sweeps and 2 reverse). The corresponding

displacement in the *Y* direction was observed to be -0.25 Å. A separate single sweep from 1.2 T to -1.2 T at 0.02 T/min resulted in a similar drift measurement of 0.5 Å in the *X* direction and 0.0 Å in the *Y* direction. This result indicates minimal magnetostriction effects on the graphene plane.

4.2 Initial Measurements

Measurements were performed in 7 locations over a period of 21 days. During this time four to seven different tip states are believed to have occurred, with all tip states resulting in spectra similar to tip 1 and tip 2 in chapter 3, but with E_d near 30 meV. A moiré pattern of 1.9 nm was present at each location indicating a rotation of 7.42 degrees between the top two layers of graphene. Initial investigations were performed within 200 nm of a boundary between different moiré patterns seen in figure 4.2. A second moiré pattern is observed on one side of the boundary due to rotation of the graphene layer two layers below the surface.[77, 127] The boundary is indicative of a grain boundary occurring in either the second or third layer, since the top layer appears to be defect-free (figure 4.2).

Calibrations were often performed throughout data acquisition in an attempt to improve measurements. The first magnetic field sweep performed was from 0 T to 0.2 T with a sensitivity setting of 10 mV, a time constant of 100 ms and a 0.5 mV modulation voltage. To say the resulting measurement of only noise was underwhelming would be an understatement. The first oscillations in the dI/dV referred to as "tunneling magneto conductance oscillations" (TMCO) were seen (figure 4.3). Initially a magnetic field ramp of 0.02 T/min was used to minimize drift and heating, but this was later increased to 0.04 T/min which resulted in only a 0.002 K increase in temp for sweeps up to 2 T.

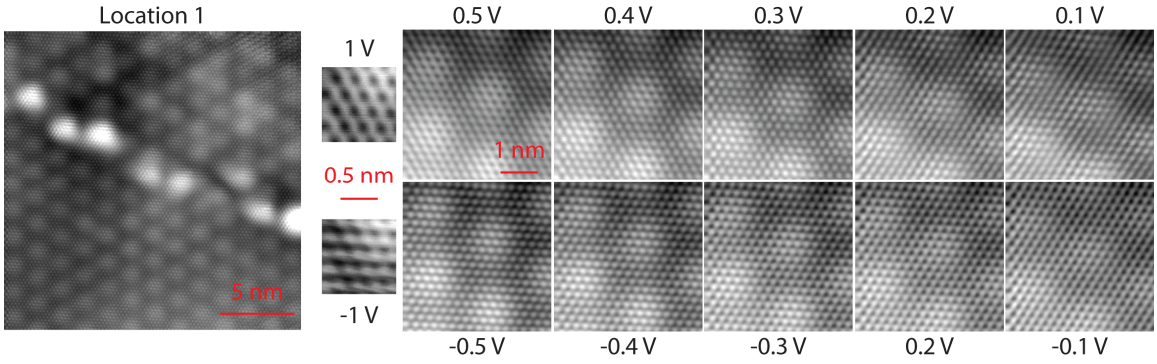

Figure 4.2: (Left) Initial dI/dV vs. B measurements were obtained on the single 1.9 nm moiré pattern, but a boundary between moiré patterns occurred within 200 nm of location 1. Bias dependence imaging at constant impedance can be seen to indicate asymmetric effects when sampling the graphene lattice, but no response is seen on the single moiré pattern. It is believed the boundary is due to the joining of two rotated graphene domains in the second or third layer, where the second moiré pattern is only observed in the upper half of the large topograph. [Location 1: (L_25667, 0.6 nm black/white scale, 200 nm x 200 nm, $V_{Bias} = 350$ meV, $I_{set} = 0.35$ nA); Bias dependence: (L_25696 and L_25691 1 nm x 1 nm, L_25676 to L_25685 5 nm x 5 nm, all $Z = 1.0$ GΩ, 0.1 Å/step, 0.1 nm black/white scale)]

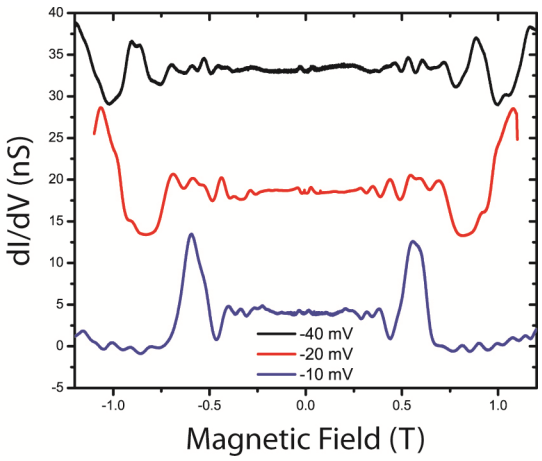

Figure 4.3: The first measurement of TMCO. Peaks caused by LLs crossing the tip bias as the magnetic field is swept are similar to Shubnikov de haas oscillations. Spectra have a 14 nS offset. [Black: (L_25739, -1.2 T to 1.2 T, $V_{set} = -40$ meV, $I_{set} = 0.4$ nA); Red: (L_25736, 1.1 T to -1.1 T, $V_{set} = -20$ meV, $I_{set} = 0.2$ nA, $V_{\mathrm{mod}} = 1.0$ mV); Blue: (L_25738, 1.22 T to -1.20 T, $V_{set} = -10$ meV, $I_{set} = 0.1$ nA , $V_{\mathrm{mod}} = 1.0$ mV)]

In an attempt to maintain similar parameters, spectra were initially obtained with the same impedance $\frac{V}{I} = \frac{10\text{ mV}}{0.1\text{ nA}} = 0.1\text{ G}\Omega$. Eventually impedance measurements were increased to minimize tip switches. Settings were not changed once the magnetic field sweep limit was switched to 2 T and shown to reproduce the 0 T to 1.2 T results. For magnetic sweeps from 0 to 2 T the ideal settings for maximum signal without saturation were found to be the following:

Table 4.1: Finalized settings used in tunneling magneto conductance spectroscopy measurements. The magnetic field range was from 0 T to 2 T.

Lock-in Amplifier Frequency (frequency used in dI/dV measurements)	465.7 Hz
Modulation Voltage, V_{mod} (amplitude of AC signal)	1 mV
Sensitivity (Sets amplification on dI/dV measurements)	0.05 mV
Time Constant, τ	0.1 sec
Time per data point	1.0 sec
Magnetic Field Ramp Rate, ΔB	0.04 T/min
Impedance, V_{Bias}/I_{tunnel}	0.25 GΩ

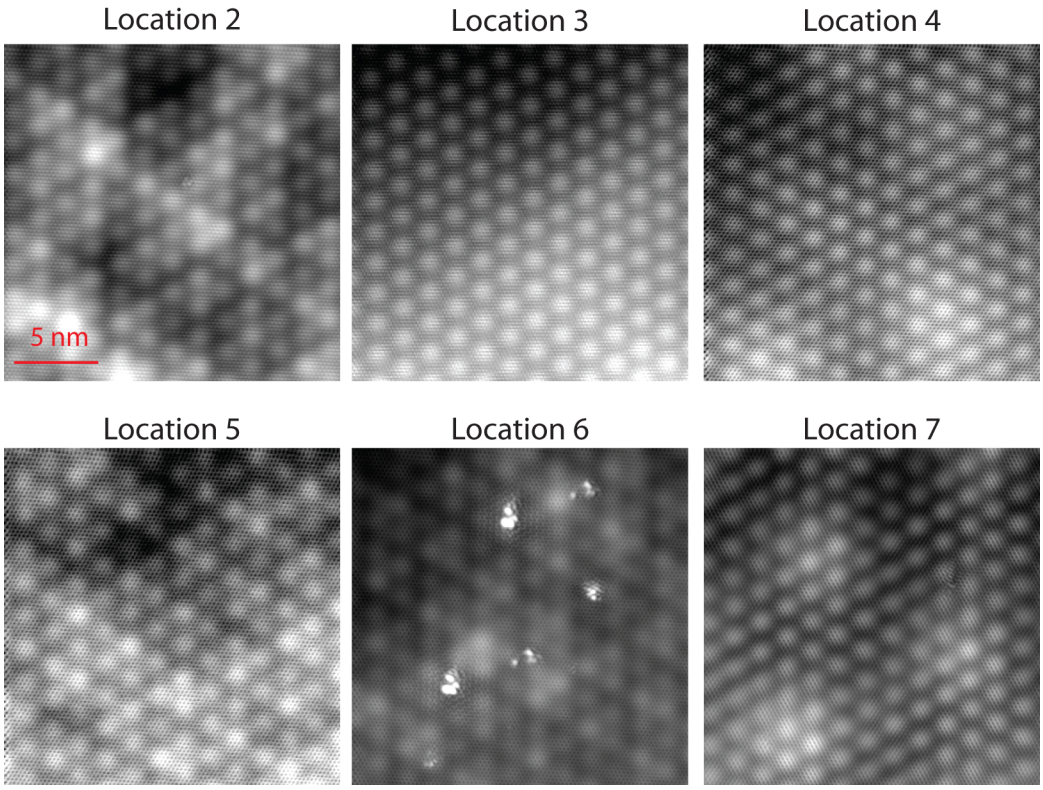

Figure 4.4: 20 nm x 20 nm topographs obtained where additional dI/dV vs. B measurements were performed. The 1.9 nm moiré pattern is present in all locations. In addition an 11.06 nm moiré pattern was observed at multiple locations with no quantifiable affect on measurements. The defect in location 2 was used to calibrate *X, Y* drift indicating < 0.1 nm/scan. Atomic imaging was obtained in all location, but in location 6 copies of defects were seen indicating a multi-tip. [Location 2: (L_ 25742, 401 points, $V_{Bias} = -350$ meV); Location 3: (L_25824, 201 points, $V_{bias} = 350$ meV); Location 4: (L_25878, 401 pts, $V_{Bias} = -100$ meV); Location 5: (L_25884, 401 pts, $V_{Bias} = -100$ meV); Location 6: (L_25890, 401 pts, $V_{Bias} = -350$ meV); Location 7: (L_25987, 2001 pts, $V_{Bias} = 350$ meV); All: $I_{set} = 0.1$ nA, black/white scale: 0.1 nm]

Locations away from defects and grain boundaries were sought once measurement parameters were shown to produce TMCO. Coarse tip movements $(> 0.5\,\mu m)$ were made to find locations 2-7 seen in figure 4.4. The atomic defect in location 2 was ideal for measuring the atomic drift rate of < 0.1 nm/hour. The majority of the 0 T to 2 T sweeps were performed in locations 3 and 4. Locations 5, 6 and 7 were used in an attempt to understand if defects and tip states had an impact on the linear-in-*B*

oscillations reported in section 4.6. Details of the moiré patterns were observed to have little effect on single location measurements done at single x, y locations.

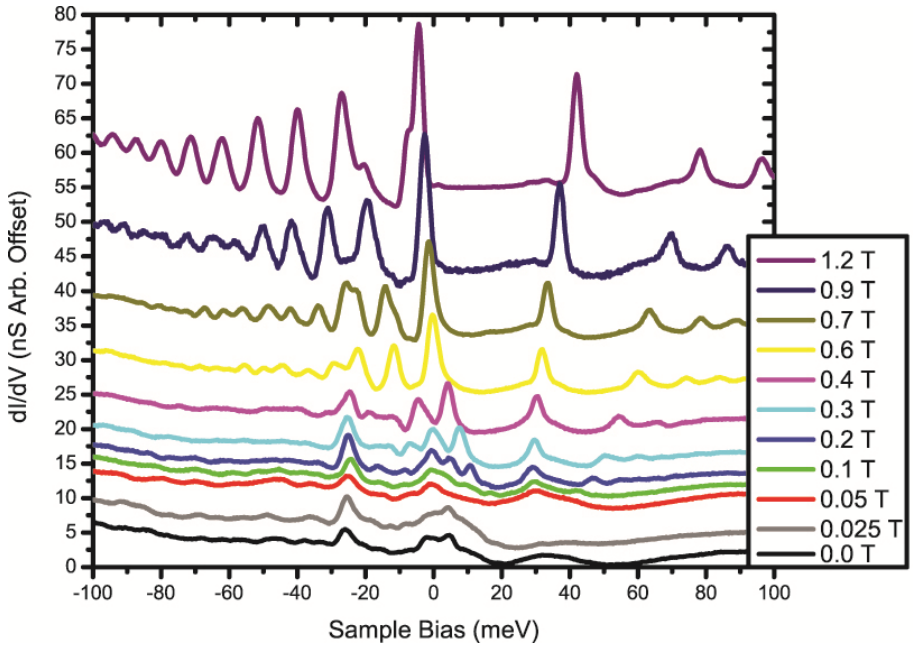

Figure 4.5: Selected constant field STS measurements performed in fields from 0 T to 1.2 T. Spectra are from the same tip state as all 0 T to 2 T scans. [Selected from L_25757-L_25777, $V_{set} = -100$ meV, $I_{set} = 0.4$ nA, 601 pts, $V_{mod} = 1.0$ mV]

Sample low field conductance spectra have been included in figure 4.5. Tip effects discussed in chapter 3 are expected to be the cause of the ~10 meV shift of LL_0 from 0.1 T to 1.2 T. Unfortunately field series were confined to ≤ 2.0 T, making a reliable fit for TIBB nearly impossible, but LL_0 was observed to shift by over 80 meV by 6 T indicating that TIBB remains a large contributor to low-index LL energies. These constant field STS measurements were primarily used to identify LL peak positions observed from TMCO measurements.

4.3 TMCO Results

Once fully calibrated, TMCO were observed as the magnetic field was changed. It should be stressed that the TMCO are local measurements, unlike Shubnikov de Haas oscillations (SdHO). In addition TMCO measurements are not limited to the Fermi

energy; rather the energy of interest is set by the tunneling bias, without the need of a back-gate (which is inherently difficult in multi layer epitaxial graphene).

Sample TMCO data is shown in figure 4.6. The largest peaks are due to LLs matching the tunneling bias, ie, $eV_{Bias} = E_N - E_f = \mathrm{sgn}(N)c^*\sqrt{2e\hbar B|N|} - E_f$ (neglecting the lever-arm effect). With this relation, a procedure analogous to that applied to SdHOs[4, 5] can be performed to convert the frequency of oscillations in $1/B$ to the cross-sectional area of a constant-energy contour in momentum space. For SdHOs, the magnetic frequency is given by $B_F = \left[\Delta\left(\frac{1}{B}\right)\right]^{-1} = \frac{\hbar}{2\pi e}A_F$ where A_F is the cross-sectional area of the Fermi surface in a plane normal to the magnetic field.[128-130] An identical result holds for TMCOs except that the cross-sectional area will depend on the *k*-space area, A_E, at $E = eV_{Bias}$ (figure 4.6 A) and not the at Fermi energy. Substituting the area, $A_E = \pi k_E^2$, for energies near the Dirac point, one arrives at the wave vector relationship:

$$k_E = \sqrt{\frac{4\pi e}{h}B_E}\,. \qquad 53$$

Thus, with the assumption of circular constant-energy surfaces, graphene's momentum wave vector (magnitude) can be determined at any energy (tunneling bias). Examples of three different tunneling biases are shown in figure 4.6 B. Once the corresponding LL indices are identified for each sampled energy, they can be plotted in relation to the inverse magnetic field (figure 4.6 C). The slope, B_E, is then extracted using least-square fitting.

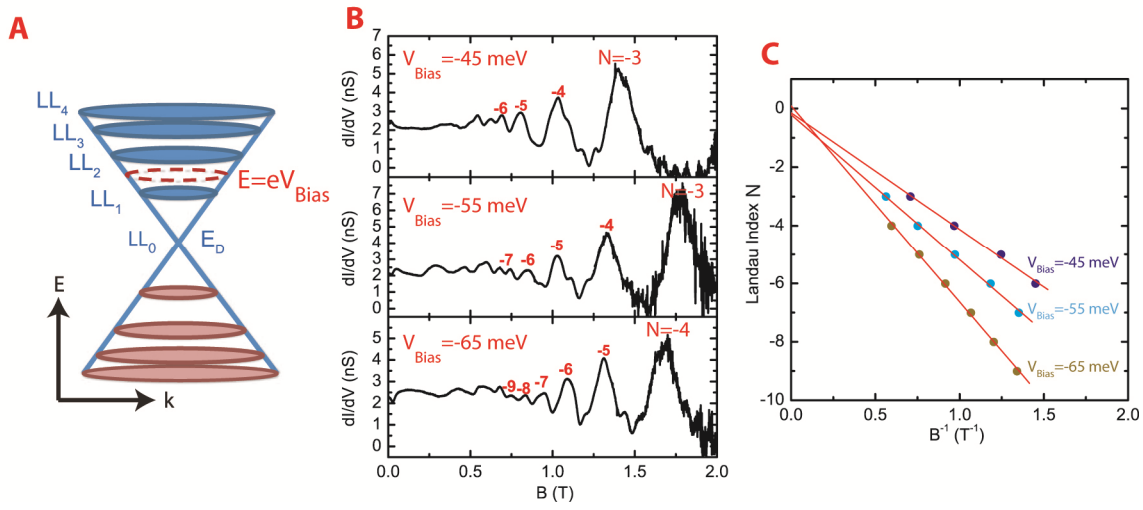

Figure 4.6: (A) Under the influence of perpendicular magnetic field, graphene's energy spectrum condenses into discrete rings in momentum space. Changing the magnetic field forces LLs (rings) through the cross sectional area (red dashed ring) set by the tunneling bias eV_{Bias}. This creates a peak in dI/dV. (B) Three TMCO spectra obtained at different sample biases using measurement settings in table 4.1. For fields above 0.5 T, LL's can be indexed with the assistance of figure 4.5. (C) Landau index N plotted vs. B^{-1}. The slope of energies -45 meV, -55 meV and -65 meV gives B_E equal to -3.2 T^{-1}, -5.3 T^{-1} and -6.8 T^{-1} respectively, from which k_E can be determined (equation 53). [(L_25839, 0 T to 2 T, $V_{Bias} = -45$ meV), (L_25836, 2 T to 0 T, $V_{Bias} = -55$ meV), and (L_25837 0 T to 2 T, $V_{Bias} = -65$ meV)]

B_E can be extracted for multiple tip biases, resulting in the "fan plot" in figure 4.7 A. The intercept of zero is indicative of a graphene Berry phase of π,[74] providing further evidence of multilayer epitaxial graphene's massless Dirac fermion behavior. Figure 4.7 B shows the energy dispersion, extracted from TMCO spectra within ± 125 meV of the Dirac point. A linear fit to the energy distribution yields an "extracted" carrier velocity of $c' = (1.07 \pm 0.006) \times 10^6$ m/s for both electrons and holes. The resulting Dirac point was found to be at $E_0 = 29.7 \pm 0.5$ meV, which agrees with $E_0 = 29.6 \pm 1.0$ meV in dI/dV spectrum obtained at 0.1 T (figure 4.5). All uncertainties represent one standard deviation in the measured quantity. This technique allowed the author to measure the

low-energy dispersion of graphene with an energy resolution of 2.8 meV in both the empty and filled states,[74] unlike photo-electron microscopy.[62]

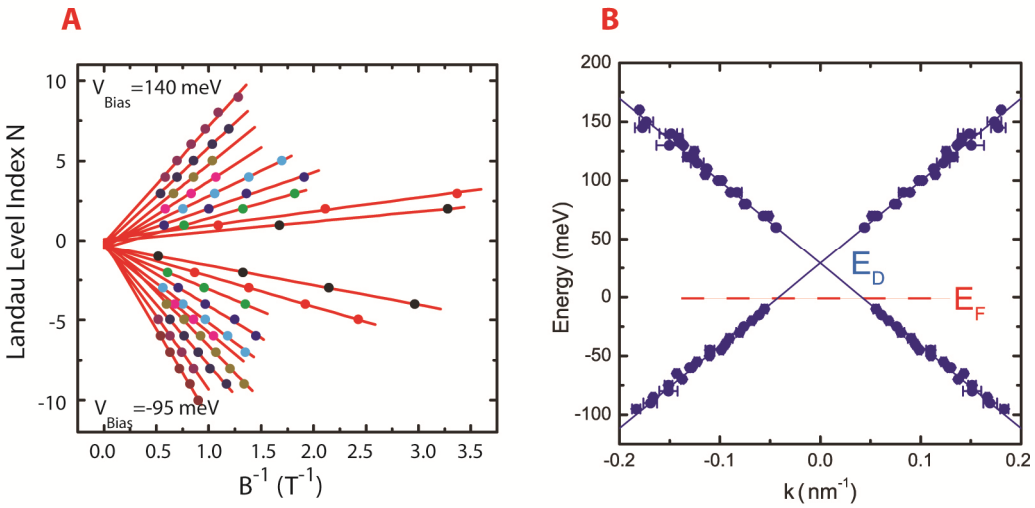

Figure 4.7: (A) A fan plot (LL index vs. B^{-1}) corresponding to all recorded 0-2 T TMCO spectra. The intercept of zero indicates the presence of massless fermions as expected for graphene. (B) $E(k_E)$ determined from B_E values, equation 53, and $E - E_f = eV_{Bias}$. A precise local energy vs. momentum measurement is obtained for energies near the Dirac point.

4.4 Limitations

While the TMCO technique enables for precise energy vs. momentum measurements, the implementations described does have some limitations. First, tip effects have not been considered in the preceding discussion. It was initially believed that because measurements were performed at smaller magnetic fields and lower sample bias, tip effects would be minimized. More careful consideration (chapter 3) shows that that tip effects follow equation 48. The following relationship can then be extracted for the momentum magnitude:

$$k_{meas} = \sqrt{\frac{4\pi e}{h}\left(\frac{\left(1 - 1/\xi\right)E_{meas} - \lambda_{n,m}}{c^* \sqrt{2e\hbar}}\right)^2} \quad . \qquad 54$$

LLs of index $N < 2$ were rarely measured at sample biases where $\left|E_d - eV_{Bias}\right| > 25$ meV, minimizing the perturbation due to the tip potential well and causing $\lambda_{n,m} \sim 0$. The extracted velocity, c', found by assuming the measured energy $E_{meas} = \hbar c^* k_E$, is incorrect; from the measurement one obtains $E_{meas} = \hbar c' k_{meas}$. The ideal measurement is only obtained when $\xi \to \infty$. Equating these two relations for $\lambda_{n,m} = 0$ equations we find the corrected carrier velocity:

$$c^* = c' \frac{k_{meas}}{k_E} = c'\left(1 - 1/\xi\right). \qquad 55$$

Unfortunately large field series (cf. chapter 3) were not performed concurrently with TMCO data, hence the author can only speculate on the exact value of ξ. From conductance line scans performed at location 4, a lever arm of $\xi = 9.7$ was measured, but the tip changed slightly between TMCO measurements and the conductance line scan. However, using this value the corrected velocity would be $c^* = 0.96 \times 10^6\ m/s$, slightly lower than the corrected values of c^* obtained in chapter 3.

A second limitation in the TMCO method is the difficulty to distinguish LL from "background variations" in fields lower than 0.5 T. The physics of these variations is a topic worthy of investigations (see appendix A) but they limit the determination of k_E close to the Dirac point. The gap within 25 meV of the Dirac point (figure 4.8) is due to the fact that only $LL_{\pm 1}$ could be identified in this magnetic field range because higher LLs with $|N| > 1$ crossed A_E at fields lower than 0.5 T. It is likely that this limitation can be reduced, since LLs are evident in $\frac{dI}{dV}(E)$ measurements at fields as low as 0.1 T. A reduction might be accomplished by performing smaller magnetic field sweeps with higher sensitivity settings, but due to limited instrument time, this was not verified.

The final major constraint is due to system limitations. While incredibly stable, system 2 was designed such that isolation air bellows must be emptied or filled to re-level the STM as the magnetic field is changed. Because TMCO measurements are performed while the tip is tunneling, the air bellows cannot be re-leveled during the measurement. As a result, magnetic fields could only be safely ramped to 2 T and a noticeable increase in noise became apparent around 1.5 T due to small mechanical contact between the dewar and the STM cryostat. This design limitation has been addressed in the newest ultra low temperature STM system at NIST. [87] Finally, revisions to the data acquisition software and hardware could be made to allow high density E vs. B maps be performed (up to 15 T) without the need of constant supervision.

4.5 Benefits

The TMCO results in figure 4.7 B show the expected symmetry between hole and electron states, unlike the constant-*B* conductance measurements, which heavily weight the low index LLs. As a direct result, tip effects impact traditional LL $\frac{dI}{dV}(E)$ measurements more than TMCO measurements. In addition, TMCO measurements have been shown to result in a highly-accurate determination of graphene's energy-momentum dispersion, being limited thermally and instrumentally to 2.8 meV at 4.3 K (this could be reduced with smaller modulation voltage), and a wave vector resolution $\leq 0.02\ \mathrm{nm}^{-1}$.[74] This resolution is nearly one order of magnitude more precise then traditional low temperature photoelectron measurements,[62, 131, 132] and TMCO measurements probe both the unfilled and filled electron states.

4.6 Oscillations Periodic in B

As briefly mentioned in section 4.1, by subtracting the polynomial background from *Z* vs. *B* measurements an oscillation periodic in *B* was observed. These oscillations were also seen in all TMCO measurements. They are nearly an order of magnitude smaller than LL

TMCO at magnetic fields higher than 1.5 T (figure 4.6), but below 0.5 T they are nearly indistinguishable from LLs. Interestingly, no linearly separated peaks were present in dI/dV vs. sample bias measurements (figure 4.5) when the magnetic field was held constant. This indicates these oscillations are not due to tip induced quantum dot states directly below the tip,[109] and instead indicates that these oscillations are due to the changing magnetic field or are caused by tip states where $\left|\Psi_{tip}(0)\right|^2 = 0$.

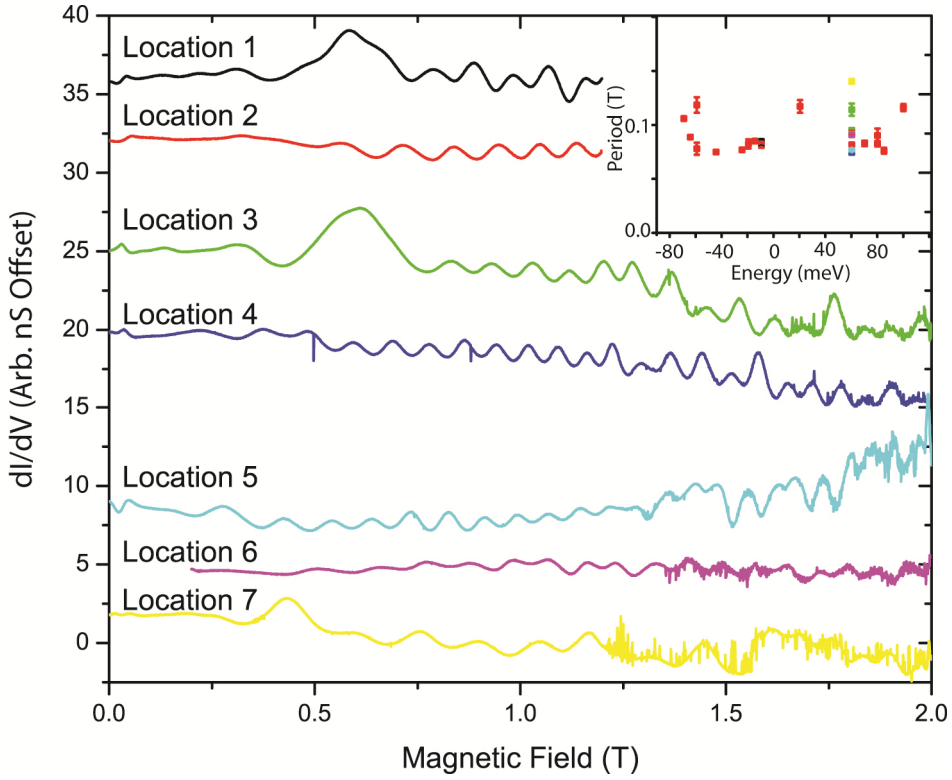

Figure 4.8: Oscillations periodic in *B*, seen in TMCO data. Selected spectra performed at 60 meV in different locations show the oscillations visible in fields above ~ 0.3 T. The large peak seen near 0.6 T is due to LL_1. (Inset) Periods obtained at each location (color correspond to spectra) vary slightly, but sample bias, and changes in microtips resulted in similar variations. [All parameters set by table 4.1 unless indicated; Location 1: (L_25794, 0 T to 1.2 T, 0.2 T/min); Location 2: (L_25827, 0 T to 1.2 T); Location 3: (L_25859, 0 T to 2.0 T); Location 4: (L_25881, -0.4 T to 2.0 T); Location 5: (L_25887, 2.0 T to -0.2 T); Location 6: (L_25891, 0.2 T to 2.0 T); Location 7: (L_25902, 2 T to -0.2 T)]

In order to better categorize these measurements multiple spectra were measured in each location at 60 mV (figure 4.8). This bias was selected such that no LLs were

present between 0.75 T and 2.0 T. In each location, a period of 0.09 ± 0.02 T was observed at all sampled energies. (Uncertainty represents one standard deviation in the measured quantity.) A slight range of periods was seen at different sample bias, but when probing different physical locations with different moiré patterns or additional defects, a nearly identical spread of data was seen (figure 4.8 inset). This variation was found to have little dependence on any of these two parameters, which could be due to under sampling these dependencies, or more likely the tip state. In addition, oscillations for $|B| > 0.5\,T$ nearly identical in frequency to the TMCO (figure 4.9) are seen after the parabolic background from *Z* vs. *B* is removed. This periodic-in-*B* oscillation did not vary as the magnetic field ramping rate was changed from 0.01 to 0.06 T/min. In addition the oscillation period was seen to shift slightly when changing sweep direction, only matching near the end (L_25827) and the beginning of each sweep (L_25828) seen in figure 4.9.

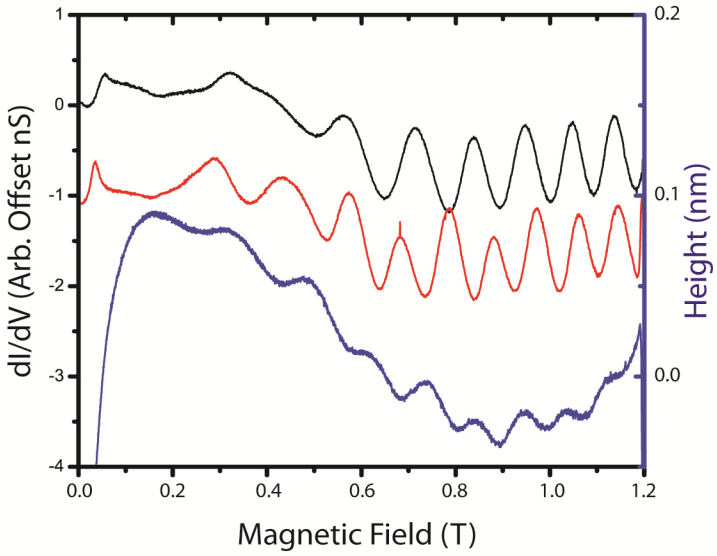

Figure 4.9: TMCO sweeps (Black and Red) performed at 60 meV. Background-subtracted *Z* vs. B spectrum (Blue) show similar oscillations. [Black: (L_25827, 0 T to 1.2 T); Red: (L_25828, 1.2 T to 0 T)]

The periodic in *B* oscillations are not due to induced currents since the frequency has no noticeable dependence on sweep rate. The reproducibility in different locations

indicates that universal conductance fluctuations also are not a likely explanation. Instead, it appears likely that these are Aharonov-Bohm oscillations.[133-135] Fermions are believed to flow in cyclotron orbits around closed circular equipotentials created by the tip's potential. If a loop is created interference will occur between fermions with a phase factor due to the magnetic flux $\Phi = B\mathrm{A}$, where B is the magnetic field and A is the area inside any loop created by the fermion. The oscillations are caused by the phase difference between orbiting fermions, $\Delta\varphi = 2\pi\frac{\Phi}{\Phi_0}$, where $\Phi_0 = h/2e$ is the magnetic flux quantum.[136] In this case the oscillations complete a period in 0.09 ± 0.02 T indicating $\Phi/\Phi_0 = 1 \rightarrow (0.09 \pm 0.02\ \mathrm{T}) \times \mathrm{A} = \Phi_0$, and assuming a circular path results in a radius of 85 ± 10 nm. This number is slightly higher than the widths of potential wells found in chapter 3, where a radius of 85 nm would have a shift of ~ 5 meV from E_d. Interestingly, once magnetic fields are ≤ 0.3 T these oscillations disappear in figure 3.8. This could indicate that circular motion does not occur when magnetic lengths are on the order of 50 nm or larger. This length scale is similar to the well widths observed in chapter 3, and could indicate that circular motion likely does not occur when the magnetic length is larger than the well. The larger radius of 85 nm could indicate that there are states outside the well that fermions are able to orbit in when the magnetic length is of the same order or smaller than the well width. This effect would not be noticeable as linear peaks in traditional conductance measurements at constant fields. Instead it is expected that it would lower or raise total conductance which in this case would only be correctly sampled by performing over 10 different constant magnetic field STS measurements within 0.1 T.

4.7 TMCO Summary

TMCO were observed within 125 meV of the Dirac point. By using graphene's magnetic field and LL energy relation, measurements were converted to momentum space. This

new STM measurement technique resulted in the highest measured precision to date in energy and momentum space for graphene. Tip effects due to the lever arm were observed to influence these measurements, but the perturbation effect was minimized due to the emphasis on higher index LLs. In addition this measurement showed a linear oscillation not seen in constant field STS measurements, which possibly indicates an Aharonov-Bohm like effect due to TIBB. The ability to ramp the magnetic field while tunneling is still in its infancy stages, but it has been shown to measure the conductance magnetic field dependence in the atomic scale which is complimentary to constant magnetic field spectra.

CHAPTER 5

DEFECTS

The task of separating tip effects identified in chapter 3 from defect effects will be performed in this chapter. First a selection of high magnetic field conductance responses to different defects will be presented. These responses in dI/dV will be classified as potential effects on LLs or new defect states. Next an in depth analysis of a defect displaying nearly all of these traits will be performed, and using tip effect influences ,nearly all of the observed responses will be explained.

5.1 Tunnel Conductance Near Defects in High Magnetic Fields

Multiple defects due to atomic arrangements on the surface were studied. Most of these defects were identified from their influence in conductance measurements and then verified to exist via topographic data. This process inherently ignores defects which exhibit no modification to the LDoS. Figure 5.1 displays six representative defect responses.

The defect in figure 5.1 A shows the creation of "defect" states within 5 nm of the defect and the loss of LL states within 1 nm of the defect. This was the only defect observed where LLs and defect states were constant in energy, and no mixing was present between the LLs and the defect states. Shortly after studying this defect the sample was reheated and the tip was changed.

This new tip resulted in the measured defect responses seen in figure 5.1 B-F. In these spectra LLs are observed to bend in energy on the nm scale with LL or defect states modifications occurring up to 40 nm away from defects. The new tip created mirrored states for all defects, although spectra to ± 300 meV were needed for defect D6. The mirror states resulted in lever arm values ranging from 3.75 to 20. Each induced tip

change resulted in different lever arms, with the highest tip influence (lowest lever arm) occurring midway through data acquisition.

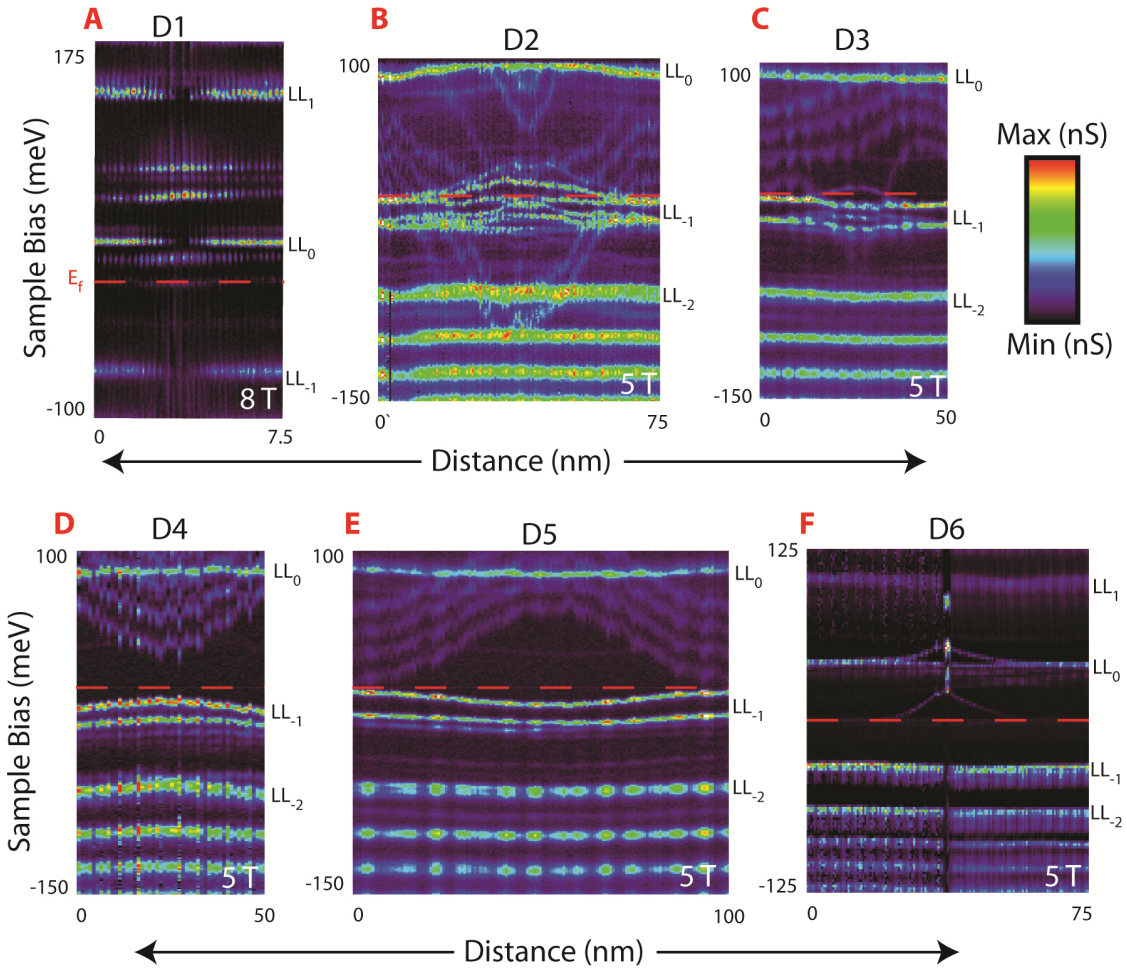

Figure 5.1: Six representative defect responses. (A, defect D1) This defect causes the loss of LL conductance intensity and creates new constant energy defect states within 5 nm of the defect. After the tip was replaced and the sample was reheated two peaks were observed to be present in LL_{-1}. (B, defect D2) Each peak undergoes a 4-fold splitting, indicating the presence of spin and valley degeneracy. (C, defect D3) One degenerate state can be seen to cross the Fermi energy, but the other three states remain under E_f and their splitting is only observed in mirror states. (D, defect D4) Defects bend LLs in energy, showing the presence of ≥ 5 $|n,m\rangle$ states. (E-D5) A defect moves states towards negative energies, while the splitting of LL_{-1} reduces by 5 meV. (F, defect D6) LLs disappear and defect states which bend in energy appear within a few nm of the defect. [A: (L_23656, Min = -0.05 nS, Max= 3.0 nS, 8 T); B: (L_26021 Min = -0.05 nS Max = 1.0 nS, 5 T) C: (L_26003 Min = -0.05 Max = 1.4, 5 T); D: (L26027 Min = -0.05 Max = 1.8, 5 T); E: (L_26003 Min = 0 Max = 1.2, 5 T); F: (L_25895 Min = -0.05 Max = 5.0, 5 T)]

Splitting of LL_{-1}'s $|n,m\rangle$ states can be seen near defects D2 and D3 (figure 5.1). The 4-fold degeneracy splitting of states $|1,0\rangle$ and $|1,-1\rangle$ can be seen directly in defect D2. Only one state crosses the Fermi energy in defect D3, while the other 3 states remain degenerate and are only observable in mirroring events. Defect D4 $|n,m\rangle$ states remain below E_f and do not split, but the additional states $|1,-2\rangle$, $|1,-3\rangle$, and $|1,-4\rangle$ can be measured in LL_{-1}. Other defects cause LLs to bend towards negative bias while the energy spacing between manifold states of LL_{-1} ($|1,0\rangle$ and $|1,-1\rangle$) decrease. In figure 5.1 this splitting is seen to reduce by 5 meV.

The final defect shown (D6, figure 5.1 F) contains two separate effects. Similarities are seen to defect D1 with LLs vanishing within 1.3 nm of the defect while new defect states appear. But, responses similar to defect D3 are also present, where LL_0 (instead of LL_{-1}) bends in energy. In addition, a second bending state believed to not be a LL is present at E_f. This bending in energy is believed to be due to a tip influence and will be explained in section 5.2.5.

Bound defects states have been extensively studied in systems with bandgaps.[109, 113, 137] Defects such as D1 and D6 exhibited bias dependent ionization regions (figure 5.2) indicating that magnetically localized states are ionized at higher sample bias. The length of this ionized regions indicated a tip effective radius of only 2 nm. At this length scale the TIBB potential with the lever arm effect included is expected to be ~200 meV. Only half of graphene's atoms were imaged for most of the voltages probed. This could be due to the defect or the tip state, but at 0.5 *V* and 0.4 *V* a small patch of graphene's honeycomb lattice can be seen when the tip has ionized the defect state.

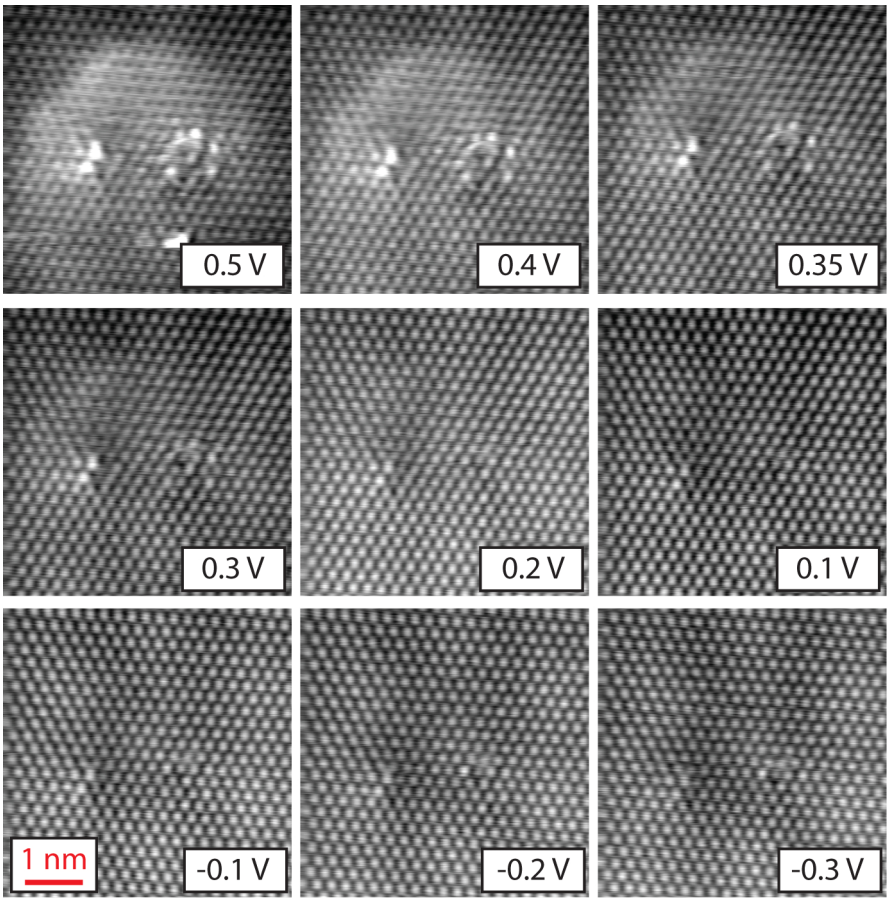

Figure 5.2: Potential dependence on topographs obtained at defect D6. For $V_{Bias} \geq 300$ meV regions appear higher within 2 nm of the defect due to an ionization event, where the tip effect pulls a defect state above the Fermi energy. [(L_ 26005 to L_26013 $V/I = 1.0$ GΩ, 5 nm x 5 nm, 0.1 Å/step, 5 T, black to white = 0.4 Å)]

5.2 In Depth Focus

Multiple conductance maps were performed in fields from 1/8 to 8 T around a single defect to understand the cause of these defects states and why LLs are observed to bend to them. This defect was located on a 4 nm moiré region (figure 5.3 A). Atomic imaging (figure 5.3 B) shows a 6-fold symmetry in the topograph, but graphene's atomic lattice is not easily identified due to the restructuring of graphene's orbitals. Unfortunately this defect cannot be identified as any particular lattice arrangement, but the graphene lattice can be overlaid on the topograph which indicates that this defect is not a screw dislocation or other type of defect which contorts the graphene layer.

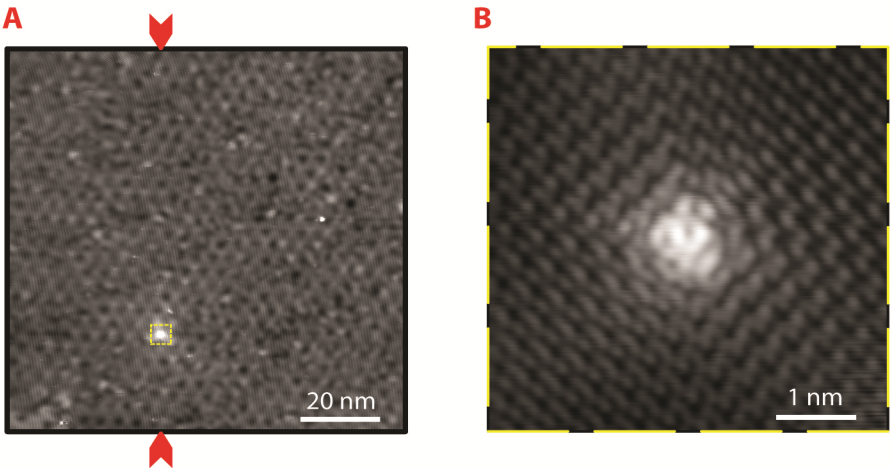

Figure 5.3: (A) A 100 nm x 100 nm topograph of the location multiple conductance maps were performed. One defect is easily identified on this image, but five were observed to be in the vicinity once conductance maps are studied. Line scans in figures 5.4 and 5.5 are extracted from the axis defined by the red arrows. (B) A 5 nm x 5 nm image of the large defect. A reconstruction of graphene's LDOS occurs making it nearly impossible to identify the atomic structure at the defect. [A: (L_25065, black to white 0.15 Å, $V_{Bias} = 350$ meV, $I_{set} = 0.4$ nA); B: (L_24877, black to white = 2.8 Å, $V_{Bias} = 350$ meV, $I_{set} = 0.4\,\text{nA}$)]

Data collection was performed at multiple magnetic fields for over a month and resulted in an immense amount of data from which only selected effects can be presented. Results such as the observation of LL_0's dependence on small angle moiré patterns[76, 77] have been reported on in depth and will be ignored.

5.2.1 Conductance Line Scans

An extracted line scan obtained at 1/8 T between the red arrows in figure 5.3 A is shown in figure 5.4 A. The location of the identified defect is marked with green arrows. Spectra are seen to have a large asymmetry between hole and electron states away from any defect (red arrow). Spectra are shown in figure 5.4 B corresponding to each location to provide better characterization. The current belief is that the potential gradient due to the tip effect is causing the asymmetric spectra away from any defect. From chapter 3 tip 2 is known to have a tip effect which dopes the area ~150 meV, while a lever arm of 10

was measured near the large defect. This will cause a p-n junction to occur from the graphene below the tip to the bulk graphene. From literature it is known that contacts cause asymmetries in conductance measurements between electron and hole states,[138] and it has been predicted that this is due to an asymmetry for repulsive vs. attractive scattering for massless Dirac quasiparticles.[139] It is the belief of the author that this asymmetric scattering effect is the cause of the conductance asymmetry. Ideally multiple tips with different work functions would be used to verify this effect, much like studies on the role of contacts that have already been performed.[140] Due to time constraints this could not be preformed and instead defects were used to change the amount of doping directly below the tip. At the blue arrow in figure 5.4 A the asymmetry reduces and makes spectra appear similar to ideal graphene. Here the belief is that the local potential of the defect cancels much of the tip's doping effect, effectively reducing the p-n junction.

This TIBB effect plus the defect potential picture works well in explaining the spectra until the tip is within 4 nm of the defect seen in the topograph (green arrow). If the only effect occurring was a larger local potential, then the larger p-n junction should continue to produce a larger asymmetry between the filled and empty states. Instead, a defect peak forms. This type of defect state has been predicted for multiple types of defects, but most predictions expect these defect states to occur within the first nearest neighbor of the defect.[141] Some of the longer range effects might be due to the existence of multiple defects within 2 nm of each other, but even predictions on nearest neighbor double vacancy expect the longest range effects to occur within a few nearest neighbors.[142]

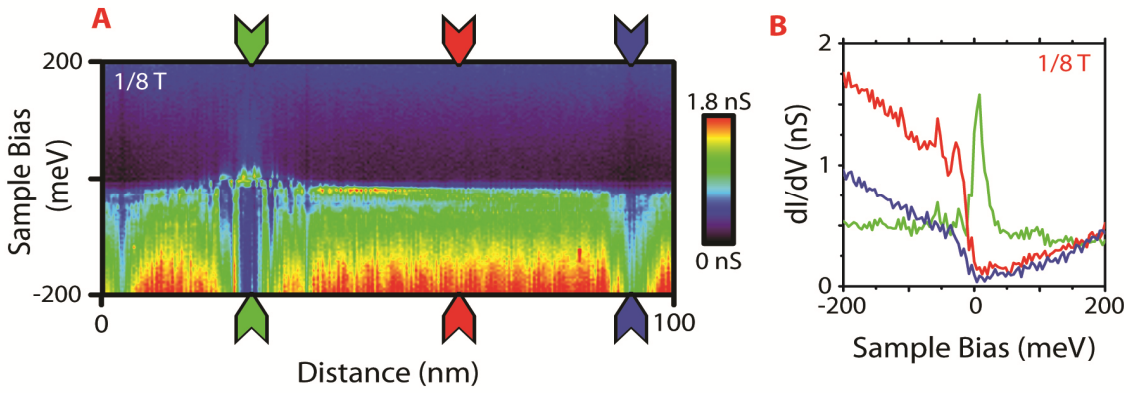

Figure 5.4: (A) An extracted conductance line scan performed at 1/8 T (L_25067) corresponding spatially to the arrows in figure 5.3 A. Three different responses are seen. Near the defect in the topograph (green arrow) spectra contain a large defect peak which crosses the Fermi energy. Away from defects (red arrow) spectra have a step like form, and near a second defect (blue arrow) electron-hole asymmetry reduces making spectra similar to ideal graphene. (B) Extracted spectra at each arrow are shown, retaining color correlation.

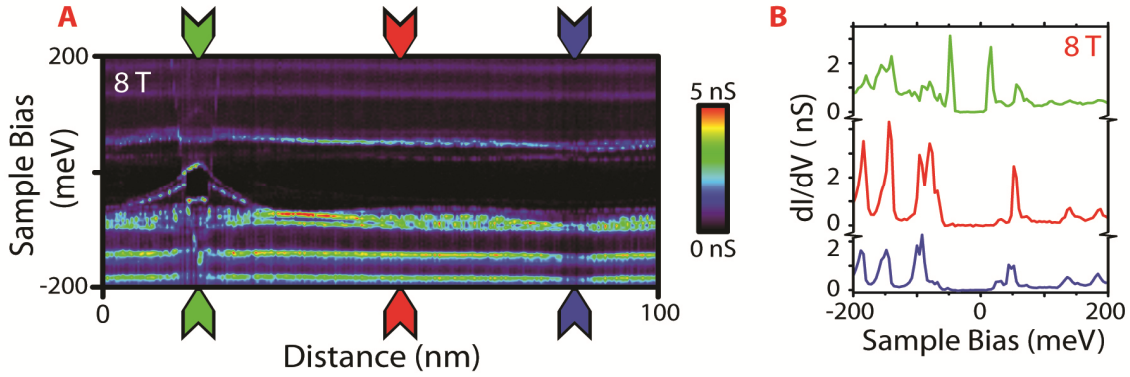

Figure 5.5: (A) An extracted conductance line scan performed at 8 T (L_25084) along the axis of the arrows in figure 5.3 A. Three different areas affect LLs. Near the defect in the topograph (green arrow) spectra contain additional defect peaks originating from LL_{-1}. Away from defects (red arrow) LLs have the same shape as tip 2 in chapter 3 and near the second defect (blue arrow) LL asymmetries in energy and conductance reduce. (B) Extracted spectra at each arrow are shown, retaining color correlation.

This picture of the defect potential effect adding with the tip's induced potential also matches with line scans extracted at 8 T (figure 5.5 A). Spectra away from defects are similar (red line figure 5.5 B) to those of the tip 2 in chapter 3. Spectra above the blue arrow (blue line figure 5.5 B) shifts LL_0 8 meV towards E_f while the splitting in LL_{-1}

nearly disappears, resulting is spectra close to ideal graphene. This confirms that the tip's potential effect on LLs can be reduced by potential variations near defects, but the large 80 meV shift of a the state originating from LL_{-1} near the green arrow indicates more is occurring than just this total potential dependence of LLs.

5.2.2 Local Potential Extraction

Three separate methods were used in an attempt to extract the local electron potential to see if the TIBB plus defect potential theory is accurate. The first method was originally designed to extract local potentials from silicon doped GaAs.[143] There tip effects were seen to ionize electrons, causing a spike in the current at higher sample bias. These ionized spectra were then used to extract the local potential near the defect. With graphene the TIBB and defects have a slightly different effect, yet can be treated nearly the same. The principle can be seen in figure 5.6 A. When tunneling into graphene with only the TIBB effect a bias V_1 is needed to produce a tunneling current I. Defects are believed to further manipulate the LDoS, with bound negative charges shifting the Dirac point towards positive energies, and vice versa for bound positive charges. This defect effect adds/subtracts to the TIBB (figure 5.6 A) making graphene easier/harder to tunnel into. In the case shown in figure 5.6 A to obtain the same current, I, a smaller bias, V_2, is needed. Using this principle, current spectra obtained near defects are shifted in voltage until they overlap a reference spectrum selected from the defect free regions. The total shift results in the potential change between V_1 and V_2. When the LDoS is not severely altered this value can be assumed to be the potential difference between the two locations. The hole state conductance intensity has been shown to depend on the p-n junction, so only positive sample bias measurements are used since the intensity for electron states had less of a potential dependence. Two sample spectra obtained at 1/8 T are presented in figure 5.6 B, showing how a spectrum over the defect is shifted to

overlay the averaged spectra affected by only TIBB. This shift results in the potential change from the defect to the TIBB spectra.

A second method of extracting the local potential is performed by measuring the energy shift of LL_0. This method will not result in a one to one correspondence with the local potential because of the smoothing on the magnetic length scale. But, defects and their relative charge can be identified.[112]

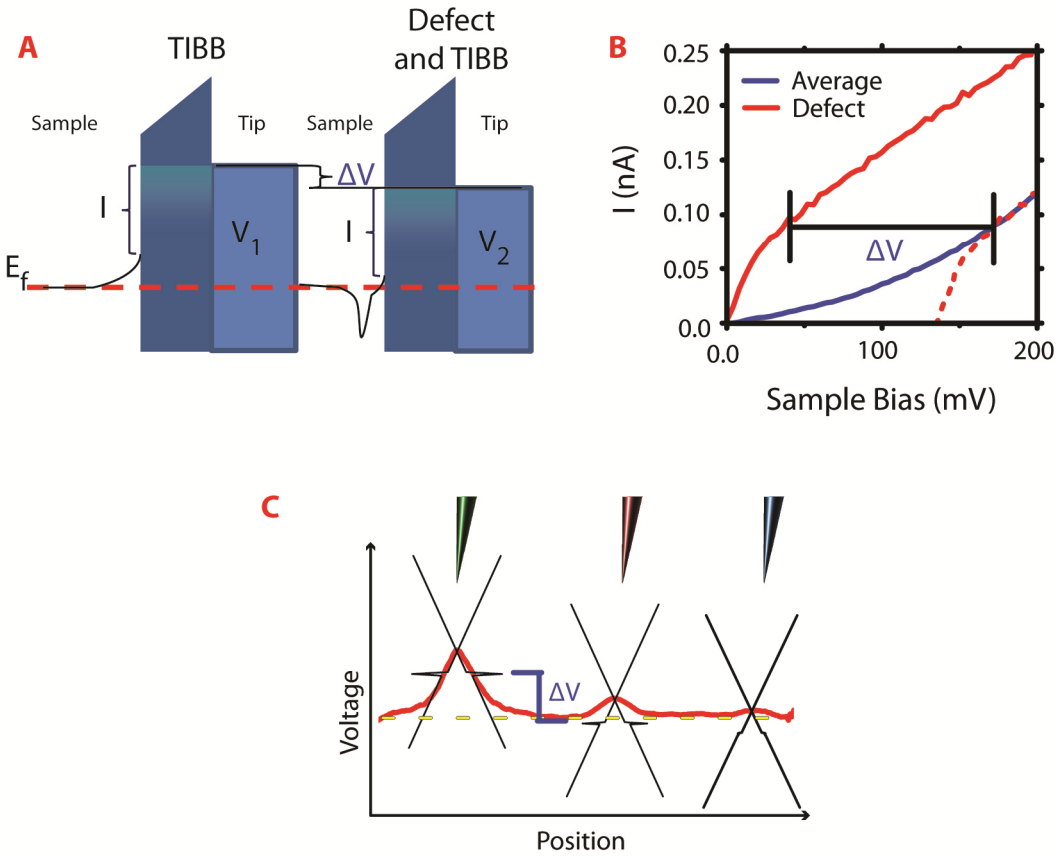

Figure 5.6: Schematics for principles used in extracting local potentials. (A) Measurements away for any defects will contain TIBB, shifting LDoS. By applying a voltage V_1 the corresponding current *I* will be obtained. Near defects LDoS will be shifted, in this case lower where a smaller voltage, V_2, is needed to obtain the same current I. By assuming a nearly constant LDoS structure the difference of these two voltages should give the local potential shift of the system. (B) This ΔV can be extracted by translating *I* vs. *V* spectra until they overlap. (C) An additional method performed relies on the tip effect being larger than the observed defect potentials. Here the location of the asymmetry is traced resulting in the local potential change.

The last technique used relies on the location of the asymmetry caused by TIBB. If this is closely related to the local potential, it should be an excellent indicator of how the potential or local doping varies.[140] By following the step from the asymmetry (figure 5.6 C) an estimate on the local potential variations was extracted.

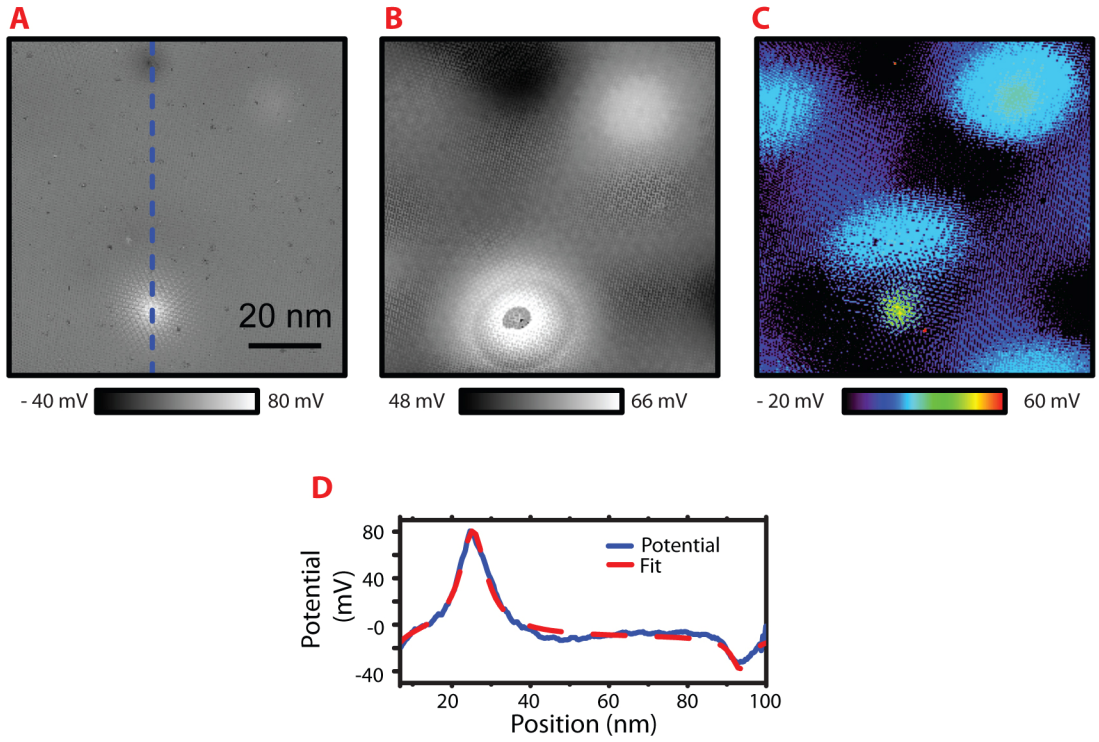

Figure 5.7: (A) Extracted electron potential maps using I vs. V spectra performed at 1/8 T, (B) LL_0 tracing performed at 8 T, and (C) asymmetry tracing from dI/dV measurements performed at 1/8 T. All three maps show similar defects, but asymmetry tracing shows additional regions which affected LDoS. (D) An extracted profile (blue) along the blue dashed line. Here the defect in the topograph has a positive potential of ~80 meV and a second defect shows the presence of a negative potential (-35 meV). The resulting fit is shown in red.

The resulting electron potential maps can be seen in figure 5.7. The current matching method (5.7 A), LL_0 energy tracing (5.7 B), and asymmetry tracing (5.7 C) identify 3 similar defects in this 92.5 nm x 92.5 nm region. The defect in the topograph identified by the green arrows has a positive potential, while the negative potential corresponds to a second defect identified by the blue arrows on line scans. Besides showing the defects, the asymmetry tracing method imparts an additional potential effect,

indicating the presence of a periodic 12 meV potential variation. This potential could be linked with the AA stacking region of a 2rd moiré pattern (not imaged), whose effects have been studied elsewhere.[76]

The observation of 3 similar defects using three different techniques from three different data sets, I, dI/dV spectra at 1/8 T, and dI/dV spectra at 8 T, indicates that the local potential has been correctly extracted. It is believed that the current spectra technique is the most precise due to the absence of smoothing on a magnetic length sampling and less of a dependence on LDoS fluctuations. An extracted potential profile is shown in figure 5.7 D. Here the potential effect of the large defect is seen to be nearly twice that of the negative potential. A fit was performed with both defects have a screened electron potential of the form:

$$V_{defect}(r) = \frac{Q}{4\pi\varepsilon_0\sqrt{r^2 + d_{defect}^2}\,\ln\left(\sqrt{r^2 + d_{defect}^2}\,/a\right)}. \qquad 56$$

The resulting fit for the positive potential gave $Q = 0.52 \pm 0.02\,e$, and $d_{defect} = 3.2 \pm 0.1$ nm, while the negative potential's best fit produced $Q = -0.06 \pm 0.01e$, and $d_{defect} = 1.9 \pm 0.3$ nm. The resulting fit is seen as the red dashed line in figure 5.7 D.

5.2.3 Modeled LL Response

By using the methods outlined in chapter 3 the expected total potential effect on the LLs can now be modeled. In figure 5.8 LL responses from the TIBB potential $\left(V_{trial}\right)$ are shown for the two most affected $|n,m\rangle$ states in $LL_{\pm1}$ and LL_0 as red dashed lines. The LL energy dependence can also be predicted directly above each defect by combining potential results in chapter 3 with the fit potential due to individual defects in 5.2.2 $\left(V_{trial} + V_{defect}\right)$. Results of predicted E_N locations above the positive potential (green dashed lines) and above the negative potential (blue lines) are shown in figure 5.8. How these LL energy positions transition from each location cannot be precisely modeled due

to the required radial symmetry, but the total predicted energy shift can be extracted from these results. Here state $|0,0\rangle$ can be seen to shift nearly 25 meV at 8 T from the positive potential defect to the negative one. This is almost exactly what was seen when LL_0 tracing was performed, figure 5.7 C. LL_0's shift was reduced by ~ 8 meV due to an ionization event, but the total energy shift between the two defects was 18 ± 2 meV at 8 T.

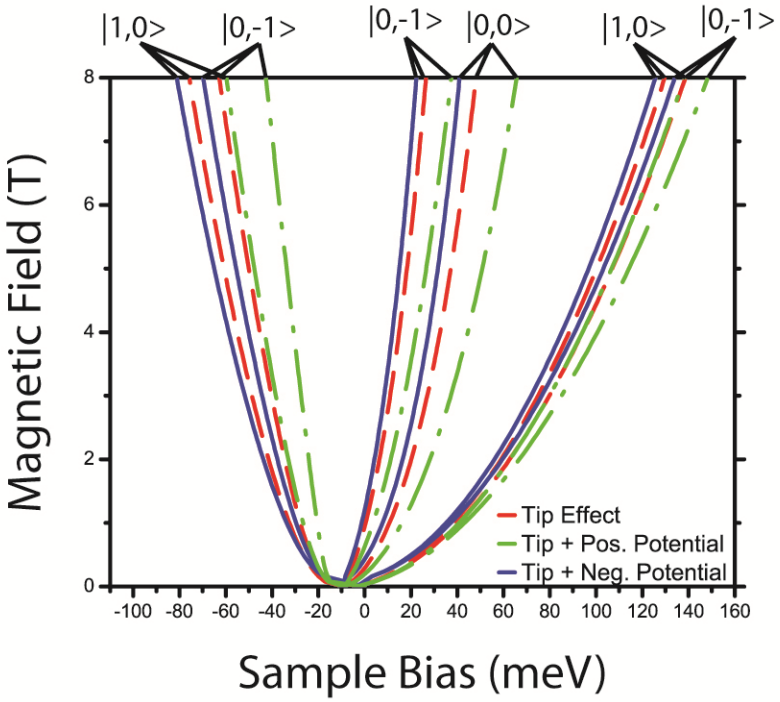

Figure 5.8: Expected $LL_{\pm1}$ and LL_0 $|n,m\rangle$ Sample Bias vs. *B* relationship for three different potential perturbations. $|n,m\rangle$ positions away from defects (red) are expected to appear similar to those of tip 2 in chapter 3. Once the tip is directly above the large positive potential (green) $|n,m\rangle$ states are seen to shift towards more positive energies. Above the negative potential (blue) states are seen to move to slightly negative values and have less of an energy difference between $|n,m\rangle$ states in the same LL.

From figure 5.8 states in LL_{-1} are expected to shift at most 20 meV from negative to positive potentials. This result is not seen unless the state that bends nearly 80 meV is a defect state and can no longer be considered a LL. If this is the case, then the remaining peaks seen in LL_{-1} remain LLs, where none are seen to shift more than 20 meV

between defects. Peaks in LL_1 are expected to change at most 14 meV and this result appears to match extracted LL energy shifts if the ionization event did not occur. Here measurements were found to have LL_1 shifting 10 ± 2 meV between the two defects. In general defect potentials added with from chapter 3 predict the behavior of LLs quite well, but there are additional defect states which appear closely tied to the local potential that will now be investigated.

5.2.4 Conductance Maps

A higher resolution (1 Å step size) conductance map was performed at 6 T over the defect with the positive potential. This resulted in the observations of multiple phenomena that will be argued to be a combination of tip effects and defect states. In particular this thesis will focus on two defect states near this defect. Defect state 1 is identified in the extracted line scan (figure 5.9 A and B) as the red line and is the only state to cross the Fermi energy. Defect state 2 is identified by the green line and is seen to split from defect state 1 before state 1 ionizes. The band, or mirror state, corresponding to when defect state 1 crosses the Fermi energy is identified by the yellow line and is known to be a TIBB effect which yields a lever arm of 10.[112, 113]

This response looks similar to that seen in figure 5.1 C, but it is believed that the defect behavior is more like the defects in 5.1 A and F. The first indication is that only one mirror state is seen for all magnetic fields, indicating that this bending band likely does not have the 4 fold degeneracy that is seen in each $|n,m\rangle$ state. Unfortunately with energy sweeps only going to 200 meV this statement cannot be completely verified due to degeneracy of defect state 2 being unobservable. Further evidence throughout this chapter will continue to verify that defect state 1 and state 2 must be treated as defect states and not LLs, but the most convincing evidence is presented in section 5.2.7 where multiple conductance line scans are given at varied magnetic fields. A charging event is believed to be seen near 100 meV (red arrow). This may indicate that state 1 can be

thought in terms of as a quantum dot state, where a second electron can be placed into the well.

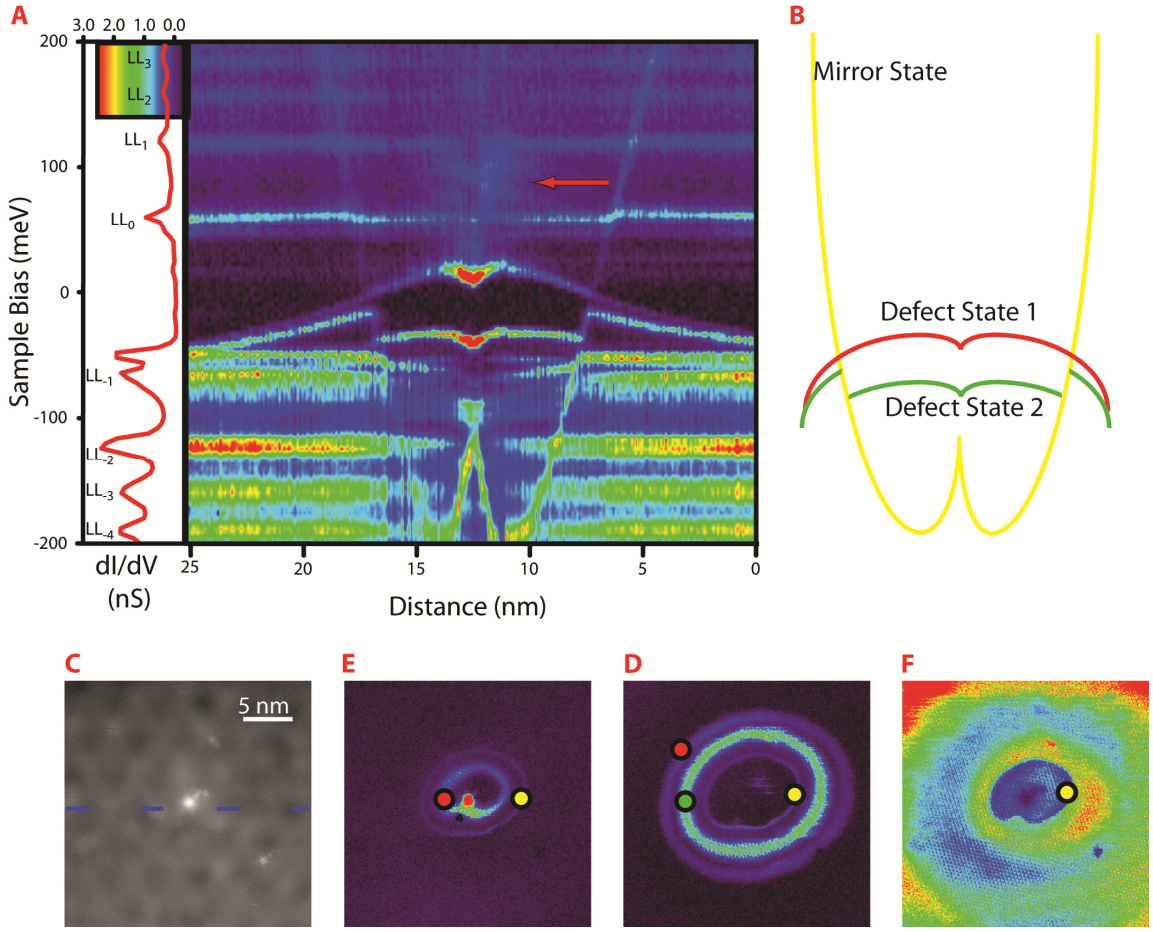

Figure 5.9: The conductance response to the positive potential. (L_25128, L_25130) (A) An extracted 6 T line scan across the defect. Bright horizontal lines correspond to LLs labeled in the included spectra. (B) Cartoon identifying defect state 1 (red), defect state 2 (green) and the mirror state (yellow). (C) The topograph for the conductance maps with the location of the extracted line scan marked as a dashed line. In the line scan two magnetically localized defect states are seen to bend in energy above the defect. (D) Defect state 1 can be seen as a ring of high conductance surrounded by zero conductance in the conductance map at 12 meV. The change of state 1 from electron to hole state as it crosses E_f causes a sharp decrease in the current, creating the W shape ionization boundary seen in the line scan and the sharp boundary in all conductance maps. Upon passing the boundary the loss of the ionized state changes the local sample potential, causing a discrete 20 meV shift for defect state 2. (E) Defect state 2 is the bright blue ring on the -24 meV conductance map. (F) LL drift states convert to localized states upon crossing the ionization boundary in the -52 meV conductance map. The red arrows in the line scan indicate where state 1 may be undergoing a charging event.

Perhaps more interesting is the spatial behavior of these defects. Conductance maps were performed on a 25 nm x 25 nm area (figure 5.9 B) where high conductance rings (figure 5.9 C and D) were seen to exist surrounded by zero conductance areas. The bending in energy of each defect state in the conductance line scan creates these rings. Figure 5.9 C shows two rings at 12 meV. The inner ring corresponds to state 1 and is seen to be affected by two defects located within 2 nm of each other. This indicates that while one large potential was measured at least two defects reside in what has been referred to as the positive potential. This ring was seen to converge to the center of the potential well caused by multiple defects at higher negative sample bias. The thinner outer ring corresponds to the ionization[38, 143, 144] of defect state 1 and is caused by creating an additional electron state for tunneling by TIBB pulling state 1 across E_f.

At -24 meV (figure 5.9 D) a ring caused by state 2 can be seen. The width of the two defect rings increases as sample bias decreases, eventually causing state 1 to be indistinguishable from state 2. State 2 appears to be discontinuous, jumping down 20 meV once it crosses the ionization boundary. This is due to the change of the local potential, where outside the ionized region state 1 is a hole state and inside state 1 is an electron state. This change in the local potential picture can be used to understand how these defect states differ from LLs. At 6 T LL_0 is seen to shift ~8 meV while LL_1 shifts at most 4 meV, consistent with the dependency expected from equation 38. This ionization effect on LLs is best seen in figure 5.9 E, where LL_{-1} transitions from an extended state, with large conductance, to a localized state, with zero conductance, once it crosses the ionization boundary. The 20 meV discontinuity indicates a large dependence on the local potential for defect state 2 and is another indication that these defect states cannot be considered LLs. Similarly this discontinuity in state 2 shows that these states are not behaving like the LL states, where the large energy jump of state 2 due to the change in potential energy cannot be modeled using states from LL_{-1} and a

perturbation potential. Hence, state 1 and state 2 are not similar to defect D3, but instead are similar to the defect D1 and D6.

5.2.5 Tip Interaction

It is believed that the 80 meV bending of state 1 is due to TIBB. In this situation the tip effect can be treated as an additional electric field, where without the tip one would observe constant energy states similar to those represented in figure 5.10 A. The black defect potential causes state 1 to have an energy state at the blue dashed line, while state 2's energy state is grey. With the addition of an electric field from the tip, the two states are believed to Stark shift to higher energies. When the tip is located above the defect (figure 5.10 B) the electric field bends the state above E_f (yellow dashed line), but as the tip moves further away the electric field effect on the defect state decreases causing less of an energy shift. Once the Stark shift ionizes state 1, the local potential decreases making state 2 appear discontinuous (figure 5.10 C). Measurements performed directly under the tip result in the observation of defect states similar to those seen in figure 5.10 D. This type of tip effect indicates that defect D1's constant energy states were due to the different macrotip which had little to no TIBB, or TIBB was on a length scale >> the macrotip for the defects that have bending energy states.

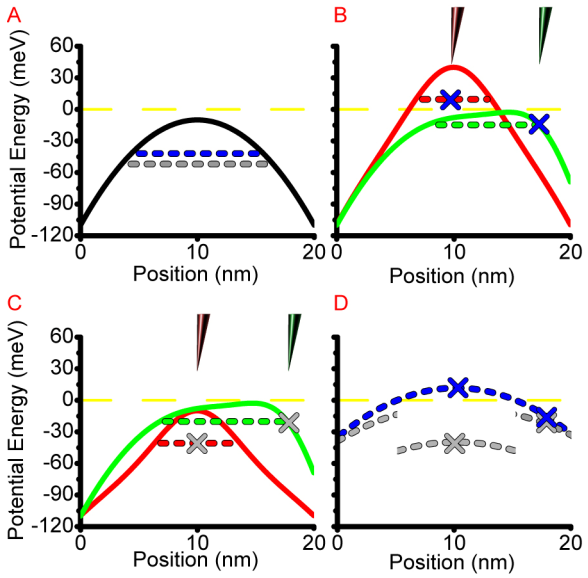

Figure 5.10: An explanation for the defects states' energy dependence. (A) Without the tip effect the potential due to the defect (black line) creates a constant energy state that splits in a magnetic field (blue/grey dashed lines). (B) The tip causes an additional electric field which Stark shifts state 1. Two tip positions are represented, 0 nm (red) and 9 nm (green) from the defect, with the measured energy state for each tip position marked with a blue X. (C) State 2 has a similar response, but once state 1 crosses E_f (yellow) the local potential decreases, causing a jump to lower measured energies for state 2 (grey X). (D) This Stark shift results in the observance of defect states which bend in energy.

5.2.6 Drift Velocity

In a magnetic field all fermions should undergo cyclotron motion while following equipotentials.[145] Since the defect states originate from LL_{-1}, it is believed that initially they follow the semi-classical picture drawn in figure 5.11. Here a simplified potential map is shown where electrons (yellow line) undergo cyclotron motion on equipotential areas colored green. In this figure the defect is located in the center while a second potential source (blue) from the tip is added to create the total local potential. The higher potential directly below the tip may affect the electron's orbit and state as was shown in chapter 3, but the total width of these cyclotron orbits should remain on the length scale of the magnetic length.

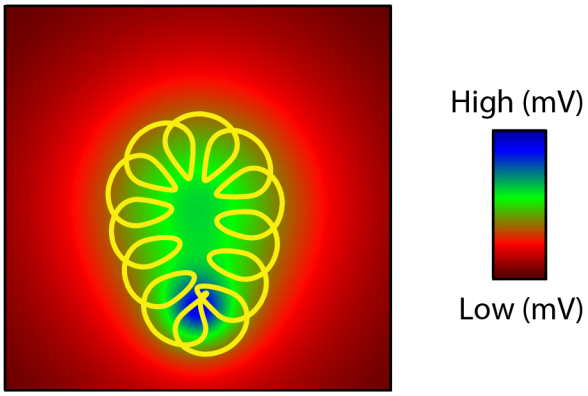

Figure 5.11: When a magnetic field is applied to graphene, fermions are expected to flow (yellow line) along equipotentials (green area), undergoing cyclotron motion. For every measurement this equipotential will be affected by the location of the tip (blue).

The defect states' high conductance rings in figure 5.9 have widths as small as 2 nm, while the magnetic length is 10.6 nm. This indicates that the local potential is changing on a smaller length scale than the magnetic length. Each time the tip is moved this potential is changed slightly, shifting the measured location of the defect states. This tip influence likely causes the states to be seen farther from the center of the defect than if there was no tip effect, but also it effectively measures where an equipotential is located. In figure 5.9 it is seen that the fermions circle in a semi elliptical orbit, but for the purposes of this thesis these orbits will be treated as circles. This allows for the extraction of the drift velocity of these fermions by equating the force due to cyclotron motion with the change in potential: $qv_d \times B = qE = q\frac{dV}{dr}$. By tracing the energy location of defect state 1 (black figure 5.12 A) $\frac{dV}{dr}$ is directly measured, and hence the drift velocity can be derived (blue curve).

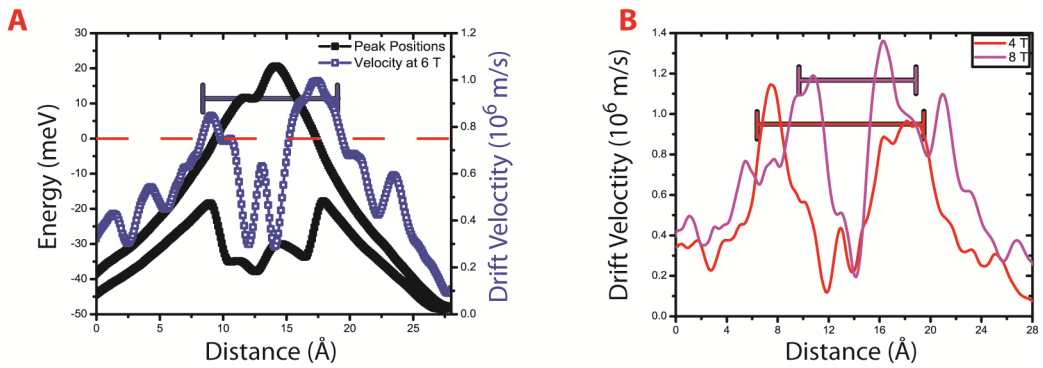

Figure 5.12: Extracted drift velocities. The drift velocity is extracted by equating the force for a fermion undergoing cyclotron motion to the force of a fermion in an electric field. (A) The velocity at 6 T (blue line) reaches its maximum when state 1's energy (upper black line) crosses E_f (red dashed line). State 2 (lower black line) is included to guide the eye. The magnetic length is identified by the blue bar. (B) Additional extracted velocities performed at 4 T and 8 T show a dependence on magnetic lengths (red a purple bars). [A: (Data extracted from L_25145) ; B: (L_25173 , L_25084)]

There are some interesting results gleaned from the extracted velocity. One is that the drift velocity reaches its maximum at nearly the Fermi velocity. At 6 T the velocity is found to maximize at exactly the Fermi velocity. In addition this maximum velocity corresponds to where the defect state crosses the Fermi energy. It is thought that before crossing E_f state 1 still resemble LLs, with fermions following equipotentials while undergoing cyclotron orbits. Once this state crosses E_f it may switch to directly orbiting the defect and can now be considered a magnetically bound defect state. If this conversion from orbiting LL state to defect state is occurring, it is expected to have a magnetic length scale dependence. Colored bars representing the magnetic length at each field have been included with the extracted velocities at 4 T and 8 T in figure 5.12 B and show this length dependence. The data suggest that the magnetic length defines the diameter in which fermions convert from the LL drift state picture to a bound defect state. A limited data set was obtained with magnetic length varying from only 13 nm to 9.2 nm for four different magnetic fields. Additional observations at different defects are needed to verify this magnetic length dependence.

5.2.7 Local Energy Pinning

The large defect was seen to be locally pinned at 10 meV above the Fermi energy when the magnetic field was varied. This pinning is seen in the multiple conductive line scans in figure 5.13. A linear fit was performed on the maximum conductance position of defect state 1 for all magnetic fields and resulted in a slope of 0.3 ± 0.3 meV/T and an intercept of 10.0 ± 1.3 meV/T. In addition the maximum in the state 2 after it has ionized was found to have a slope of -5.1 ± 0.4 meV and an intercept of -9.6 ± 1.7 meV. (Uncertainty represents one standard deviation in the measured quantity.)

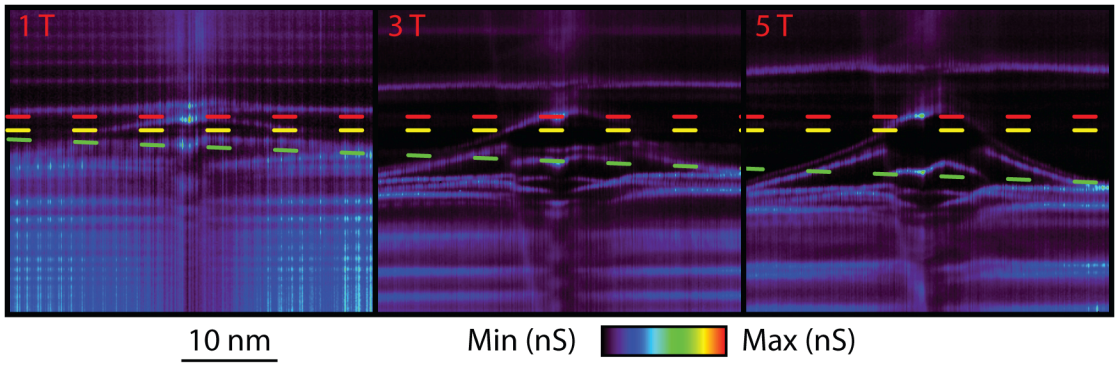

Figure 5.13: 1 T, 3 T and 5 T conductance line scans show a local pinning of defect state 1 (red dashed line) 10 meV above E_f (yellow dashed line). The maximum intensity of state 2 in the ionized region was observed to undergo a linear dependence in magnetic field (green dashed line). [1 T: (L_25154 Min = 0.0 nS, Max = 1.25 nS); 3 T: (L_25177 Min = 0.0 nS , Max = 1.0 nS); 5 T: (L_25166 Min = 0.0 nS, Max = 1.0 nS)]

Besides this local pinning the final indication that these state are indeed defect states similar to that seen in defect D1 can be seen in the 1 T and 3 T line scans of figure 5.13. Here LLs disappear within 2 nm of the defect and new states appear. In addition, the charging of state 1 can be seen to retain the same ~70 meV spacing between 3 and 5 T, while LL_0 shifts by 10 meV, again indicating this defect state cannot be considered as a splitting of $|n,m\rangle$ states in LL_{-1} due to an increased potential.

5.2.8 Radial Dependent Response

The final response observed near this defect is currently not understood. Conductance intensity is seen to have an almost step like dependence as a function of the radial

distance from the defect. Local conductance measurements were observed to vary from tip state to tip state, but this relative conductance step did not change as the tip state was modified.

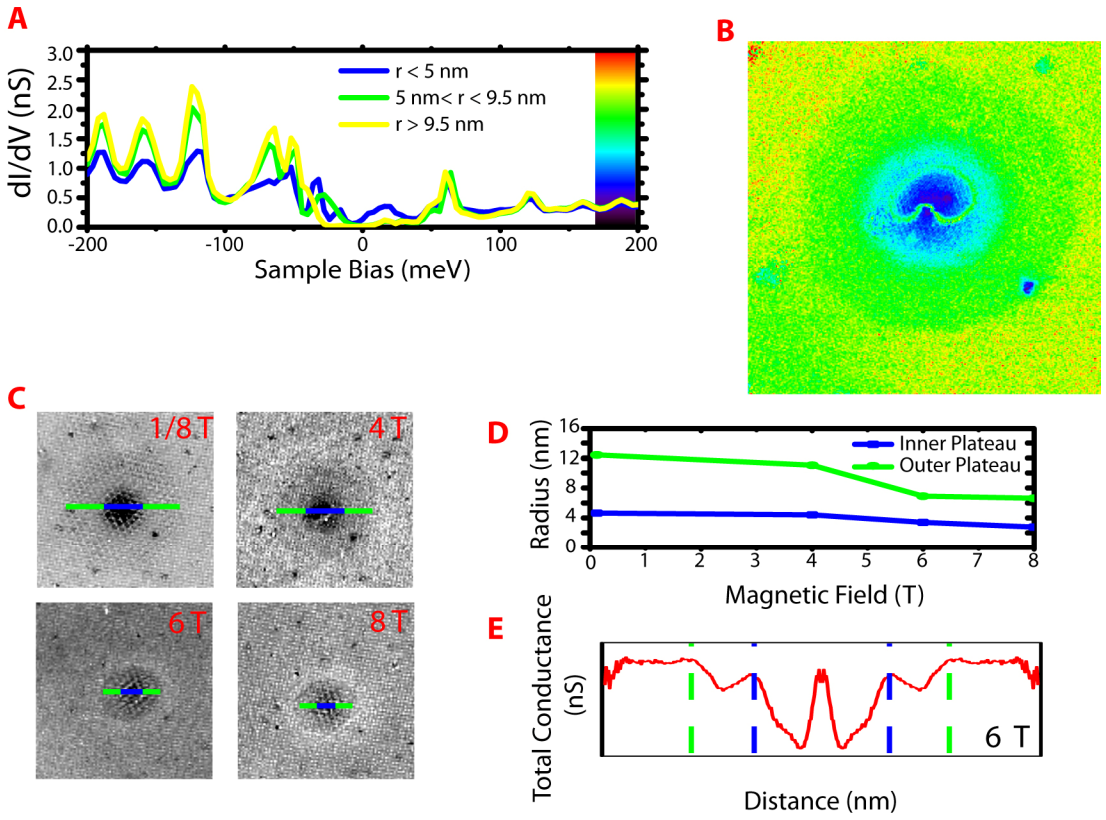

Figure 5.14: Unexplained data observed near the positive potential. (A) Radially averaged conductance measurements show a lowering of conductance as a function of radius. (B) These drops in conductance appear as plateau-like features on conductance maps. (C) Conductance maps performed at 1/8 T, 4 T, 6 T and 8 T show the presence of this feature. (D) This feature has a small dependence on magnetic field, but it is not seen to vary like the magnetic length. (E) Radially averaged total conductance readings from -200 meV to 200 meV were performed indicating a wave like structure in this feature. [B: (L_25130, $V_{Bias} = -160$ meV); 1/8 T: (L_25067, $V_{Bias} = -200$ meV); 4 T: (L_25094, $V_{Bias} = -200$ meV); 6 T: (L_24875, $V_{Bias} = -200$ meV); 8 T: (L_25084, $V_{Bias} = -200$ meV)]

Three radially averaged conductance measurement are seen in figure 5.14 A. The spectra shown fall into three regions: $r < 5$ nm (blue), $5 < r < 9.5$ nm (green), and $r > 9.5$ nm (yellow). As the radius increases conductance is observed to increase. To

highlight this spatial dependence a sample conductance map has been included in figure 5.14 B at -160 meV. Here the ionization boundary is the green region inside a radius of 5 nm. Figure 5.14 C shows that these plateau-like features are present at all measured fields and that while the radius does vary slightly as magnetic field changes, it does not appear to depend on the magnetic length (figure 5.14 D). In an attempt to classify this effect, a radial averaged sum of the total conductance measured between -200 and 200 meV was performed on the 25 nm map. Here it can be seen that these steps have a wave like structure. Previous results of Te-doped GaAs have seen somewhat similar structures identified as Friedel charge-density oscillations,[146] but if these were Friedel oscillations then it should be apparent in the topographs. Only a 350 mV set point image was performed, but at this voltage no oscillations were seen.

5.3 Defect Summary

By using results from chapter 3 the bending and degeneracy splitting of $|n,m\rangle$ states from tip effects was shown to be influenced by local potential variations caused by defects. In particular defects along with TIBB effect were shown to nearly cancel each other out resulting in nearly ideal graphene spectra. Electron-hole asymmetries can be explained due to repulsive versus attractive scattering. Additional magnetically bound defect states responded directly to potential changes, unlike LLs, bending in energy from a Stark effect due to the tip and shifting ~ 20 meV from ionization events. These defect states appear to originate from LL_{-1} and were observed to pin the local Fermi energy. Extracted drift velocities are believed to indicate the transition from the semi-classical drift state picture to a magnetically bound defect state. The final observation was plateau like features seen in conductance measurements which indicate an unknown radial dependence of the LDOS near defects.

CHAPTER 6

CONCLUDING REMARKS

Low temperature scanning tunneling microscopy and spectroscopy experiments were performed in magnetic fields to study graphene's massless fermion behavior. In chapter 3 it was shown that these measurements indicated an influence due to the tip. This influence was modeled as a capacitive gating effect due to the applied bias and as a finite potential well due to the work function difference between graphene and Ir. A technique involving degenerate perturbation theory on LL states solved in the symmetric gauge resulted in the extraction of this finite potential. These results indicated that the tip can be considered as a defect, and indicated that the tip can be used to influence graphene's LDoS. This may signify that the tip effect could be used as a controlled charged defect, where one could control the effective charge of the defect by changing the applied bias on the tip. The influence of a single controlled defect charge could be performed by using this tip effect in conjunction with transport measurements. This method of extracting the tip-induced band bending has also been shown to provide a route towards studying nanometer scale screening effects in graphene. While the current results do not indicate a definitive model (the unscreened, screened, and spherical models resulted in nearly identical fit accuracies), it is the hope of the author that more advanced tip simulations (e.g. hyperbolic tip models) may result in a decidedly better fit.

In chapter 4 a new tunneling technique was performed where the magnetic field was varied while conductance measurements were collected. This resulted in a highly precise measurement of the energy and momentum space relationship in graphene, and indicated that the top layer of multilayer epitaxial graphene follows the Dirac dispersion of monolayer graphene. Measurements were observed to remain susceptible to the gating influence of the tip, but the finite potential caused by the tip had little influence on the

resulting energy and momentum due to the reliance on higher indexed LLs. Observations of linear oscillations in measurements indicated an Aharonov-Bohm effect may be present due to tip-induced band bending. It is the author's belief that this technique can be slightly modified in order to directly measure the local density of states as a function of both energy and magnetic field in a single measurement. In particular it is hoped that additional research can be performed at low fields to better understand the unique LDoS structure reported on in appendix A.

Finally in chapter 5 defect effects were placed into two categories. One category contained defects that were observed to create local potentials, where their effect on the LDoS could be modeled by adding the defect's potential with the tip's potential and using the perturbation method described in chapter 3. The second type of defect was observed to create new states a few nanometers from the defect at an energy between LLs. It is the belief of the author that if there were enough of these type of defects the observation of the half-integer quantum Hall effect would be nearly impossible in transport measurements. These defect states were observed to Stark shift in energy from the local electric field created by the STM tip.

Tip influences were shown to be present in nearly every measurement performed. This influence was shown to be heavily dependent on the microtip state and it is believed that this influence can be reduced by using tip materials that closely match graphene's work function. It is the author's conviction that understanding the influence of the tip potential will be particularly important for correctly interpreting the physics underlying correlation-induced energy gaps measured by STS.

APPENDIX A

ADDITIONAL TMCO OBSERVATIONS

A.1 Low Field Oscillations

Both weak localization[147] and weak anti-localization[126] have both been observed in graphene at small magnetic fields. Likewise, the low-field form of TMCO spectra is intriguing. Additional bias dependent TMCO sweeps were performed to clarify results from *Z* vs. *B* measurements which indicated a sudden decrease in conductance in fields less than 0.15 T (figure 4.1). These measurements also produced puzzling results that have yet to be explained. In this appendix the low-field TMCO data is presented, and discussed in the context of physical effects known from electrical transport experiments.

The literature shows that in single layer graphene weak anti-localization can be identified with the observance of negative magneto-conductance.[148] Additionally, by varying a back gate, transitions to weak localization (positive magneto-conductance) were observed at low fields.[149] Similar behavior is seen in the small field TMCO scans, shown in figure A.1 and A.2. Spectra obtained within 5 meV of the Dirac point have negative magneto-conductance values (figure A.1 at 25 meV and 35 meV and figure A.2 at 30 meV). Temperature dependence measurements were not performed, yet the negative magneto-conductance paired with the decrease in *Z* height were strong indications that weak anti-localization occurs at low fields near the Dirac point. The remaining spectra that were obtained all have positive conductance values indicating the presence of weak localization when sampling away from the Dirac point.

In an attempt to understand the additional structure seen in all spectra, data has been split into two types of phenomena. The first type of data is presented in figure A.1. This type of low field spectra had nearly identical responses recorded for both magnetic field sweeping directions once the hysteresis was removed. Spectra in figure A.1 have

been placed on equivalent, but offset 1nS scales. In general there is always a local minima/maxima located at zero magnetic field and within 0.05 T where an additional minima/maxima can be identified, dots have been used to guide the eye. It is extremely difficult to categorize these small oscillations, where it could be argued that the spectrum obtained at -55 meV contain instead larger local minima instead of maxima. What one can state is that for all sample bias measurements within 0.1 T of 0 T, there is a relatively large peak not attributed to LL when compared to the averaged conductance measurements within 0.5 T. This structure is evident in all sweeps and a peak height comparison to LLs can be seen in figure 4.3. Spectra's minima and maxima do not always repeat as seen in 25 and 50 meV. In these examples spectrum switch from maxima peaks when magnetic sweeping direction is changed. In addition two of these minima appear to occasionally be absorbed into the background spectrum such as seen for 50 meV.

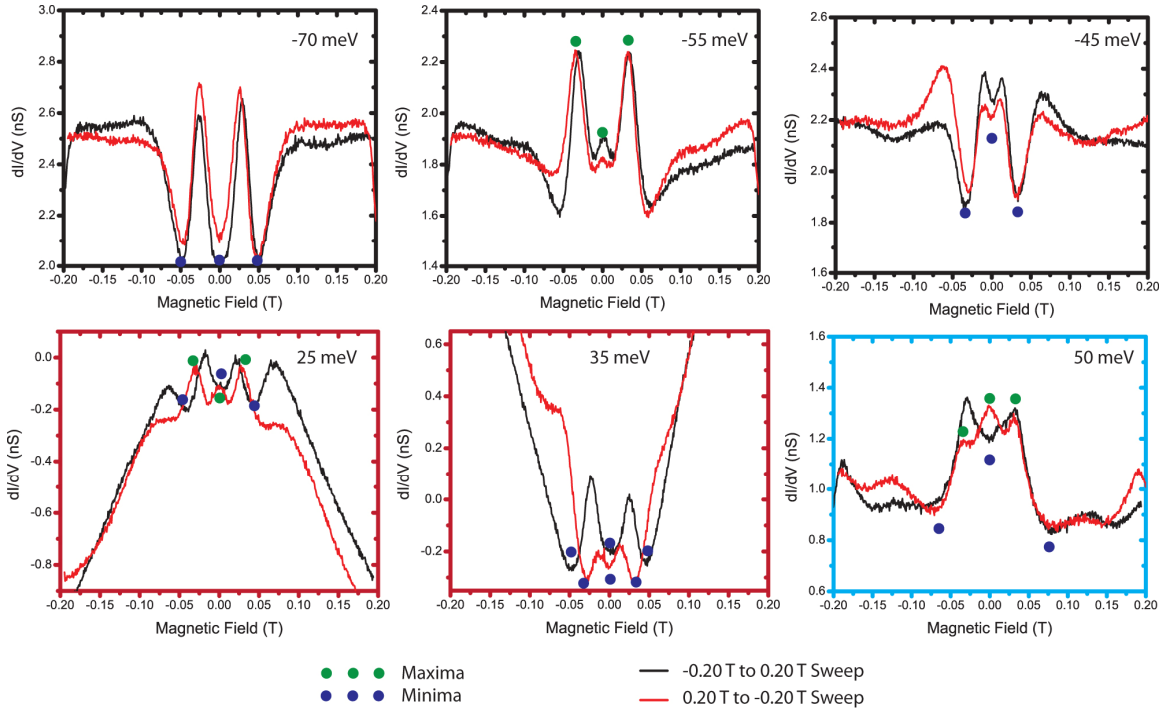

Figure A.1: Semi symmetric low field TMCO results. [Selected results spectra from L_25903 to L_25961, settings set by table 4.1]

The effects of three minima or three maxima were again seen in spectra of type 2, but additional sweep direction dependencies occur on the magneto-conductance (figure A.2). In spectra obtained at -60 meV spectrum appear to have a much higher conductance measurement where magnetic field sweeps began, but as the sweep progressed the conductance was seen to decrease. This leads towards a mirror like effect where positive to negative sweeps can be made to match negative to positive sweeps by reflecting across the 0 T axis. In addition to this magnetic sweep dependence spectra obtained at 30, 50 and 65 meV exhibited an unexplained inversion of conductance when hanging the sweep direction. The two sets of spectra (blue box) shown in figures A.1 and A.2 were obtained in the same location, but 4 hours apart. Interestingly the local minima for negative to positives sweeps performed at 50 meV in figure A.2 are easily identifiable, while this was not the case in figure A.1. But for positive to negative sweeps in figure A.2 local minima sweeps are nearly hidden, which is a complete reversal of behavior. Though, both sets of measurements do exhibit the same minima/maxima behavior.

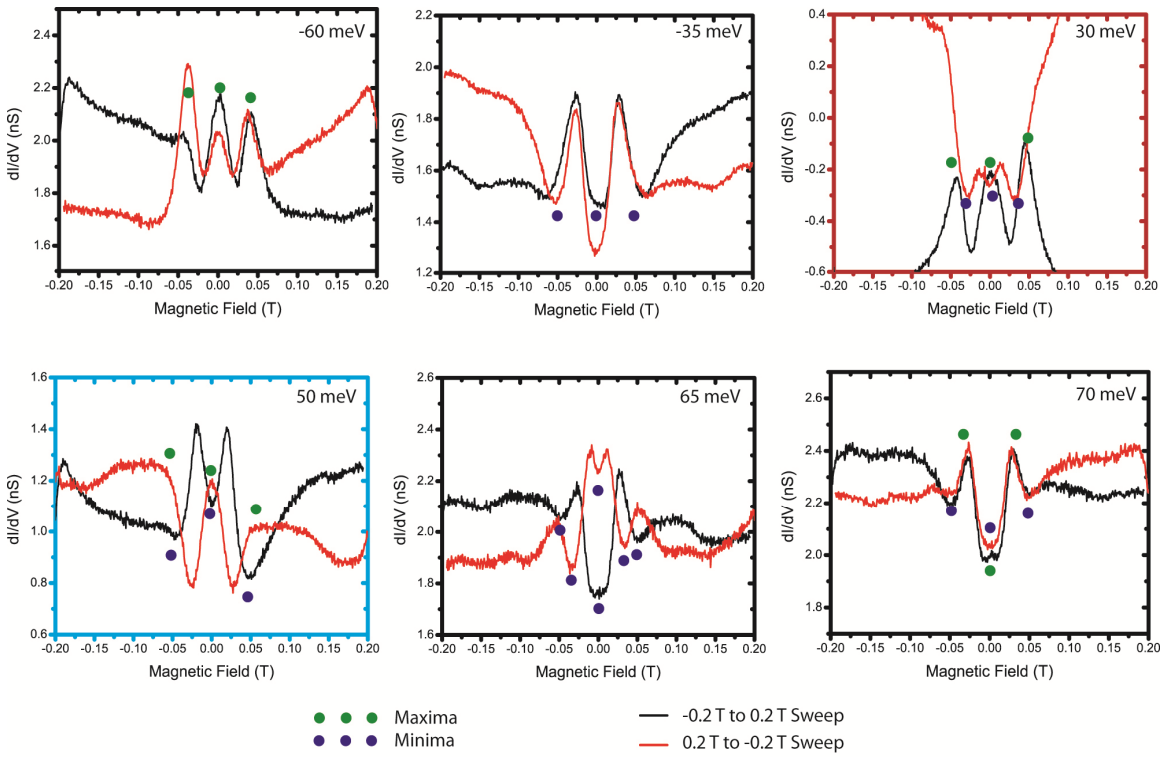

Figure A.2: Sweep direction dependent low field TMCO results. [Selected results spectra from L_25903 to L_25961, settings use table 4.1]

The structure in these low field oscillations could be due to universal conductance fluctuations (UCF).[150] It is reasonable to assume that if they were due to UCF, then changes in atomic location or drift would account for discrepancies in repeat spectra. While focused low field studies were not performed in different locations, similar irregular results with conductance peaks within -0.05 T to 0.05 T were seen on all TMCO sweeps. Additional studies were performed to measure the effect of the magnetic field ramp rate and produced conflicting results. In figure A.3 a gradual change in conductance responses was observed. Spectra were obtained at 55 mV by ramping from 0.2 to -0.2 T (figure A.3 A) and then back (figure A.3 B), where the only change was the magnetic ramp rate being varied from 0.06 T/min to 0.03 T/min. While performing these measurements the local minima at 0 T on both ramping directions was observed to decrease in intensity by nearly a multiple of 6. Concurrently the conductance difference

between 0.1 T and 0.05T was seen to increase by a multiple of 3 from 0.06 T/min scans to 0.03 T/min scans.

Tests to observe if conductance had a dependence on the total magnetic field swept were then performed at 0.04 T/min after the ramp rate tests. Spectra were found to have changed to produce a reproducible local maximum at 0 T, figure A.3 C, for positive to negative field sweeps, while the local minimum for sweeps from negative to positive fields, figure A.3 D, disappeared by the sweep from -0.1 T to 0.1 T.

Similar magnetic rate dependence measurements were then performed at -55 mV (figure A.3 E and F) and resulted in completely different results. When sweep rates were changed from 0.06 T/min to 0.03 T/min the overall conductance changed by nearly a factor of 2 from -0.1 T to -0.5 T, but the local minima and maxima intensity underwent little to no change. Drift rates between the tip and sample should have been nearly identical in both ramp rate tests, since measurements were performed 48 hours after a course move and each 42 minute ramp speed data set was obtained within 15 minutes of each other.

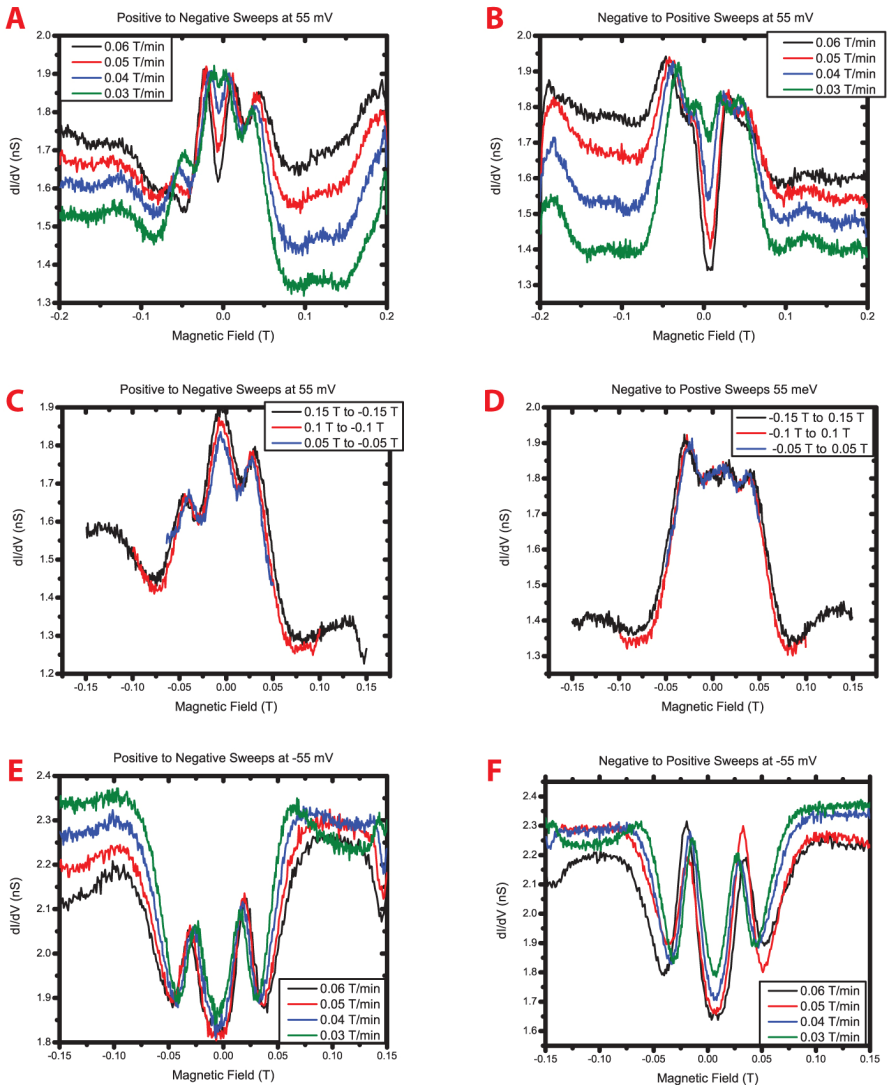

Figure A.3: Low field magnetic ramp rate dependence (L_25962 to L_25983, settings set by table 4.1 except where indicated). (A, B) The ramp speeds are shown to change the small oscillations near 0 T when tunneling at 55 mV. (C, D) This large change was not present when ramp width effects were checked. (E, F) When tunneling at -55 meV, changes in the local minimum/maximum structure did not occur as the magnetic ramp rate was again varied.

It is believed that these effects are not tip or defect related. Changes in either of those effects should have caused nearly instantaneous responses, not the gradual progression seen in figure 4.12. A slight, 0.004 K, decrease in temperature was observed as ramping rates decreased, but if these were UCF this variance would be too small to cause a change of a multiple of 6. Similar oscillations are still seen in magneto-

conductance measurements after UCF have been removed by averaging data accumulated over a range of back gate biases. It is unknown if those oscillations are due to remaining unfiltered UCF, or some other phenomena such as Reshaba spin-orbit interactions. All that can be definitely stated is that these structured patterns are not explained by current weak localization and anti-localization theory. Additional data is needed to truly distinguish these effects from UCF.

A.2 E vs. B Maps

Nearly 300 different magnetic sweep measurements were performed for this study, making it nearly impossible to observe all data as single spectra. It was decided that E vs. *B* images, with intensity correlating to conductance measurements, should be constructed. These images can be seen in figure A.4. Data from low field (-0.2 to 0.2 T) is shown in 4.13 A and B. Unfortunately sampling was sporadic at best, with data collected at irregular intervals, ranging from 5 meV sampling to 20 meV sampling. Interpolation was performed and some identifiable structure can be seen. In particular, by using equation 13, an E vs. *V* plot was made and then resampled at the data sampling intervals and interpolated. By comparing the data to the theoretical model (4.13 C) the total background conductance intensity for spectra near the Dirac point can be seen to be due to LL_0 and the conductance gap to $LL_{\pm 1}$. The added small oscillation occurs where discrete LLs should be indistinguishable, and must be due to some other phenomena.

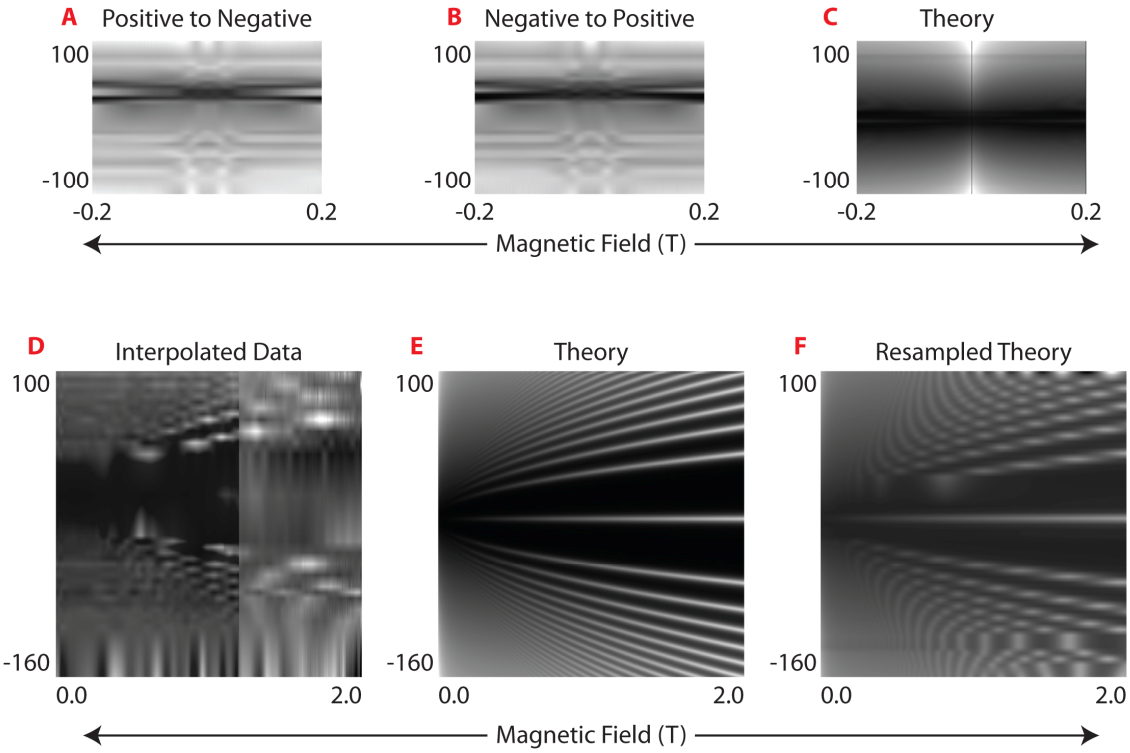

Figure A.4: Compiled and interpolated E vs. B maps (sampled spectra from L_25702 to L_25961, impedance normalization was performed when needed). (A) Low field data collected from sweeps performed from 0.2 T to -0.2 T, black/white scale 2.75 nS. (B) Low field data collected from sweeps performed from -0.2 T to 0.2 T, black/white scale 2.75 nS. (C) A theoretical model was created using equation 13, with each Lorentzian energy peak spread having a filling factor according to equation 40. (D) E vs. B maps from interpolated data ranging from 0 to 2.0 T black/white scale 10 nS. Two different interpolations were performed and merged, due to the higher number of samples performed from 0 to 1.2T compared to 0 to 2.0 T. (E) Ideal graphene's E vs. B LL response according to equation 13. (F) The resulting theoretical prediction when data is resampled to match interpolated data sampling.

In figure A.4 D spectra obtained on larger scans have been plotted on E vs. *B*. Interpolation was performed this time with different sampling resolutions below and above 1.2 T. Results can be compared to ideal graphene's LL structure seen in 4.13 E, but much of the added structure can be seen to be due to limited energy sampling as seen in the resample theoretical model 4.13 F.

It is the authors hope that eventually E vs. B maps will be able to be performed using methods similar to those performed for conductance line scan. Where while the magnetic field is slowly changed, the tip can be taken out of the servo loop, STS

measurements can be performed, and the tip can then be placed back into the loop. In principle measurements from 0 to 2.0 T could be performed with a magnetic sweep rate of 0.01 T /min while spectroscopy measurements could be performed within 40 ms resulting in magnetic field variations of 0.4 mT. Hopefully in the near future this procedure will be performed and local measurements of high density E vs. B maps will be obtainable within 3.5 hours of data acquisition.

REFERENCES

1. *Web of Science*. 2011, Thomson Reuters.

2. *Graphene Week*. 2010; Available from: http://www.nanocenter.umd.edu/grapheneweek/.

3. *International Symposium on the Science and Technology of Epitaxial Graphene*. 2010; Available from: http://www.steg2.gatech.edu/.

4. Novoselov, K.S., et al., *Two-dimensional gas of massless Dirac fermions in graphene.* Nature, 2005. **438**(7065): p. 197.

5. Zhang, Y., et al., *Experimental observation of the quantum Hall effect and Berry's phase in graphene.* Nature, 2005. **438**(7065): p. 201.

6. Young, A.F. and P. Kim, *Quantum interference and Klein tunnelling in graphene heterojunctions.* Nat Phys, 2009. **5**(3): p. 222.

7. Lin, Y.-M., et al., *100-GHz Transistors from Wafer-Scale Epitaxial Graphene.* Science, 2010. **327**(5966): p. 662.

8. Kim, K.S., et al., *Large-scale pattern growth of graphene films for stretchable transparent electrodes.* Nature, 2009. **457**(7230): p. 706.

9. Tzalenchuk, A., et al., *Towards a quantum resistance standard based on epitaxial graphene.* Nat Nano, 2010. **5**(3): p. 186.

10. Bolotin, K.I., et al., *Temperature-Dependent Transport in Suspended Graphene.* Physical Review Letters, 2008. **101**(9): p. 096802.

11. Orlita, M., et al., *Approaching the Dirac Point in High-Mobility Multilayer Epitaxial Graphene.* Physical Review Letters, 2008. **101**(26): p. 267601.

12. Bae, S., et al., *Roll-to-roll production of 30-inch graphene films for transparent electrodes.* Nat Nano, 2010. **5**(8): p. 574.

13. Silverberg, K. *Vorbeck Materials announces collaboration with PNNL to develop graphene product for batteries*. 2010; Available from: http://www.businesswire.com/news/home/20100713006946/en/Vorbeck-Materials-announces-collaboration-PNNL-develop-graphene.

14. Sprinkle, M., et al., *Scalable templated growth of graphene nanoribbons on SiC.* Nat Nano, 2010. **5**(10): p. 727.

15. *Institute for Nanolectronics Discovery and Exploration (INDEX)*. 2011; Available from: http://www.src.org/program/nri/index/about/.

16. Boehm, H.P., et al., *"Das Adsorptionsverhalten sehr dünner Kohlenstoffolien".* Zeitschrift für anorganische und allgemeine Chemie, 1962. **316**(3–4): p. 119.

17. Kittel, C., ed. *Solid State Physics*. 1996, John Wiley and Sons, Inc.: Hoboken, NJ.

18. R. Saito, G.D., and M. S. Dresselhaus, ed. *Physical Properties of Carbon Nanotubes*. 1998, Imperial College Press: London.

19. Gavryushin, V. *"Graphene Brillouin Zone and Electronic Energy Dispersion" from The Wolfram Demonstrations Project*. Available from: http://demonstrations.wolfram.com/GrapheneBrillouinZoneAndElectronicEnergyDispersion/.

20. Ando, T., T. Nakanishi, and R. Saito, *Berry's Phase and Absence of Back Scattering in Carbon Nanotubes.* J. Phys. Soc. Jpn., 1998. **67**(8): p. 2857.

21. Zheng, Y. and T. Ando, *Hall conductivity of a two-dimensional graphite system.* Physical Review B, 2002. **65**(24): p. 245420.

22. Slonczewski, J.C. and P.R. Weiss, *Band Structure of Graphite.* Phys. Rev., 1958. **109**(2): p. 272.

23. Chen, H.-Y., V. Apalkov, and T. Chakraborty, *Fock-Darwin States of Dirac Electrons in Graphene-Based Artificial Atoms.* Physical Review Letters, 2007. **98**(18): p. 186803.

24. Davies, J., ed. *The Physics of Low-Dimensional Semiconductors*. 1998, Cambridge University Press: New York, NY.

25. Yang, C.H., F.M. Peeters, and W. Xu, *Landau-level broadening due to electron-impurity interaction in graphene in strong magnetic fields.* Physical Review B, 2010. **82**(7): p. 075401.

26. Bolotin, K.I., et al., *Observation of the fractional quantum Hall effect in graphene.* Nature, 2009. **462**(7270): p. 196.

27. Chakraborty, T., ed. *Quantum Dots*. 1999, Elsevier: Amsterdam.

28. Weisstein, E.W. *Laguerre Polynomial*. Available from: http://mathworld.wolfram.com/LaguerrePolynomial.html.

29. Goerbig, M.O., *Quantum Hall Effects.* 2009.

30. Goerbig, M.O., *Electronic Properties of Graphene in a Strong Magnetic Field.* 2010.

31. Martin, J., et al., *Observation of electron-hole puddles in graphene using a scanning single-electron transistor.* Nat Phys, 2008. **4**(2): p. 144.

32. Bolotin, K.I., et al., *Ultrahigh electron mobility in suspended graphene.* Solid State Communications, 2008. **146**(9-10): p. 351.

33. Meyer, J.C., et al., *The structure of suspended graphene sheets.* Nature, 2007. **446**(7131): p. 60.

34. Castro, E.V., et al., *Limits on Charge Carrier Mobility in Suspended Graphene due to Flexural Phonons.* Physical Review Letters, 2010. **105**(26): p. 266601.

35. Rutter, G.M., et al., *Scattering and Interference in Epitaxial Graphene.* Science, 2007. **317**(5835): p. 219.

36. Hashimoto, A., et al., *Direct evidence for atomic defects in graphene layers.* Nature, 2004. **430**(7002): p. 870.

37. Palacios, J.J., et al., *Vacancy-induced magnetism in graphene and graphene ribbons.* Physical Review B, 2008. **77**(19): p. 195428.

38. Brar, V.W., et al., *Gate-controlled ionization and screening of cobalt adatoms on a graphene surface.* Nat Phys, 2011. **7**(1): p. 43.

39. Shytov, A.V., M.I. Katsnelson, and L.S. Levitov, *Atomic Collapse and Quasi–Rydberg States in Graphene.* Physical Review Letters, 2007. **99**(24): p. 246802.

40. Zhang, Z.Z., K. Chang, and F.M. Peeters, *Tuning of energy levels and optical properties of graphene quantum dots.* Physical Review B, 2008. **77**(23): p. 235411.

41. Paredes, J.I., et al., *Atomic Vacancy Engineering of Graphitic Surfaces: Controlling the Generation and Harnessing the Migration of the Single Vacancy.* The Journal of Physical Chemistry C, 2009. **113**(23): p. 10249.

42. Lahiri, J., et al., *An extended defect in graphene as a metallic wire.* Nat Nano, 2010. **5**(5): p. 326.

43. S H M Jafri, K.C., E Widenkvist, T Blom, B Sanyal, J Fransson, O Eriksson, U Jansson, H Grennberg, O Karis, R A Quinlan, B C Holloway and K Leifer, *Conductivity engineering of graphene by defect formation* J. Phys. D: Appl. Phys., 2010 **43** (4).

44. Novoselov, K.S., et al., *Electric Field Effect in Atomically Thin Carbon Films.* Science, 2004. **306**(5696): p. 666.

45. Tan, Y.W., et al., *Measurement of Scattering Rate and Minimum Conductivity in Graphene.* Physical Review Letters, 2007. **99**(24): p. 246803.

46. Geim, A.K. and K.S. Novoselov, *The rise of graphene.* Nat Mater, 2007. **6**(3): p. 183.

47. Du, X., et al., *Approaching ballistic transport in suspended graphene.* Nat Nano, 2008. **3**(8): p. 491.

48. Dean, C.R., et al., *Boron nitride substrates for high-quality graphene electronics.* Nat Nano, 2010. **5**(10): p. 722.

49. Dean, C.R., et al., *Multicomponent fractional quantum Hall effect in graphene.* (arXiv:1010.1179v1 [cond-mat.mes-hall]).

50. Wang, D., et al., *Manipulating Graphene Mobility and Charge Neutral Point with Ligand-Bound Nanoparticles as Charge Reservoir.* Nano Letters, 2010. **10**(12): p. 4989.

51. Dai, H., *Carbon nanotubes: opportunities and challenges.* Surface Science, 2002. **500**(1-3): p. 218.

52. Ismach, A., et al., *Direct Chemical Vapor Deposition of Graphene on Dielectric Surfaces.* Nano Letters, 2010. **10**(5): p. 1542.

53. Reina, A., et al., *Large Area, Few-Layer Graphene Films on Arbitrary Substrates by Chemical Vapor Deposition.* Nano Letters, 2008. **9**(1): p. 30.

54. Chae, S.J., et al., *Synthesis of Large-Area Graphene Layers on Poly-Nickel Substrate by Chemical Vapor Deposition: Wrinkle Formation.* Advanced Materials, 2009. **21**(22): p. 2328.

55. N'Diaye, A.T., et al., *Structure of epitaxial graphene on Ir(111).* New Journal of Physics, 2008. **10**(4): p. 043033.

56. Marchini, S., et al., *Scanning tunneling microscopy of graphene on Ru(0001).* Physical Review B, 2007. **76**(7): p. 075429.

57. Kwon, S.-Y., et al., *Growth of Semiconducting Graphene on Palladium.* Nano Letters, 2009. **9**(12): p. 3985.

58. Van Bommel, A.J., J.E. Crombeen, and A. Van Tooren, *LEED and Auger electron observations of the SiC(0001) surface.* Surface Science, 1975. **48**(2): p. 463.

59. Berger, C., et al., *Ultrathin Epitaxial Graphite: 2D Electron Gas Properties and a Route toward Graphene-based Nanoelectronics.* The Journal of Physical Chemistry B, 2004. **108**(52): p. 19912.

60. Berger, C., et al., *Electronic Confinement and Coherence in Patterned Epitaxial Graphene.* Science, 2006. **312**(5777): p. 1191.

61. First, P.N., et al., *Epitaxial Graphenes on Silicon Carbide.* MRS Bulletin, 2010. **35**(4): p. 296.

62. Sprinkle, M., et al., *First Direct Observation of a Nearly Ideal Graphene Band Structure.* Physical Review Letters, 2009. **103**(22): p. 226803.

63. de Heer, W.A., et al., *Epitaxial graphene.* Solid State Communications, 2007. **143**(1-2): p. 92.

64. Hass, J., W.A. de Heer, and E.H. Conrad, *The growth and morphology of epitaxial multilayer graphene.* Journal of Physics: Condensed Matter, 2008. **20**(32): p. 323202.

65. Cambaz, Z.G., et al., *Noncatalytic synthesis of carbon nanotubes, graphene and graphite on SiC.* Carbon, 2008. **46**(6): p. 841.

66. Prakash, G., et al., *Nanomanipulation of ridges in few-layer epitaxial graphene grown on the carbon face of 4H-SiC.* New Journal of Physics, 2010. **12**(12): p. 125009.

67. Li, X., et al., *Top- and side-gated epitaxial graphene field effect transistors.* physica status solidi (a), 2010. **207**(2): p. 286.

68. Rutter, G.M., et al., *Imaging the interface of epitaxial graphene with silicon carbide via scanning tunneling microscopy.* Physical Review B, 2007. **76**(23): p. 235416.

69. Riedl, C., et al., *Quasi-Free-Standing Epitaxial Graphene on SiC Obtained by Hydrogen Intercalation.* Physical Review Letters, 2009. **103**(24): p. 246804.

70. Shen, T., et al., *Observation of quantum-Hall effect in gated epitaxial graphene grown on SiC (0001).* Applied Physics Letters, 2009. **95**(17): p. 172105.

71. Riedl, C. and et al., *Structural and electronic properties of epitaxial graphene on SiC(0 0 0 1): a review of growth, characterization, transfer doping and hydrogen intercalation.* Journal of Physics D: Applied Physics, 2010. **43**(37): p. 374009.

72. Wu, X., et al., *Half integer quantum Hall effect in high mobility single layer epitaxial graphene.* Applied Physics Letters, 2009. **95**(22): p. 223108.

73. Kuwabara, M., D.R. Clarke, and D.A. Smith, *Anomalous superperiodicity in scanning tunneling microscope images of graphite.* Applied Physics Letters, 1990. **56**(24): p. 2396.

74. Miller, D.L., et al., *Observing the Quantization of Zero Mass Carriers in Graphene.* Science, 2009. **324**(5929): p. 924.

75. Sadowski, M.L., et al., *Landau Level Spectroscopy of Ultrathin Graphite Layers.* Physical Review Letters, 2006. **97**(26): p. 266405.

76. Miller, D.L., et al., *Real-space mapping of magnetically quantized graphene states.* Nat Phys, 2010. **6**(10): p. 811.

77. Miller, D.L., *Atomic-Scale Spectroscopy and Mapping of Magnetic States in Epitaxial Graphene*, in *Physics*. 2010, Georgia Institute of Technology: Atlanta, GA.

78. Biedermann, L.B., et al., *Insights into few-layer epitaxial graphene growth on 4H-SiC(000-1) substrates from STM studies.* Physical Review B, 2009. **79**(12): p. 125411.

79. Shen, T., et al., *Magnetoconductance oscillations in graphene antidot arrays.* Applied Physics Letters, 2008. **93**(12): p. 122102.

80. Mele, E.J., *Commensuration and interlayer coherence in twisted bilayer graphene.* Physical Review B, 2010. **81**(16): p. 161405.

81. Lopes dos Santos, J.M.B., N.M.R. Peres, and A.H. Castro Neto, *Graphene Bilayer with a Twist: Electronic Structure.* Physical Review Letters, 2007. **99**(25): p. 256802.

82. Trambly de Laissardière, G., D. Mayou, and L. Magaud, *Localization of Dirac Electrons in Rotated Graphene Bilayers.* Nano Letters, 2010. **10**(3): p. 804.

83. Giaever, I., *Electron Tunneling Between Two Superconductors.* Physical Review Letters, 1960. **5**(10): p. 464.

84. Young, R., J. Ward, and F. Scire, *The Topografiner: An Instrument for Measuring Surface Microtopography.* Review of Scientific Instruments, 1972. **43**(7): p. 999.

85. Binnig, G., et al., *Surface Studies by Scanning Tunneling Microscopy.* Physical Review Letters, 1982. **49**(1): p. 57.

86. Binnig, G. and H. Rohrer, *Scanning tunneling microscopy—from birth to adolescence.* Reviews of Modern Physics, 1987. **59**(3): p. 615.

87. Song, Y.J., et al., *Invited Review Article: A 10 mK scanning probe microscopy facility.* Review of Scientific Instruments, 2010. **81**(12): p. 121101.

88. Griffiths, D.J., *Introduction to Quantum Mecanics*. 2nd ed. 2004: Benjamin Cummings.

89. Stroscio, J.A. and W.J. Kaiser, eds. *Scanning Tunneling Microscopy*. 1993, Academic Press, Inc: San Diego, CA.

90. Grandidier, B., et al., *STM measurements of barrier height on Si(111)-7×7 and GaAs(110) cleaved surfaces using I(z), z(V) and I(z(V),V) techniques.* Applied Physics A: Materials Science & Processing, 1998. **66**(0): p. S977.

91. Lang, N.D., *Spectroscopy of single atoms in the scanning tunneling microscope.* Physical Review B, 1986. **34**(8): p. 5947.

92. Mogenstern, M., *Probing the Local Density of States of Dilute Electron Systems in Different Dimensions.* Surface Review & Letters, 2003. **10**(6): p. 933.

93. Harrell, L., *Investigation of Gold Nanocrystals by Ultrahigh Vacuum Cryogenic Scanning Tunneling Microscopy*, in *Physics*. 1998, Georgia Institute of Technology: Atlanta, GA.

94. Harrell, L.E. and P.N. First, *An ultrahigh vacuum cryogenic scanning tunneling microscope with tip and sample exchange.* Review of Scientific Instruments, 1999. **70**(1): p. 125.

95. Melmed, A.J. *The art and science and other aspects of making sharp tips*. 1991. Boston, Massachusetts (USA): AVS.

96. Dardona, S., *Energy Relaxation and Hot-electron Lifetimes in Single Nanocrystals*, in *Physics*. 2006: Atlanta, GA.

97. Pan, S.H., E.W. Hudson, and J.C. Davis, *^{3}He refrigerator based very low temperature scanning tunneling microscope.* Review of Scientific Instruments, 1999. **70**(2): p. 1459.

98. Rutter, G.M., *Atomic Scale Properties of Epitaxial Graphene Grown on SiC (0001)*, in *Physics*. 2008: Atlanta, GA.

99. Min, H., et al., *Landau Levels and Band Bending in Few-Layer Epitaxial Graphene.* 2011.

100. Li, G., A. Luican, and E.Y. Andrei, *Scanning Tunneling Spectroscopy of Graphene on Graphite.* Phys. Rev. Lett., 2009. **102**(17): p. 176804.

101. Luican, A., G. Li, and E.Y. Andrei, *Scanning tunneling microscopy and spectroscopy of graphene layers on graphite.* Solid State Communications, 2009. **149**(27-28): p. 1151.

102. Pereira, J.M., F.M. Peeters, and P. Vasilopoulos, *Landau levels and oscillator strength in a biased bilayer of graphene.* Physical Review B, 2007. **76**(11): p. 115419.

103. Flores, F., et al., *Voltage drop in the experiments of scanning tunneling microscopy for Si.* Physical Review B, 1984. **30**(4): p. 2289.

104. Feenstra, R.M. and J.A. Stroscio, *Tunneling spectroscopy of the GaAs(110) surface.* Journal of Vacuum Science & Technology B: Microelectronics and Nanometer Structures, 1987. **5**(4): p. 923.

105. Feenstra, R.M., *Electrostatic potential for a hyperbolic probe tip near a semiconductor.* Journal of Vacuum Science & Technology B: Microelectronics and Nanometer Structures, 2003. **21**(5): p. 2080.

106. Lucier, A.-S., *Preparation and Characterization of Tungsten Tips Suitable for Molecular Electronics Studies*, in *Physics*. 2004, McGill University: Montreal, Quebec.

107. Tiedje, T., et al., *Tip contamination effects in ambient pressure scanning tunneling microscopy imaging of graphite.* Journal of Vacuum Science & Technology A: Vacuum, Surfaces, and Films, 1988. **6**(2): p. 372.

108. Morgenstern, M., et al., *Landau Level Quantization Measured by Scanning Tunneling Spectroscopy on n-InAs(110).* physica status solidi (b), 1998. **210**(2): p. 845.

109. Dombrowski, R., et al., *Tip-induced band bending by scanning tunneling spectroscopy of the states of the tip-induced quantum dot on InAs(110).* Phys. Rev. B, 1999. **59**(12): p. 8043.

110. Stoll, E.P., *Why do 'dirty' tips produce higher-resolution images when graphite is scanned in a scanning tunnelling microscope?* Journal of Physics C: Solid State Physics, 1988. **21**(26): p. L921.

111. Matsui, T., et al., *STS Observations of Landau Levels at Graphite Surfaces.* Physical Review Letters, 2005. **94**(22): p. 226403.

112. Hashimoto, K., et al., *Quantum Hall Transition in Real Space: From Localized to Extended States.* Physical Review Letters, 2008. **101**(25): p. 256802.

113. Marczinowski, F., et al., *Effect of charge manipulation on scanning tunneling spectra of single Mn acceptors in InAs.* Physical Review B (Condensed Matter and Materials Physics), 2008. **77**(11): p. 115318.

114. Xia, J., et al., *Measurement of the quantum capacitance of graphene.* Nat Nano, 2009. **4**(8): p. 505.

115. Jung, S., et al., *Evolution of microscopic localization in graphene in a magnetic field from scattering resonances to quantum dots.* Nat Phys, 2011. **7**(3): p. 245.

116. Song, Y.J., et al., *High-resolution tunnelling spectroscopy of a graphene quartet.* Nature, 2010. **467**(7312): p. 185.

117. Fogler, M.M., D.S. Novikov, and B.I. Shklovskii, *Screening of a hypercritical charge in graphene.* Phys. Rev. B, 2007. **76**(23): p. 233402.

118. *Interactive Data Language*. 2011; Available from: http://www.ittvis.com/language/en-us/productsservices/idl.aspx.

119. Markwardt, C.B., *Non-linear Least-squares Fitting in IDL with MPFIT.* Astronomical Data Analysis Software and Systems XVIII, 2009. **411**: p. 251.

120. Moré, J., *The Levenberg-Marquardt algorithm: Implementation and theory*, in *Numerical Analysis*, G. Watson, Editor. 1978, Springer Berlin / Heidelberg. p. 105.

121. *Origin 8.5 Data Analysis and Graphing Software*. Available from: http://www.originlab.com/.

122. Foster, A., *Theoretical Modelling of Non-contact Atomic Force Microscopy on Insulators*, in *Condensed Matter and Materials Physics Group*, University College London

123. Hansen, W.N. and G.J. Hansen, *Standard reference surfaces for work function measurements in air.* Surface Science, 2001. **481**(1-3): p. 172.

124. Wilson, R.G., *Vacuum Thermionic Work Functions of Polycrystalline Nb, Mo, Ta, W, Re, Os, and Ir.* Journal of Applied Physics, 1966. **37**(8): p. 3170.

125. Kanibolotskii, V.G., F.D. Miroshnichenko, and V.L. Snezhnoi, *Magnetostriction of stainless steels in relation to heat treatment* Metal Science and Heat Treatment, 1972. **14**(5): p. 445.

126. Wu, X., et al., *Weak Antilocalization in Epitaxial Graphene: Evidence for Chiral Electrons.* Physical Review Letters, 2007. **98**(13): p. 136801.

127. Miller, D.L., et al., *Structural analysis of multilayer graphene via atomic moiré interferometry.* Physical Review B, 2010. **81**(12): p. 125427.

128. N. Ashcroft, N.M., ed. *Solid State Physics*. 1976, Brooks Cole: London.

129. Gusynin, V.P. and S.G. Sharapov, *Magnetic oscillations in planar systems with the Dirac-like spectrum of quasiparticle excitations. II. Transport properties.* Physical Review B, 2005. **71**(12): p. 125124.

130. Sharapov, S.G., V.P. Gusynin, and H. Beck, *Magnetic oscillations in planar systems with the Dirac-like spectrum of quasiparticle excitations.* Physical Review B, 2004. **69**(7): p. 075104.

131. Rollings, E., et al., *Synthesis and characterization of atomically thin graphite films on a silicon carbide substrate.* Journal of Physics and Chemistry of Solids. **67**(9-10): p. 2172.

132. Bostwick, A., et al., *Quasiparticle dynamics in graphene.* Nat Phys, 2007. **3**(1): p. 36.

133. Recher, P., et al., *Aharonov-Bohm effect and broken valley degeneracy in graphene rings.* Physical Review B, 2007. **76**(23): p. 235404.

134. Russo, S., et al., *Observation of Aharonov-Bohm conductance oscillations in a graphene ring.* Physical Review B, 2008. **77**(8): p. 085413.

135. Aharonov, Y. and D. Bohm, *Significance of Electromagnetic Potentials in the Quantum Theory.* Physical Review, 1959. **115**(3): p. 485.

136. Wurm, J. and et al., *Graphene rings in magnetic fields: Aharonov–Bohm effect and valley splitting.* Semiconductor Science and Technology, 2010. **25**(3): p. 034003.

137. Wittneven, C., et al., *Scattering States of Ionized Dopants Probed by Low Temperature Scanning Tunneling Spectroscopy.* Phys. Rev. Lett., 1998. **81**(25): p. 5616.

138. Chen, J.-H., et al., *Charged-impurity scattering in graphene.* Nat Phys, 2008. **4**(5): p. 377.

139. Novikov, D.S., *Elastic scattering theory and transport in graphene.* Physical Review B, 2007. **76**(24): p. 245435.

140. Huard, B., et al., *Evidence of the role of contacts on the observed electron-hole asymmetry in graphene.* Physical Review B, 2008. **78**(12): p. 121402.

141. Shytov, A., et al., *Atomic collapse, Lorentz boosts, Klein scattering, and other quantum-relativistic phenomena in graphene.* Solid State Communications, 2009. **149**(27-28): p. 1087.

142. Wehling, T.O., M.I. Katsnelson, and A.I. Lichtenstein, *Impurities on graphene: Midgap states and migration barriers.* Phys. Rev. B, 2009. **80**(8): p. 085428.

143. Teichmann, K., et al., *Controlled Charge Switching on a Single Donor with a Scanning Tunneling Microscope.* Physical Review Letters, 2008. **101**(7): p. 076103.

144. Pradhan, N.A., et al., *Atomic Scale Conductance Induced by Single Impurity Charging.* Phys. Rev. Lett., 2005. **94**(7): p. 076801.

145. Ando, T., *Electron Localization in a Two-Dimensional System in Strong Magnetic Fields. II. Long-Range Scatterers and Response Functions.* Journal of the Physical Society of Japan. **53**(Copyright (C) 1984 The Physical Society of Japan): p. 3101.

146. Depuydt, A., et al., *Scanning tunneling microscopy and spectroscopy at low temperatures of the (110) surface of Te-doped GaAs single crystals.* Phys. Rev. B, 1999. **60**(4): p. 2619.

147. Tikhonenko, F.V., et al., *Weak Localization in Graphene Flakes.* Physical Review Letters, 2008. **100**(5): p. 056802.

148. Tikhonenko, F.V., et al., *Transition between Electron Localization and Antilocalization in Graphene.* Physical Review Letters, 2009. **103**(22): p. 226801.

149. Liao, Z.-M., et al., *Gate voltage dependence of weak localization in bilayer graphene.* Applied Physics Letters, 2010. **97**(16): p. 163110.

150. Magdalena, H. and et al., *The Aharonov–Bohm effect in a side-gated graphene ring.* New Journal of Physics, 2010. **12**(4): p. 043054.

VITA

Kevin D. Kubista

Kevin D. Kubista was born in Minnesota, where he was raised with his siblings Kristi and Laura in a rural town called Delano. During his childhood he participated in many extracurricular activities including boy scouts, science olympiad, athletic competitions, drama club, jazz band and choir, and math team. He continued to enjoy his love of music while at St. Olaf College by participating in the St. Olaf Viking Chorus and St. Olaf Chapel Choir. While at St. Olaf Kevin was elected the presented of SPS, where he helped start to revitalize the local chapter by introducing a trebuchet competition. He graduated magna cum laude from St. Olaf College in 2005 with his B. A. in Physics and Mathematics. He then began his Ph.D. work at Georgia Tech. During his graduate work Kevin spent his free time traveling or participating in the Atlanta Area Aquarium Association as a B.O.D. member. With his fellow fish club members he helped organize and run the American Cichlid Association Convention in Atlanta. Upon Graduating from Georgia Tech Kevin will begin his job at Intel in Portland, Oregon.